

Dissertation

# Aeroacoustics of dual-channel mass flow measurement devices

performed for the purpose of obtaining the academic degree  
of Doctor of Technical Science under the supervision of

**Univ.Prof. Dipl.-Ing. Dr.techn. Manfred Kaltenbacher**  
Institute of Mechanics and Mechatronics  
Measurement and Actuator Division

submitted to the Vienna University of Technology  
**Faculty of Mechanical and Industrial Engineering**

by

**Dipl.-Ing. Natalie Helena Schlachter**



Vienna, November 2016

*Natalie*

---



## Abstract

Measuring high speed fluid flows in ducts with dual-channel mass flow meters results in a large scattering of the measurement values outside the 0.35% error specification. However the origin of these errors remained, unlike other influences such as temperature and pressure, unresolved. This work was initiated with the motivation to prove that the cause of the measurement value scattering lies in flow-induced sound. An analysis of the flow-induced sound on such a device is complex. The main acoustic source is located within the meter itself, where the large hydrodynamic pressures superimpose the much smaller acoustic pressures and make any direct measurement of the acoustic quantities impossible. For this purpose a vibroacoustic examination of the system has been completed using a hybrid computational aeroacoustic method, applying Lighthills acoustic analogy and splitting the fluctuating pressures into their incompressible and acoustic components. The location of the main acoustic source, and the disturbance frequencies due to the flow-induced sound could be identified in the numerical analysis and verified with measurements of the duct displacements on three different devices using two Doppler laser vibrometers on a calibration rig. Furthermore, a distinct behaviour of the acoustic pressures and duct displacements over Reynolds number could be identified, which is dependent on the turbulence energy spectrum at the location of the main source. The scattering of the measurement values does not result directly from the produced acoustic pressures, but in their amplification through acoustic resonances in the system. Through design, this resonance behaviour could be suppressed and the stability and repeatability accuracy of the dual-channel mass flow devices improved by a factor of five. The measurement performance of the novel designs was verified on a calibration rig, and was found to comply with maximum error specifications of 0.25%. In future, these acoustic considerations will be made part of the optimization algorithms applied in dual channel mass flow meter design to ensure accurate measurements of high speed fluid flows.



Dissertation

# Strömungsakustik in Doppelrohr Massendurchflussmesser

ausgeführt zum Zwecke der Erlangung des akademischen Grades  
eines Doktors der technischen Wissenschaften unter der Leitung von

**Univ.Prof. Dipl.-Ing. Dr.techn. Manfred Kaltenbacher**

Institut für Mechanik und Mechatronik

Abteilung für Messtechnik und Aktorik

eingereicht an der Technischen Universität Wien

**Fakultät für Maschinenwesen und Betriebswissenschaften**

von

**Dipl.-Ing. Natalie Helena Schlachter**



Wien, November 2016



## Kurzfassung

Die Messung von großen Strömungsgeschwindigkeiten mit Doppelrohr Massendurchflussgeräten führt zu einer großen Streuung der Messergebnisse. Jedoch blieb die Quelle dieser Fehler, anders als die Einflüsse von Temperatur oder Druck, noch ungelöst. Diese Arbeit hatte zum Ziel, diese Fehler mit strömungsinduziertem Schall zu erklären. Die Analyse von strömungsinduziertem Schall in diesem Messsystem ist komplex, da die akustischen Quellen innerhalb des Gerätes selber entstehen, wo große hydrodynamische Drücke die kleinen akustischen Drücke überlagern und eine direkte Messung des Schalls unmöglich machen. Aus diesem Grund wurde eine vibroakustische Untersuchung des Geräts durchgeführt und unter Verwendung der akustischen Lighthill Analogie und Trennung der schwankenden Drücke in ihre inkompressiblen und akustischen Komponenten ergänzt. Sowohl die dominante akustische Quelle, als auch die störenden Frequenzen wurden in der numerischen Analyse identifiziert und durch Messungen der Auslenkung der Messrohre an drei unterschiedlichen Geräten mit zwei Doppler Laser Vibrometern an einer Kalibrieranlage verifiziert. Weiterhin wurde ein deutliches Verhalten der akustischen Drücke und Rohrverschiebungen über die Reynoldszahl erkannt, welche in Verbindung zum Energiespektrum der Turbulenzen steht. Die Streuung der Messergebnisse entsteht nicht direkt aufgrund der akustischen Drücke, jedoch durch deren Verstärkung aufgrund akustischer Resonanzen im System. Durch ein geändertes Design konnte diese Verstärkung unterdrückt werden und die Stabilität und Wiederholbarkeit des Massendurchflussgeräts um einen Faktor von fünf verbessert werden. Die Messleistung des neuartigen Designs wurde auf einer Kalibrieranlage verifiziert und liegt innerhalb einer maximalen Fehlerangabe von 0.25%. In Zukunft werden die erarbeiteten akustischen Überlegungen im Optimierungsalgorithmus aller Doppelrohr Massendurchflussgeräte integriert werden, um hoch genaue Messungen von Medien mit hohen Geschwindigkeiten sicher zustellen.






## Ehrenwörtliche Erklärung

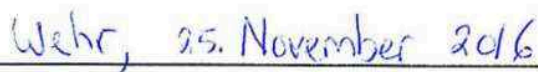
Ich erkläre ehrenwörtlich, dass ich die vorliegende wissenschaftliche Arbeit selbstständig angefertigt und die mit ihr unmittelbar verbundenen Tätigkeiten selbst erbracht habe. Ich erkläre weiters, dass ich keine anderen als die angegebenen Hilfsmittel benutzt habe. Alle aus gedruckten, ungedruckten oder dem Internet im Wortlaut oder im wesentlichen Inhalt übernommenen Formulierungen und Konzepte sind gemäß den Regeln für wissenschaftliche Arbeiten zitiert und durch Fußnoten bzw. durch andere genaue Quellenangaben gekennzeichnet.

Die während des Arbeitsvorganges gewährte Unterstützung einschließlich signifikanter Betreuungshinweise ist vollständig angegeben. Die wissenschaftliche Arbeit ist noch keiner anderen Prüfungsbehörde vorgelegt worden. Diese Arbeit wurde in gedruckter und elektronischer Form abgegeben. Ich bestätige, dass der Inhalt der digitalen Version vollständig mit dem der gedruckten Version übereinstimmt.

Ich bin mir bewusst, dass eine falsche Erklärung rechtliche Folgen haben wird.



\_\_\_\_\_  
(Unterschrift)



\_\_\_\_\_  
(Ort, Datum)

## Acknowledgments

I have always dreamed about completing a doctorate, but I could never have imagined how many people would help me fulfill this dream.

It starts, and ends, with my tireless supervisor Prof. Dr. Manfred Kaltenbacher. Only through your constant guidance and endless knowledge could I complete a work I am really proud of. Thank you also, for always stressing the importance of the fundamental principles. Furthermore, I would like to thank my two external assessors, Prof. Dr. Christian Bauer and Prof. Dr. Stefan Becker, for taking the time to review my work.

It continues with Endress+Hauser Flowtec AG, a company which supports the further education of its employees fully and made the prospect of an industrial promotion achievable. I would like to thank my department leaders at Endress+Hauser, Wolfgang Brobeil, Oliver Popp and Martin Anklin, who worked with me to make my dissertation possible. Martin thank you especially for supporting me, and above all, for giving me the time in which to complete this degree.

A big thank you to all my colleagues, both at the Vienna University of Technology and Endress+Hauser, for always lending a helping hand when it was needed. Especially Andreas Hüppe for his help with complicated software problems, as well as the team who has helped me with the building of my prototypes and the calibration measurements.

Thank you to my family and friends, who always had encouraging words when they were needed. And to my husband, Marc, who has supported me from the very beginning, and dealt with many stressful times and long absences. You were always my biggest motivator thank you.

This work was completed with the use of a student license of Star CCM+ provided by CD Adapco, and with granted access to the Vienna Scientific Cluster.

---

# Contents

---

<b>1</b>	<b>Introduction</b>	<b>1</b>
1.1	State of the art . . . . .	2
1.1.1	Acoustics in industrial pipelines . . . . .	2
1.1.2	Dual-channel mass flow meters . . . . .	4
1.2	Theoretical background . . . . .	9
1.2.1	Sound propagation in circular ducts . . . . .	9
1.2.2	Computational aeroacoustics . . . . .	14
1.3	Motivation . . . . .	17
1.4	Hypothesis . . . . .	18
1.5	Outline of work . . . . .	19
<b>2</b>	<b>Computational Aero- and Vibroacoustics</b>	<b>20</b>
2.1	Equations of fluid mechanics and the general wave equation	21
2.2	Aeroacoustic Equations . . . . .	24
2.3	Mechanic Acoustic Coupling . . . . .	27
<b>3</b>	<b>Numerical Models and Simulation</b>	<b>29</b>

3.1	Geometrical Models . . . . .	29
3.2	Fluid Dynamic Simulation . . . . .	32
3.3	Acoustic Mechanical Simulation . . . . .	35
<b>4</b>	<b>Simulation Results</b>	<b>41</b>
4.1	Fluid Dynamic Simulation Results . . . . .	41
4.2	Vibroacoustic Simulation Results . . . . .	45
4.2.1	Comparison of numerical approaches . . . . .	45
4.2.2	Final vibroacoustic results . . . . .	47
<b>5</b>	<b>Verification of Simulation Results</b>	<b>62</b>
5.1	Numerical Verifications . . . . .	62
5.2	Measurements . . . . .	66
<b>6</b>	<b>Interpretation of device performance</b>	<b>77</b>
6.1	Clarification of measurement error . . . . .	77
6.2	Statistical values of turbulence . . . . .	84
6.3	Device performance factors . . . . .	89
<b>7</b>	<b>Improved design</b>	<b>93</b>
7.1	Methods for design improvement . . . . .	93
7.1.1	Targeted design of the acoustic resonances and drive frequency . . . . .	94
7.1.2	Increase the driven vibration amplitude . . . . .	95
7.1.3	Improved filter in device electronics . . . . .	96
7.1.4	Decreasing the acoustic source amplitude . . . . .	96
7.1.5	Reducing the effect of the acoustic source on the sensors . . . . .	100
7.2	Acoustic impedance, resonators and horn theory . . . . .	103
7.3	Prototype design and verification . . . . .	109
7.4	1D Acoustics and a design tool for dual channel meters . . . . .	115
<b>8</b>	<b>Conclusion</b>	<b>122</b>
8.1	Summary . . . . .	122
8.2	Outlook . . . . .	124

---

## Notation and Abbreviations

---

In this thesis, scalars are represented by normal letters ( $b$ ), Cartesian vectors are set in bold italic letters ( $\mathbf{b}$ ) and tensors by bold letters. Matrices are capital boldface Roman letters ( $\mathbf{B}$ ).

### Abbreviations

ABC	Acoustic boundary condition
CAD	Computer aided design
CFD	Computational fluid dynamics
CFS	Coupled field simulation
DNS	Direct numerical simulation
FE	Finite element
FEM	Finite element method
PDE	Partial differential equation
PML	Perfectly matched layer
SPL	Sound pressure level

### Fluid mechanics

$\gamma$	Specific heat ratio
$\eta$	Dynamic viscosity
$\nu$	Kinematic viscosity
$h$	Mesh element size
$e$	Internal energy
$E$	Turbulent energy
$M$	Mach number
$p$	Fluid pressure
$\mathbf{T}$	Viscous stress tensor
$\rho_f$	Fluid density
$\mathbf{R}_{ii}$	Correlation tensor
$t$	Time
$\mathbf{u}$	Fluid velocity

### Structural mechanics

$\alpha$	Test function
$\delta$	Decrement
$\omega$	Rotational velocity
$\nu$	Poisson's ratio
$\phi$	Phase shift
$\rho_s$	Structural density
$\theta$	Test function
$\xi$	Damping
$\Gamma_s$	Structural boundary
$\Omega_s$	Structural domain
$a$	Duct radius
$A$	Amplitude
$A_x$	Area x
$[\mathbf{c}_s]$	Tensor of elasticity

$C$	Calibration factor
$E$	Elasticity modulus
$f_v$	External force
$F_c$	Coriolis force
$\mathbf{I}$	Identity matrix
$k$	Thermal conductivity
$K$	Mechanical stiffness
$L$	Length
$M$	Mechanical mass
$Q$	Quality factor
$S$	Area ratio
$T$	Period
$\mathbf{u}$	Mechanical displacement; also used for fluid velocity
$W$	Mechanical energy

### Aeroacoustics

$\square'$	Perturbation quantity
$\bar{\square}$	Mean quantity
$\square_a$	Acoustic quantity
$\square_{ic}$	Incompressible field variable
$\square_0$	Constant material parameters
$\square_m$	Mechanical quantity
$\lambda$	Wavelength
$\pi$	Momentum flux
$\rho$	Density
$\tau$	Viscous stress tensor
$\sigma$	Damping
$\varphi_a$	Scalar acoustic velocity potential
$\Omega_a$	Acoustic domain
$c$	Speed of sound

$c_v, c_p$	Specific heat at constant volume/ pressure
$f$	Frequency
$f_c$	Cut off frequency
$F$	Acoustic source
$j'_{mn}$	Zero of the Bessel function
$k$	Wavenumber
$K$	Transfer matrix
$I_a$	Acoustic velocity flux
$M$	Mach number
$p_a$	Acoustic pressure
$p_h$	Hydrodynamic fluid pressure
$q_a$	Sound volume flux
$\mathbf{T}_{LH}$	Lighthill stress tensor
$TL$	Transmission loss
$\mathbf{u}_a$	Acoustic particle velocity
$Z_a$	Acoustic impedance

### Mathematical Operators

$\nabla b$	Gradient of scalar valued function $b$
$\nabla \cdot \mathbf{b}$	Divergence of vector valued function $\mathbf{b}$
$\nabla \times \mathbf{b}$	Curl of vector function $\mathbf{b}$
$\Delta b$	Laplacian of scalar valued function $b$ ( $\Delta b = \nabla \cdot \nabla b$ )
$\mathcal{F}$	Fourier transform
$\int_{\Gamma} d\Gamma$	Surface integral
$\int_{\Omega} d\Omega$	Volume integral
$B$	Differential operator
$\frac{\partial}{\partial x}$	Spatial partial derivative
$\frac{\partial}{\partial t}$	First partial derivative with respect to time
$\frac{\partial^2}{\partial t^2}$	Second partial derivative with respect to time
$\frac{D}{Dt}$	Substantial derivative



# CHAPTER 1

---

## Introduction

---

This work handles an array of topics including duct acoustics, aeroacoustics and vibroacoustics with focus on obtaining accurate flow measurements with dual channel systems in industrial applications. The introductory chapter initiates these topics through a description of the latest published research in these fields, and a discussion on the current measurement principle and performance of dual-channel mass flow measurement devices. A short theoretical background is provided, which is extended upon in later chapters, followed by the motivation for the current work. Conclusively a hypothesis for the study is drawn and the structure of the subsequent chapters is outlined.

## 1.1 State of the art

### 1.1.1 Acoustics in industrial pipelines

In a turbulent fluid flow, both hydrodynamic and acoustic pressure fluctuations are present. The acoustic perturbations are what we term sound, as they are characterized by their ability to propagate [1]. Since these acoustic pressures are induced by a flowing fluid, their study is termed aeroacoustics. Although the hydrodynamic pressure is of larger amplitude, it is the acoustic pressure which can travel through the mechanical system and have a large impact on account of resonance frequency matching [2]. The study of the mechanical response of a structure due to these acoustic pressures is termed vibroacoustics. In some instances the sound production and mechanical vibrations in a certain system are small enough to be ignored, or do not cause any damage. In other cases it is the environmental noise that decreases personal comfort such as in heating, ventilation and air conditioning (HVAC) installations [3]. In more serious cases the mechanical integrity or the performance of system components is affected. The fundamental theory of duct acoustics becomes relevant since these disturbances often arise in systems for the transport of fluids due to instabilities and turbulences in the flow, or due to sound propagation generated by obstructing components in the network.

The importance of correct aeroacoustic design which avoids the occurrence of objectionable phenomena is widely documented in scientific literature. Research topics range from general investigations on flow-induced vibrations of cylindrical structures exposed to a flow such as from Zhu [4] and Chen [5], to the implementations for industry [6], to examinations of concrete cases. The studies of Firth [7] arose because of the need to be able to predict the acoustic fields produced in the system of nuclear reactors, which are created by unsteady flow mechanisms associated with the fluid pumps. Lirvat [8] examined the flow in the main steam-line and safety relief valve branches of a boiling water reactor in order to understand the mechanisms for induced structural vibrations which could lead to high-cycle fatigue damage. Large butterfly valves can generate significant noise sources with ensuing sound propagating in both the upstream

and downstream directions. This additional noise generated by valves in large lines connected to acoustic test facilities can mask the noise of the test hardware [9]. Mufflers [10] and corrugated pipes [11] are also designed adhering to acoustic considerations.

Areas of research related to the present case include investigations in to duct junctions, diameter changes and bends similar to those found within a dual-channel mass flow meter. A large area of interest surrounds T-shape junctions. Studies involve the application of scattering matrices to an incoming wave, as well as the interaction between the acoustic and hydrodynamic fields, see e.g. [12, 13]. Interesting findings include that waves incident on T junctions at the downstream side are only attenuated, while waves incident at the other branches may be amplified or attenuated depending on the Strouhal number. Additionally, the acoustic amplification of a rectangular junction is more severe than that of a circular one [12]. Xin [14] researched the different flow fields in T- and Y-junctions, finally concluding that the flow field performance is only optimal in an arc shaped junction with the radius of curvature playing a key role. Flow structures in orifices are also a large focus of study. Alenius [15] investigated the acoustic properties of an orifice in a duct exposed to a strong bias flow. She found that the incoming sound waves at a Strouhal number of 0.43 trigger a strong axisymmetric oscillation in the circular duct orifice. Maximum amplification of sound will occur at certain Strouhal numbers, and when these coincide with strong reflections from system boundaries a high tonal noise can be created. Gloerfelt [16] observed the Coanda effect in the study of turbulent flow through a diaphragm in a duct. The flow becomes asymmetric in spite of symmetric test sections and inlet conditions. Above a critical Reynolds number, a pitchfork bifurcation results. The increase of velocity near one wall is accompanied with a decrease in pressure, and once a pressure difference is established across the duct, it will maintain the asymmetry of the flow.

The research referenced above has focused on the reaction of an incoming wave to obstructions in a duct. Less widely covered in research, is the sound produced by the turbulent structures in the flow itself. Thus, the sound does not originate from an interaction between the flow and a solid boundary, but from the turbulent eddies in the fluid. An example

of research conducted in this regard involves HVAC systems, which have been numerically investigated by Hüppe [3]. These heating, ventilation and air conditioning systems consist of complex duct networks, with many changes in direction and to the duct diameter and shape. Additionally, the air can move at vast speeds through the mostly narrow ducts and the grade of turbulence is high. The flow induced noise is clearly audible and much effort has been applied in order to reduce the sound level. The main driver for this research is personal comfort, for example in a vehicle or at the workplace. Hüppe realized that the acoustics in such systems, where the aeroacoustic sound is generated very close to the observer, is difficult to measure accurately since in the near-field the acoustic field is superimposed by hydrodynamic quantities. He states that computational aeroacoustic approaches based on a perturbation ansatz allow a better separation of flow effects and audible acoustic components inside the source region. In order to understand the pure acoustic effects in the system, it is also this approach that will be used for the investigations in the present work.

### 1.1.2 Dual-channel mass flow meters

The current application extends the study of aero and vibroacoustic effects to mass flow measurement devices, where the accuracy of the measurement value may be negatively influenced by external vibrations caused by flow-induced sound. In most duct networks transporting a medium, the amount of fluid that travels through the pipeline needs to be controlled. One of the most accurate ways to achieve a mass flow measurement is using a dual-channel mass flow meter which is built directly in to the line. These meters are available for many applications, and are used in a variety of sectors such as the pharmaceutical, petrochemical, oil and gas and food industries for a large spectrum of pressures and temperatures. Available line diameter sizes range from 1 mm up to 350 mm, and they are constructed primarily using stainless steel or hastelloy materials. A typical device begins and ends with a standard flange for the process connection, between which it splits the fluid in to two smaller parallel ducts, used for the measurement of the flow. Attached to the two mea-

suring ducts is an electromagnetic exciter and two inductive sensors, see figure 1.1.

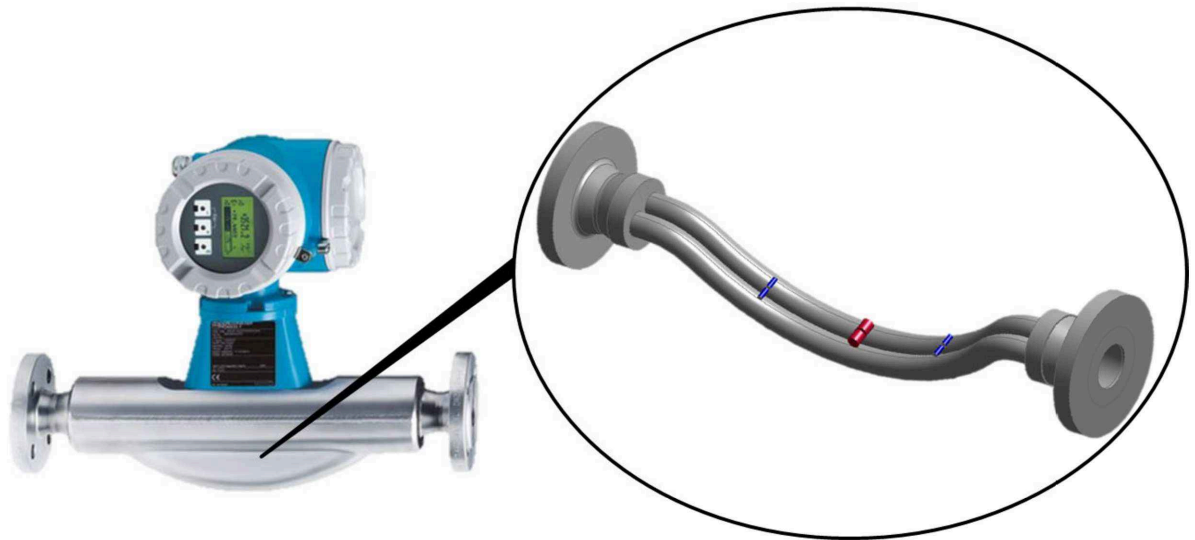


Figure 1.1: Endress + Hauser dual-channel mass flow meter showing the inner construction with two parallel measurement ducts, inductive sensors (blue) and driver (red)

The exciter at the center of the ducts causes them to vibrate at a certain resonant frequency, the so called drive mode, and the sensors pick up the corresponding displacement of the ducts at their two respective different positions, as marked in figure 1.1.

When the fluid is not flowing, the vibration of the measurement ducts corresponds exactly with the external excitation. This vibration can be seen as a rotation around the axis normal to the duct displacement and thus when the fluid starts flowing, the superimposed rotational and linear motions result in an inertial force acting on the fluid particles. This force, known as the Coriolis force, was defined by Gaspard Gustave de Coriolis in 1835 [17] using the mass  $m$ , flow velocity  $\mathbf{u}$  and duct rotation  $\boldsymbol{\omega}$  as

$$\mathbf{F}_c = 2m\mathbf{u} \times \boldsymbol{\omega}. \quad (1.1)$$

It is transferred to the duct surface via surface forces such as fluid

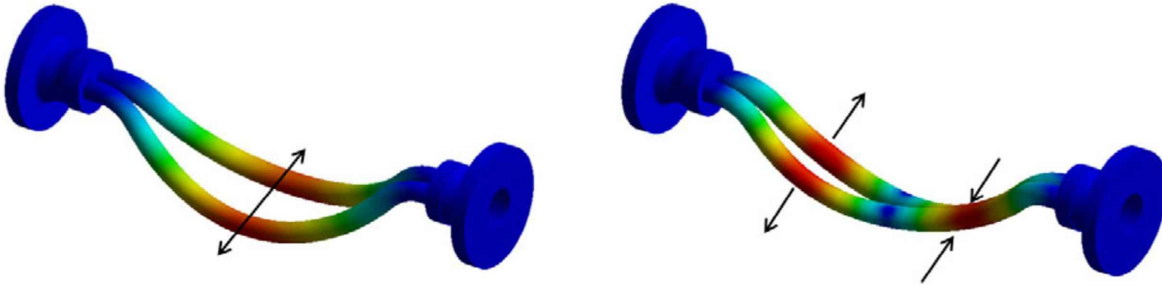


Figure 1.2: The drive mode (left) and Coriolis mode (right) of a dual channel mass flow meter

pressure or shear stress and results in a deformation of the duct walls. Since the rotation is in opposite directions near the inlet and outlet sides of the device, the Coriolis force acts in different directions, causing a deceleration of the fluid particles near the inlet and an acceleration near the outlet. Both operating modes are shown in figure 1.2. This influences the vibration of the measuring ducts and results in a phase shift  $\Delta\phi$  between the two output voltages of the inductive sensors. This measured phase shift is directly proportional to the mass flow [18]

$$\vec{m}_f \sim C \Delta t \quad C \frac{\Delta\phi}{f}, \quad (1.2)$$

where  $C$  is a calibration coefficient and  $f$  the drive frequency. The flow is split into two parallel measuring ducts to create a mechanical balance within the device. One duct is used for the flow measurement directly, while the second and identical duct works as a tilger to damp the produced vibration. In this way, vibration transfer to the process line can be minimized. Using a second identical tube filled with the same fluid as a tilger is very effective since the system is in balance independent of the fluid in the line. The effect of temperature and pressure variations in the process on the measurement reading are additionally compensated using algorithms in the device electronics.

The electronics of the device which receives the signals from the two sensors, applies a bandpass filter centered at the drive mode frequency

$f$  such that only signals with this frequency are used for the processing and calculation of the mass flow. The possible bandpass filter settings for the Coriolis device are 800 Hz, 400 Hz, 200 Hz, 100 Hz, 50 Hz, 25 Hz and 12 Hz, with the standard setting being 50 Hz, since the flow measurement value is output at this frequency. In this case the bandpass would be  $f \pm 50$  Hz, an example of which is shown on the left of figure 1.3.

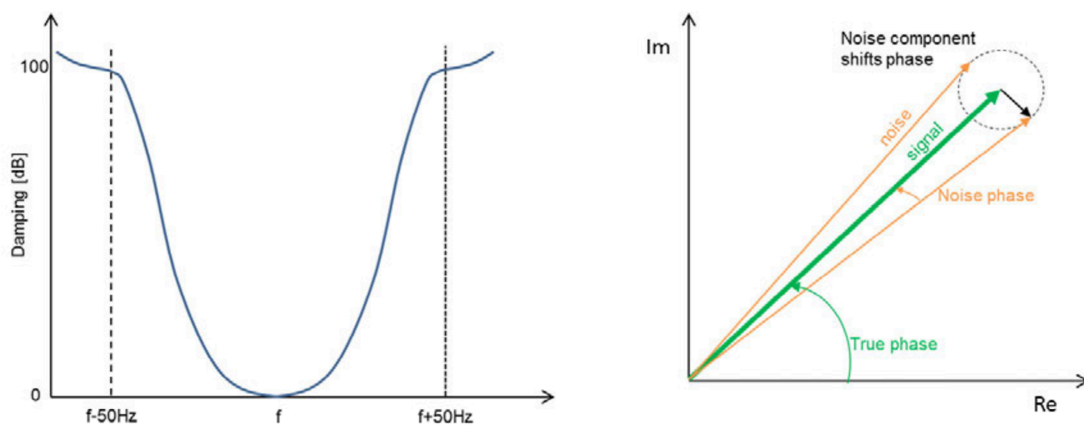


Figure 1.3: Filter stop band in the electronics for the standard setting (left) and the effect of noise on the phase signal (right).

If a disturbance frequency acts on the system, an additional signal is sent to the electronics. When the low-pass band filter is larger than the difference between the drive and disturbance frequencies, such that the disturbance is not filtered out, the unwanted perturbation will have an effect on the phase measurement. For the standard case, this means 50 Hz above and below the drive frequency. The effect is especially critical when the disturbance frequency is very close to the drive mode. The strength of the phase corruption depends on the amplitude ratio of the disturbance to the true measurement, as shown on the right of figure 1.3. The noise component shifts the true phase of the mass flow measurement signal, and a falsified mass flow calculation with an incorrect  $\Delta\phi$  in (1.2) results. The initial instinct would thus be to choose a very narrow bandpass filter [19]. However, when the filter is too small, the system response time increases and a mass-flow change takes longer to settle. This is

undesirable in applications with rapidly changing flow. Narrowing the bandpass would result in a slower signal processing speed, and thus less accurate measurements over time. The effect is shown on an example flow measurement in figure 1.4. When the bandpass width is decreased from 50 Hz to 12 Hz, the time for the change in mass flow increases from 0.15 s to 0.5 s. Additionally, alias frequencies which are multiples of the drive mode frequency, as well as at half of the drive mode frequency, can also be folded up or down and to some degree pass through the bandpass with relatively large amplitudes.

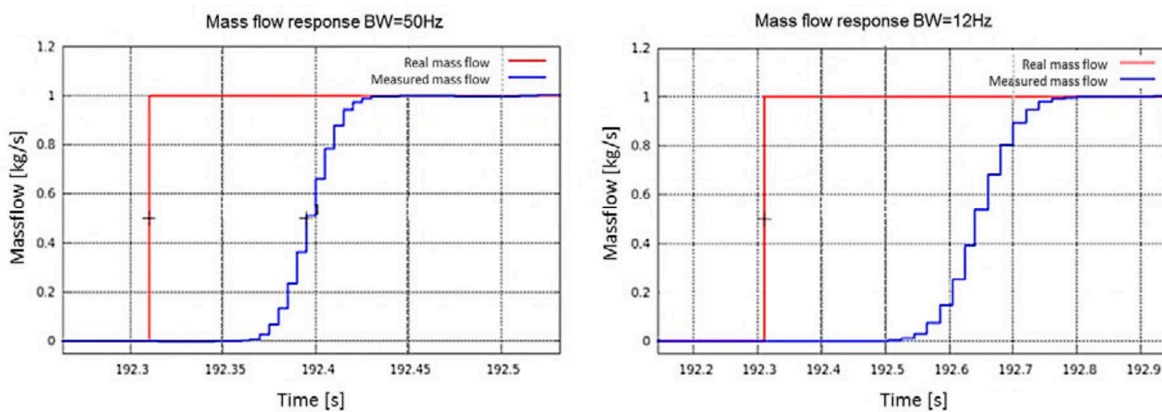


Figure 1.4: System response time for two different filter bandwidth settings.

The current design of dual channel mass meters centers around two main aspects: optimal mechanical performance and minimized pressure drop. Thus the construction of all components, such as the duct sizes and shape, and the flow splitter geometry, is designed such that the maximal response to the Coriolis force is obtained at the sensor position with minimal influence from external effects, and with minimal loss of pressure in the line. Current devices can measure liquid mass flows with an accuracy of up to 0.05% and gas flows, which prove more challenging, up to an accuracy of 0.35%. These accuracies are obtained for temperature ranges between  $-50^{\circ}\text{C}$  and  $350^{\circ}\text{C}$ , with pressures up to 250 bar in certain design versions. The measurement of gas flows is considerably more complicated due to the compressible nature of the medium. Nonetheless, repeatability



accuracies of up to 0.35% are specified. The latest developments to dual-channel flow meters can be seen from recent patents. Focus lies mostly on complex compensation algorithms for pressure, density and temperature effects, such as in [23] or [24], which are applied in the electronics, or on achieving further optimal mechanical balance through component design such as from Krohne [21], [20]. The optimization of the contours of the flow splitter geometry for minimized pressure loss is also a prominent topic [22], [25]. However, design optimizations considering the acoustics in dual-channel flow devices are novel, and becoming ever more important if constantly improving design accuracies want to be achieved. A dual channel mass meter can contain very turbulent flows when carrying fluids with high velocity. This turbulence is increased by the flow separation and joining before and after the two parallel measuring ducts respectively. The changes in duct diameters and the bends also contribute to increased flow turbulence. It is thus not surprising that flow-induced sound may arise in the system, and possibly at frequencies which are able to pass through the bandpass of the device electronics, causing a disturbance to the measurement reading.

## 1.2 Theoretical background

### 1.2.1 Sound propagation in circular ducts

The sound field in a duct may be solved using the wave equation by means of a series of expansion. The convective wave equation, as derived later in chapter 2,

$$\frac{1}{c_0^2} \frac{\partial^2 p_a}{\partial t^2} + M_x^2 \frac{\partial^2 p_a}{\partial x^2} + 2 \frac{M_x}{c_0} \frac{\partial^2 p_a}{\partial x \partial t} - \nabla^2 p_a = 0, \quad (1.3)$$

defines the acoustic pressure  $p_a$ , dependent on the time  $t$  and spatial coordinate  $x$ , in terms of the speed of sound  $c_0$  and the axial Mach number  $M_x$ . If a time harmonic pressure is assumed with a frequency  $\omega$  such that

$$p_a(t) = p_a(\omega)e^{-i\omega t}, \quad (1.4)$$

then the convective wave equation can be written as

$$[k^2 - M_x^2 \frac{\partial^2}{\partial x^2} + 2iM_x c_0 \frac{\partial}{\partial x} - \nabla^2] p_a = 0 \quad (1.5)$$

with  $k = \omega/c_0$ . Since the duct is cylindrical, we can define an ansatz using separation of variables with the radial coordinate  $r$ , angular coordinate  $\theta$  and axial coordinate  $x$ . This means that  $\nabla^2 = \frac{\partial^2}{\partial x^2} + \frac{\partial^2}{\partial r^2} + \frac{1}{r} \frac{\partial}{\partial r} + \frac{1}{r^2} \frac{\partial^2}{\partial \theta^2}$  and the result is an infinite sum of special solutions, called duct modes, that retain their shape when traveling down the duct [28]. The general description for sound propagation using polar coordinates in a circular duct is thus given by

$$p_a(x, r, \theta) = \sum_{m=-\infty}^{\infty} \sum_{n=-\infty}^{\infty} (A_{mn} e^{-ik_{mn}x} + B_{mn} e^{ik_{mn}x}) U_{mn}(r) e^{-im\theta}, \quad (1.6)$$

where  $A_{mn}$  and  $B_{mn}$  are the amplitudes of upstream and downstream duct mode  $mn$ ,  $m$  being the circumferential wave number and  $n$  the  $n^{\text{th}}$  zero of the Bessel function. The radial component  $U_{mn}(r)$  is a normalization factor based on the Bessel function and  $(r, \theta)$  is the cylindrical coordinate [26]. The axial wave number  $k_{mn}$  is given by one of the square roots

$$k_{mn} = \pm \sqrt{(\omega^2 - \alpha_{mn}^2)} \quad (1.7)$$

for radial eigenvalues  $\alpha_{mn}$  (+ for downstream and – for upstream propagation). The circumferential, radial and axial wave forms occurring in a cylindrical duct as described in (1.6) are visualized in figure 1.5. The shape of the wave is determined by the infinite combinations of  $(m, n)$  and the amplitude of this wave as it travels along the duct is defined by the axial form.

An important case is the plane wave with  $m = 0, n = 0$ , where the radial eigenvalue is zero and  $k_{00} = \omega$ . In the plane wave case, the first zero of the Bessel function is equal to zero. This fundamental mode can propagate at all frequencies, whereas all higher order modes have a

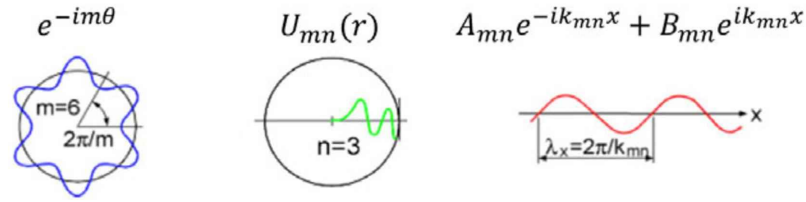


Figure 1.5: Visualization of the circumferential, radial and axial wave forms in a cylindrical duct

non-zero cut-off frequency below which they cannot propagate [27]. The reason for this behaviour is that the zeros of the Bessel function are an ever increasing sequence in both  $m$  and  $n$ , so there is always an  $m_0$  and  $n_0$  beyond which  $\alpha_{mn}^2 > \omega^2$  which results in a purely imaginary  $k_{mn}$ . In this case the duct modes decay exponentially in  $x$  and are called *cut-off* modes. The propagating modes are in turn called *cut on* modes. For low frequencies, where  $\omega$  is less than the first trivial zero of the Bessel function, all modes are *cut-off* and only the plane wave propagates. The critical frequency can be described with (1.8), and is seen to be dependent on the  $mn^{th}$  zero of the Bessel function  $j'_{mn}$ , the radius of the duct  $a$  and the speed of sound  $c_0$  [28]

$$f_c = \frac{j'_{mn} c_0}{2\pi a}. \quad (1.8)$$

When a mean flow is considered, the axial modal wave numbers are shifted to the left ( $M > 0$ ), or right ( $M < 0$ ) by a fixed amount of  $\omega M/(1 - M^2)$

$$k_{mn} = \frac{-\omega M \pm \sqrt{(\omega^2 - \alpha_{mn}^2)}}{1 - M^2}. \quad (1.9)$$

Accordingly the cut-off frequency is shifted to

$$\omega_{cM} = \omega_c \sqrt{1 - M^2}. \quad (1.10)$$

Thus with uniform mean flow the modal theory still applies, however with higher flow rates more modes are possibly cut-on than with lower flow

rates [28]. The acoustic field has a larger effect on duct wall vibration and external radiation in cases with severe disturbances, in comparison to those due to undisturbed turbulent pipe flow. The response of the duct wall to the internal acoustic field at low frequencies, at which no higher order modes propagate, is quite different from that at the higher frequencies where the higher order modes can also propagate. It is necessary to consider these two frequency ranges separately. At frequencies at which only plane acoustic waves can propagate in the duct, both forced pumping motions and resonant modes of the duct wall contribute to the acceleration response of the wall. Discontinuities in the pipe network result in changes to the acoustic impedance and may thus build acoustic resonances [28] between consecutive components. These acoustic resonances are described as

$$f_n = \frac{nc}{2L} \quad (1.11)$$

with the possibility of  $n$  acoustic resonances for a tube of length  $L$ , depending on the acoustic source. These acoustic resonances develop due to the propagating acoustic pressures in the system. For a circular duct with uniform wall thickness, theory predicts no coupling between plane waves and modes of circumferential order  $m > 0$ , but departures from the ideal state results in apparent excitation of all duct modes with resonance frequencies in this range [27]. Increases in the wall response and external radiation are largest at frequencies at which higher order acoustic modes can propagate, in which case wavenumber coincidence effects lead to a strong excitation of supersonic duct modes. This occurs when the wavenumbers of the structural and acoustic waves are equal at the duct wall. This type of coincidence usually occurs at a frequency close to the cut-off frequency of the acoustic mode involved. The phenomenon of complete coincidence is defined as the condition in which there is wavenumber coincidence and, in addition, equality of structural and acoustic frequencies. In general, because of the discrete nature of the structural resonance frequencies, only wavenumber coincidence will occur [27].

The behaviour may be different in bent pipes. The middle-radius bends produce small, if any, increases in wall acceleration and acoustic radia

tion over those due to undisturbed flow throughout the frequency range, while  $45^\circ$  and  $90^\circ$  mitred bends produce much more [27]. Studies from Sariguel [29] showed that sharper bends provide more sound attenuation corresponding to higher non dimensional wavenumbers in a wider range. For flow induced sound, there is additionally a dependency on the hydrodynamic field. Since the magnitude of the shed vorticity is amplified during its convected path over for example a T-junction, a net increase in sound power is possible, depending on the Strouhal number. For instance, if the time scale associated with vorticity convection across the junction opening equals an odd multiple of half the acoustic period, mostly attenuation will take place. For an even multiple amplification is expected. Thus, there will be several alternating Strouhal number regions of attenuation and amplification [12]. The near-field components are pressure fluctuations incurred by the adjacent fluid with boundary-layer turbulence being the most important near-field noise. The far-field components comprise all noises that propagate at the speed of sound. Sources of far-field noise include flow pulsations, vortex shedding over the submerged objects, turbulence generated by bends, cavitation, and the like. Boundary layer noise is always present if the flow is turbulent, however the strength of far-field noise depends on system design [5].

In a simple system the location of the duct modes and acoustic resonances are easily determined, in complex systems rather with the help of finite element methods to avoid simplification errors. However, determining which modes are able to occur and to what extent is more challenging, since the intensity and range of the acoustic sound source needs to be quantified, and this source depends on the mass flow. Additional transient multiphysics considerations also need to be implemented to compute the mechanical response to the acoustic pressures in the flow over a specified time period. These types of studies, as outlined above, have been conducted for varying pipeline geometries and components, resulting in optimized geometrical considerations. It has not as yet been conducted for dual-channel mass flow meters. The nature and extent of the acoustic influence on these measuring devices has remained, until now, unexplored. Due to the complex nature of the problem, and the coupling of three different physics models, the application of computational

aeroacoustics is best suited to obtain a usable solution.

### 1.2.2 Computational aeroacoustics

There are two main approaches to an aeroacoustical computation: a direct numerical simulation (DNS) and a hybrid simulation. The first methodology is based on the numerical solution of the compressible Navier Stokes equations which also includes acoustics. The big drawback of this method is the huge disparity of scales of the acoustic and flow fields. The resolution of the flow grid has to resolve small scale vortices, orders of magnitude smaller than the acoustic wave length propagating inside the region. In addition, the sound intensity is mostly very small in comparison to the energy quantities of the flow such that numerical noise pollutes the acoustic simulation. In certain applications this method does need to be applied, for example in applications where the sound-flow interaction is of increased importance such as in the studies of a diaphragm in a duct by Gloerfelt [16]. However in many cases the DNS solution is not feasible due to the enormous computational costs.

When the reaction of the fluid to the acoustics is assumed to be reasonably small, the hybrid method can be applied. In this method, based on an initial compressible or incompressible fluid dynamic simulation, the acoustic sources are computed by means of an appropriate aeroacoustic analogy as detailed in chapter 2. These sources are then used in a secondary step in which the acoustic wave propagation is simulated. This is a convenient separation of the two main areas of study: the estimation of the source characteristics (in terms of known aerodynamic quantities) and the modeling of the propagation of the generated sound [30]. The disparity of scales regarding the grid resolutions however remains, which is why the sources calculated in the initial computational fluid dynamic (CFD) step, have to be interpolated to a separate acoustic grid for the further acoustic analysis [3].

The approach used for the hybrid aeroacoustical simulation in this work is depicted in figure 1.6. Firstly the flow field is modeled using the fluid dynamic software StarCCM+ V9.02.007. This is a fully turbulent transient simulation with an appropriately fine discretization and time

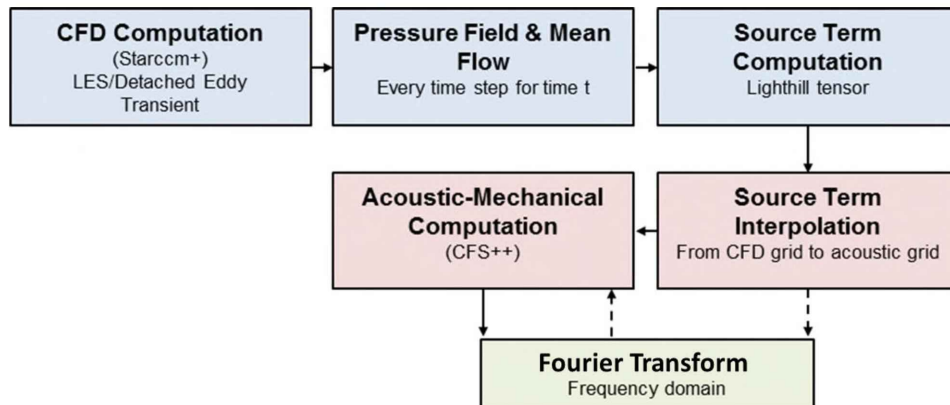


Figure 1.6: Flow chart of the implemented hybrid aeroacoustic simulation method.

step for the required frequency resolution as detailed in chapter 3. Once the transient simulation has reached a stable state, the incompressible pressure field over the whole fluid domain is exported at every time step. Additionally, the mean flow vector should be calculated for this time period. The total simulation time is dependent on the frequency domain required. The simulation values, for example the incompressible pressure and mean velocity field vector, are used to calculate the acoustic source terms as derived in chapter 2. The result is the acoustic source term value for each CFD element over time. The source term values can now be interpolated from the CFD grid to the acoustic grid. The interpolation on to a new grid is used to save computation time, since the acoustic computation allows for a much coarser grid.

The interpolation of the acoustic source term at every time step from the CFD grid to the acoustic grid is performed using the conservative interpolation technique described by Kaltenbacher [31]. The center value of the CFD volume element is positioned in the containing element of the acoustic grid and the associated value is distributed amongst the relevant 3 dimensional acoustic nodes. The algorithm extracts the acoustic cell center and interpolates the volume weighted source term according to the center coordinates, as pictured in figure 1.7. The algorithm is limited to acoustic elements which are larger than the CFD elements. This is usually

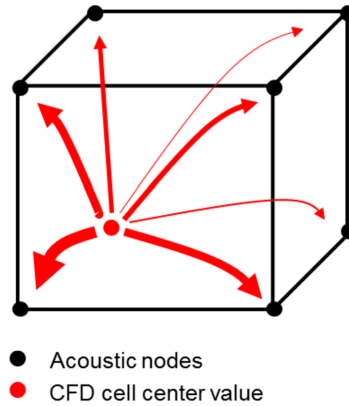


Figure 1.7: Visualization of the interpolation method for the transfer of the acoustic source terms from the CFD mesh to the acoustic mesh.

the case, since the acoustic model requires fewer elements for an accurate solution, and as a result many CFD cells are contained in one acoustic cell. In the broadest sense, the interpolation between meshes adheres to the energy conservation law, such that when a field  $q$  is interpolated from mesh  $A$  to mesh  $B$  in the domain  $\Omega$ , the following relation holds

$$\int_{\Omega} q_A dV = \int_{\Omega} q_B dV. \quad (1.12)$$

Now that the source terms are on an appropriate grid, the acoustic analysis may begin. The wave equation is solved for the acoustic pressure  $p^a$ , for example using the multiphysics software CFS++ [32]. These acoustic pressures may be examined in the time domain, or in the frequency domain if a Fourier transform is applied. Furthermore, since CFS++ has multiphysics capabilities, the acoustic simulation can be directly coupled to the mechanical solution of the duct, such that the vibrations on the mechanical system due to the acoustic pressures may be analyzed. The wave equation and the mechanic acoustic coupling equations are derived in chapter 2.



## 1.3 Motivation

When dual-channel mass flow meters are deployed to measure high velocity flows, frequently in gas applications, a reduced quality in the repeatability of the measurement outputs is observed. Different device constructions show different behaviours in this regard, as seen in figure 1.8, which shows the output scattering of ten measurements at each mass flow in three different devices.

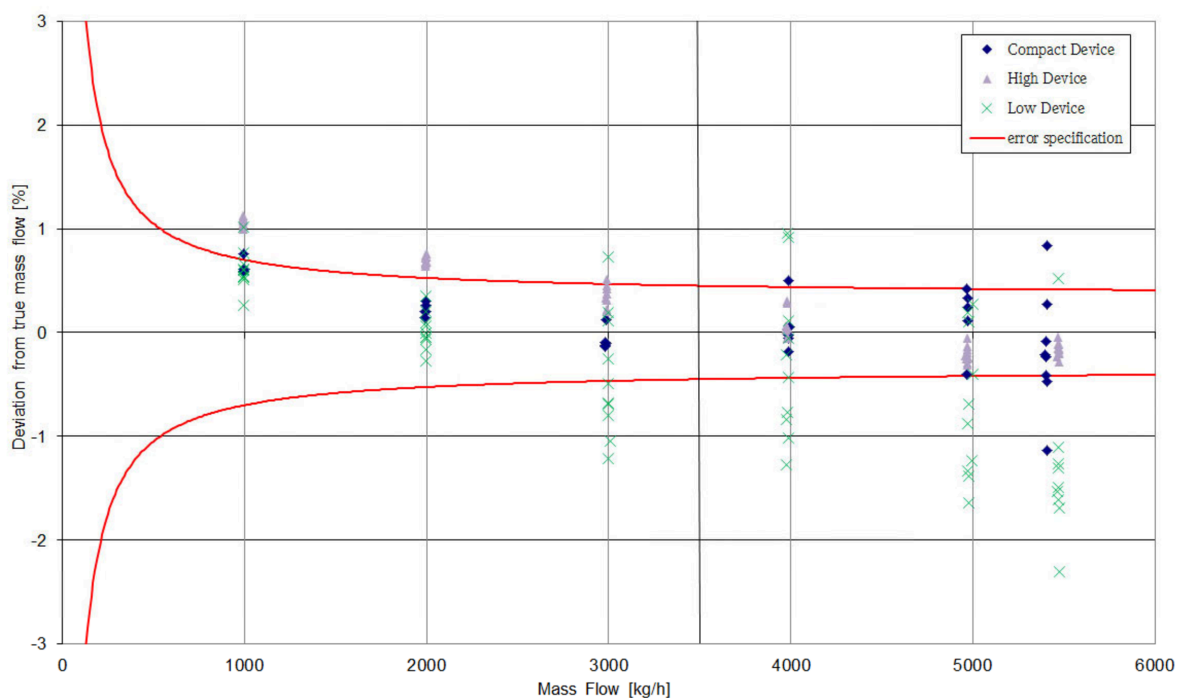


Figure 1.8: Scattering of measurement values for three different devices over mass flow rate with an error specification of 0.35%.

Some devices show a steady increase in the scattering of the measurement values with increasing mass flow, while other devices display maximal scattering at a certain flow rate, after which the performance improves again. The overall amplitude of scattering differs between mass flow devices, with different designs performing better or worse than others. The current performance of dual-channel mass flow meters with high speed gas applications thus poses a problem for the application of

the devices in the gas market with the required accuracy specifications. Prior investigations into the origin of these errors have been heretofore unsuccessful, and the lack of understanding of the underlying cause of the value scattering has hindered the discovery of a viable solution. The current work aims to identify the source of this phenomenon in dual channel devices at high flow rates, understand and quantify its influence on the measurement principle and if possible provide solutions for improved performance. For simplification of the problem, only devices with a nominal diameter of 50 mm will be considered, with the fluid medium air at 10 bar and room temperature.

### 1.4 Hypothesis

The cause for the impaired repeatability of the measurement results in dual-channel mass flow meters is suspected to be related to flow-induced sound. To confirm this assumption, the source of flow-induced sound in different dual-channel devices needs to be identified and quantified. Thereafter, the response of the system mechanics to this source needs to be examined in order to understand how and why the scattering of measurement values originates, as well as to understand the dependency of the scattering magnitudes on the Reynolds number. The aeroacoustic and vibroacoustic effects in dual-channel flow mass meters have hereto remained unexplored. Devices have been optimized according to ideal mechanical and flow considerations, but never concerning the in-duct acoustics. The geometry of the system is also unique, in that the flow is split into two smaller parallel pipes which contain an arch. The flow splitting and joining geometry is thus different to that found in, for example, T junctions. At the beginning of the work, it was uncertain if the aeroacoustic effects are present at all at the flow rates and mediums seen by such a device, and if so, to what degree their influence on the stiff device geometries results in a detrimental flow measurement value. The entire underlying mechanism is not yet defined, and only once this is understood, the device and the electronics can be improved.

## 1.5 Outline of work

In order to isolate the acoustic effects in the system, hybrid computational aeroacoustic methods based on a perturbation ansatz are applied [3]. This allows the separation of the hydrodynamic and acoustic pressures in the device, which is near to impossible to achieve through conventional measurement methods. The following chapter will focus on the derivation of the acoustic analogy used in the computational method such that the elemental physics may be well understood. Chapter 3 will provide a description of the numerical models deployed in the hybrid numerical method, followed by chapter 4, in which the consequential numerical results are presented. These include the fluid dynamic, aero- and vibroacoustic findings. The verification of the mechanical simulation output using measurements on a gas calibration rig with a laser vibrometer is provided in chapter 5, supplementary to further numerical verifications of the simulation method. Through a detailed analysis of the pressure distributions and mechanical displacements in the frequency domain, an increased understanding of the source of the errors is achieved and detailed in chapter 6. This allows the identification of optimization techniques to improve the system, which are discussed and verified in the final chapter. The thesis concludes with a summary of the work and an outlook to future possibilities.

## CHAPTER 2

---

# Computational Aero- and Vibroacoustics

---

There are several difficulties surrounding in-duct source identification methods. The sound source is aeroacoustic, which does not allow measurement of the surface velocity using a laser vibrometer or accelerometer. Due to the presence of the flow, a measured acoustic pressure signal is corrupted by the flow generated pressures, pseudo sound and external sources [33]. Measurements with a microphone array may be corrupted by sound produced by other components in the system such as pumps and valves. Thus for investigation of the acoustics in the near-field, computational aeroacoustics is a useful tool to identify pure acoustic effects without the superposition of the large scale hydrodynamic field. In order to achieve this certain aeroacoustical methods need to be applied, as introduced in the previous chapter. First the equations of general fluid mechanics will be introduced, followed by their use to derive the acoustic analogies. This produces a relation between the flow and acoustic quantities and allows an aeroacoustic analysis. The analysis will be extended

to vibroacoustics using direct mechanical acoustic coupling.

## 2.1 Equations of fluid mechanics and the general wave equation

Three components are required for an aeroacoustic formulation: a description of the flow field, a description of the acoustic field and a coupling between the two. The basic equations for these scientific descriptions originate from the conservation laws of mass, momentum, energy and state. These basic laws are used to build the general wave equation, which is further used in the aeroacoustic computations.

The first conservation law states that the total mass of the fluid does not change in time and is conserved within the fluid motion. The mass of a system cannot be created or destroyed. The Eulerian form of the conservation of mass is defined using the density and reads as

$$\frac{\partial \rho}{\partial t} + \nabla \cdot (\rho \mathbf{u}) = 0, \quad (2.1)$$

in which  $\rho$  denotes the density of the medium and  $\mathbf{u}$  the flow velocity field. The equation of momentum conservation is related to Newton's second law, stating that momentum can only be changed within a system due to the action of external forces. For fluid applications this law is given as

$$\frac{\partial \rho \mathbf{u}}{\partial t} + \nabla \cdot (\rho \mathbf{u} \otimes \mathbf{u}) = -\nabla p + \nabla \cdot \boldsymbol{\tau} + \mathbf{f} \quad (2.2)$$

where  $\boldsymbol{\tau}$  is the viscous stress tensor and  $\mathbf{f}$  is any force field density acting on the fluid. An alternative form of (2.2) often used in the description of momentum conservation may be written as

$$\frac{\partial \rho \mathbf{u}}{\partial t} + \nabla \cdot (\rho \mathbf{u} \otimes \mathbf{u} + p \mathbf{I} - \boldsymbol{\tau}) = \mathbf{f}. \quad (2.3)$$

In this description  $\mathbf{I}$  is the identity tensor of the third dimension, with the momentum flux tensor

$$\boldsymbol{\pi} = \rho \mathbf{u} \otimes \mathbf{u} + p \mathbf{I} - \boldsymbol{\tau}. \quad (2.4)$$

Similar to the first two conservation laws, the conservation of energy law states that energy can neither be created or destroyed, but is instead transformed to other forms. The description in terms of internal energy in the final Eulerian form is described as the change in heat and change of work

$$\rho \frac{De}{Dt} - \nabla \cdot (k \nabla T) + \nabla \cdot (\mathbf{T} \mathbf{U}) - \mathbf{u} \cdot (\nabla \cdot \mathbf{T}) \quad (2.5)$$

in which  $e$  is the total internal energy and  $k$  the thermal conductivity obtained from the heat flux. Equation (2.5) makes use of the substantial derivative  $\frac{D}{Dt}$ , which will be used frequently in the aeroacoustic descriptions and is defined as the rate of change of a quantity subjected to a space-and-time dependant velocity field

$$\frac{D}{Dt} = \frac{\partial}{\partial t} + \mathbf{u} \cdot \nabla. \quad (2.6)$$

In the case of non viscous problems, the dynamic viscosity tends to zero and the Reynolds number becomes infinite. Thereby all viscosity related terms in the momentum and energy conservation equations become zero [1]. If additionally all external sources are neglected one can give the reduced Euler equations based on simplifications of (2.1), (2.2) and (2.5), again making use of the substantial derivative:

$$\frac{D\rho}{Dt} + \rho(\nabla \cdot \mathbf{u}) = 0 \quad (2.7)$$

$$\rho \frac{D\mathbf{u}}{Dt} + \nabla p = 0 \quad (2.8)$$

$$\rho \frac{De}{Dt} + \rho(\nabla \cdot \mathbf{u}) = \nabla \cdot (k \nabla T). \quad (2.9)$$

The final law, for conservation of state, can be defined in case of a perfect gas with constant temperature and entropy as

$$e = c_v T + \frac{p}{\rho(\gamma - 1)}, \quad (2.10)$$

## 2.1 Equations of fluid mechanics and the general wave equation

---

in which  $\gamma$  gives the specific heat ratio defined by the specific heat constants for pressure and volume,  $\gamma = c_p/c_v = 1.4$  for air. Using this law, (2.9) may be written in terms of the pressure

$$\frac{Dp}{Dt} + \gamma p \nabla u = (\gamma - 1) \nabla \cdot (k \nabla T). \quad (2.11)$$

In order to come from the descriptions of the fluid field to the general wave equations, the Euler equations need to be linearized [28]. These linearized equations can be obtained by splitting the flow field variables,  $p$ ,  $\rho$  and  $\mathbf{u}$ , into mean and fluctuating components with

$$p = \bar{p} + p'; \rho = \bar{\rho} + \rho'; \mathbf{u} = \bar{\mathbf{u}} + \mathbf{u}'.$$

The overlined quantities refer to the temporal mean field whereas the prime variables are the fluctuating components. Application of this splitting to the set of Euler equations above with  $\bar{\mathbf{u}} = 0$ , a constant density  $\bar{\rho} = \rho_0 = \text{const}$  [28] and additionally assuming that the perturbations are small enough to justify a linearization we obtain the conservation equations of linear acoustics

$$\frac{1}{c^2 \rho_0} \frac{\partial p_a}{\partial t} + \nabla \cdot \mathbf{u}_a = 0, \quad (2.12)$$

$$\rho_0 \frac{\partial \mathbf{u}_a}{\partial t} + \nabla p_a = 0 \quad (2.13)$$

in terms of the acoustic pressure and particle velocity quantities  $p_a$  and  $\mathbf{u}_a$  for a homentropic medium where  $p' = c_0^2 \rho'$ . Eliminating the acoustic particle velocity yields the general wave equation in its pressure formulation [28]

$$\frac{1}{c_0^2} \frac{\partial^2 p_a}{\partial t^2} - \Delta p_a = 0. \quad (2.14)$$

## 2.2 Aeroacoustic Equations

The coupling between the acoustic and flow fields was first presented by M.J. Lighthill. Lighthill extended on the general wave equation and formulated the science of how sound is created, see [34] and [35]. Sound is a linear mechanical vibration of a medium and can be described in terms of any one of several variables, including pressure and density fluctuations, and originates from a specific source. What is regarded as the source obviously depends on the choice of variable. Lighthill worked primarily with the density fluctuation because of the central part compressibility plays in sound.

Lighthill's acoustic analogy states that any fluctuating density field in a real medium, either fluid or solid, can be regarded as a superposition of quadrupole driven sound waves, with the strength of the quadrupole needed per unit volume being the Lighthill tensor  $T_{LH}$  [36]. This idea can be applied for example to the turbulences in a fluid flow. Considering the conservation of momentum from (2.2) neglecting any forces  $\mathbf{f}$ , we rearrange the terms to one side

$$\frac{\partial \rho \mathbf{u}}{\partial t} + \nabla \cdot (\rho \mathbf{u} \otimes \mathbf{u}) + \nabla p - \nabla \boldsymbol{\tau} = 0. \quad (2.15)$$

When the considered fluid is at rest, such that there are no turbulences or density fluctuations, and the viscous effects are neglected the description becomes

$$\frac{\partial \rho \mathbf{u}}{\partial t} + c_0^2 \nabla \rho = 0. \quad (2.16)$$

The difference between these two cases is simply the stress distribution  $T_{LH}$ ,

$$\nabla \cdot (\rho \mathbf{u} \otimes \mathbf{u}) + \nabla p - \nabla \boldsymbol{\tau} - c_0^2 \nabla \rho = \nabla \cdot \mathbf{T}_{LH}, \quad (2.17)$$

which is called the Lighthill stress tensor. It is now asserted that the sound generated by the turbulence in the real fluid is exactly equivalent to that produced in the ideal, stationary acoustic medium forced by the



above stress distribution [37]. The application of (2.17) as a source to (2.16) gives

$$\frac{\partial \rho \mathbf{u}}{\partial t} + c_0^2 \nabla \rho = -\nabla \cdot \mathbf{T}_{\text{LH}}. \quad (2.18)$$

By further taking the divergence of the above equation and using the conservation of mass (2.1), an inhomogeneous wave equation describing the radiated sound field of a turbulent flow region into a medium at rest is obtained

$$\frac{\partial^2 \rho}{\partial t^2} - c_0^2 \Delta \rho = \nabla \cdot (\nabla \cdot \mathbf{T}_{\text{LH}}), \quad (2.19)$$

or in pressure form

$$\frac{1}{c_0^2} \frac{\partial^2 p}{\partial t^2} - \Delta p = \nabla \cdot (\nabla \cdot \mathbf{T}_{\text{LH}}). \quad (2.20)$$

Lighthills equation is the very first aeroacoustic analogy which takes the sound sources from the fluid flow and applies them to an acoustic description. By solving the partial differential equation, and applying the correct boundary conditions on the solid bodies present, all sound sources are considered. This has been investigated in various studies, for example by Gloerfelt [38] who has shown that the surface distribution of dipoles from other acoustic analogies which specifically specify the solid surfaces in the aeroacoustic equations, in this case Curle's analogy, is equivalent to the scattering of sound waves generated by the volume distribution of quadrupoles by the rigid surface as defined by Lighthill. There are two simplifications to (2.20). The first neglects viscous dissipation and assumes the Lighthill source is obtained by an incompressible, low Mach number simulation and the main source of sound is vortex born. In this case the Lighthill tensor may be approximated by

$$\mathbf{T}_{\text{LH}} \approx \rho_0 \mathbf{u} \otimes \mathbf{u}. \quad (2.21)$$

The second simplification holds for incompressible flows where the divergence of the velocity field is zero, the density can be assumed as con-

stant and the incompressible pressure  $p_{ic}$  is substituted

$$\nabla \cdot \nabla \cdot \mathbf{T}_{LH} = \Delta p_{ic}. \quad (2.22)$$

Using this incompressible form of the Lighthill equation,

$$\frac{1}{c_0^2} \frac{\partial^2 p}{\partial t^2} - \nabla p = -\Delta p_{ic}, \quad (2.23)$$

we can use the splitting technique to separate the fluctuating pressure  $p'$  into its incompressible and acoustic components  $p = p_{ic} + p_a$ , giving

$$\frac{1}{c_0^2} \frac{\partial^2 p_{ic} + p_a}{\partial t^2} - \Delta(p_{ic} + p_a) = -\Delta p_{ic}. \quad (2.24)$$

After simplifying we arrive at the aeroacoustic wave equation

$$\frac{1}{c_0^2} \frac{\partial^2 p_a}{\partial t^2} - \Delta p_a = -\frac{1}{c_0^2} \frac{\partial^2 p_{ic}}{\partial t^2}, \quad (2.25)$$

which serves as a good estimation of the acoustic pressure in a fluid, while neglecting the mean flow. This aeroacoustic formulation can also be derived using the acoustic perturbation equations (APE). Although this equation clearly describes physically correct wave propagation, it has two flaws. Firstly, it neglects the mean flow field and secondly, the source term involves the second time derivative of the fluid pressure whose computation is very sensitive to numerical noise in the given flow field [3]. To overcome this drawback, Hüppe [3] has used the scalar acoustic potential using the identity  $\mathbf{u}_a = -\nabla \varphi_a$ . Using this relation results in the convected wave equation with an incompressible source term which considers the mean flow of the fluid

$$\frac{D^2 \varphi_a}{Dt^2} - \nabla \cdot \nabla \varphi_a = -\frac{1}{c_0^2} \frac{D p_{ic}}{Dt}. \quad (2.26)$$

With this convected wave equation, and since the acoustic and hydrodynamic quantities have been separated, it is now possible to use the incompressible pressure and mean flow field results from a fluid dynamic

analysis to resolve the acoustic nature of the system.

## 2.3 Mechanic-Acoustic Coupling

For a full vibroacoustic analysis, a mechanical field needs to be introduced. The mechanical field is described according to the partial differential equation of form [32]

$$\rho \frac{\partial^2 \mathbf{u}}{\partial t^2} - B^t \sigma = \mathbf{f}_v, \quad (2.27)$$

which originates from the conservation of momentum. Here  $\mathbf{u}$  is the displacement,  $B$  is the differential operator in Voigt notation and  $\mathbf{f}_v$  is any external force acting on the system, usually set to zero. The acoustic field  $p_a$  can be described using the wave equation, here also considering an acoustic source  $F$

$$\frac{1}{c_0^2} \frac{\partial^2 p_a}{\partial t^2} - \Delta p_a = F. \quad (2.28)$$

To solve such a multiphysics system involving both mechanical and acoustic descriptions, the coupling of the two fields needs to be constructed. For the case of a vibroacoustic system, the coupling ensures the continuity of velocities and pressure forces at the fluid-solid boundary. The continuity of velocities holds for the normal components of the mechanical and particle velocities,  $\mathbf{v}_m$  and  $\mathbf{v}_a$  respectively, at the boundary surface [32]

$$(\mathbf{v}_m - \mathbf{v}_a) \cdot \mathbf{n} = 0. \quad (2.29)$$

By taking the time derivative

$$\left( \frac{\partial \mathbf{v}_m}{\partial t} - \frac{\partial \mathbf{v}_a}{\partial t} \right) \cdot \mathbf{n} = 0, \quad (2.30)$$

and using the equation of linear momentum,  $\rho_0 \frac{\partial \mathbf{v}_a}{\partial t} = -\nabla p_a$ , the first coupling condition between the acoustic pressure and mechanical dis

placement is obtained

$$\rho_0 \frac{\partial^2 \mathbf{u}}{\partial t^2} \cdot \mathbf{n} = - \frac{\partial p_a}{\partial n} \quad (2.31)$$

with the mechanical displacement  $\mathbf{u}$  substituted for  $\partial \mathbf{u} / \partial t = \mathbf{v}_m$ . The second coupling condition using the continuity of pressure is much simpler, with the normal component of acoustic pressure on the solid directly equal to the resulting surface pressure force in the same direction [32]

$$\boldsymbol{\sigma}_n = -p_a \mathbf{n}. \quad (2.32)$$

With application of test functions  $\boldsymbol{\alpha}$  and  $\theta$  and the coupling conditions (2.31) and (2.32), the two partial differential equations (2.27) and (2.28) can be written in the final weak formulation for the finite element analysis in terms of the acoustic pressure  $p_a$  and  $\mathbf{u}$

$$\int_{\Omega} \rho \boldsymbol{\alpha} \cdot \frac{\partial^2 \mathbf{u}}{\partial t^2} d\Omega + \int_{\Omega} (B \boldsymbol{\alpha})^t [c] (B \mathbf{u}) d\Omega + \int_{\Gamma} \boldsymbol{\alpha} \cdot \mathbf{n} p_a d\Gamma = \int_{\Omega} \boldsymbol{\alpha} \cdot \mathbf{f}_v d\Omega, \quad (2.33)$$

$$\int_{\Omega} \theta \frac{1}{c_0^2} \frac{\partial^2 p_a}{\partial t^2} d\Omega + \int_{\Omega} \nabla \theta \nabla p_a d\Omega - \int_{\Gamma} \theta \ddot{\mathbf{u}} \cdot \mathbf{n} d\Gamma = \int_{\Omega} \theta F d\Omega. \quad (2.34)$$

Performing the space discretization by finite elements, results

$$\begin{pmatrix} M_u & 0 \\ -M_{pu} & M_p \end{pmatrix} \begin{pmatrix} \ddot{\mathbf{u}} \\ \ddot{\mathbf{p}} \end{pmatrix} + \begin{pmatrix} K_u & K_{up} \\ 0 & K_p \end{pmatrix} \begin{pmatrix} \mathbf{u} \\ \mathbf{p} \end{pmatrix} = \begin{pmatrix} \mathbf{f}_u \\ 0 \end{pmatrix}. \quad (2.35)$$

This matrix system contains two equations for two unknowns across both physic domains, and thus achieves a full vibroacoustic description of the solution. For more detail see [32].

# CHAPTER 3

---

## Numerical Models and Simulation

---

The computational aero and vibroacoustic methods described in chapter 2 are now applied on dual-channel mass flow devices in order to identify the main acoustic source regions and to quantify the effect of the produced acoustic pressures on the mechanical ducts. First the geometrical models relevant for the investigation will be introduced, followed by details on the numerical fluid dynamic and vibroacoustic simulation setups, which produce the best results for investigations on multi channel duct systems.

### 3.1 Geometrical Models

In order to obtain a broad understanding of the aeroacoustic effects in dual-channel mass flow meters, three different constructions are considered. All constructions have a nominal diameter of 50 mm at the inlet and outlet ducts, are built using the same stainless steel materials and are analysed when transporting air with 10 bar at room temperature. The

parallel measuring tubes are all of the same inner diameter 26 mm with a wall thickness of 1.5 mm. Differences, however, can be found in the length and shape of the two parallel measuring ducts, as seen in figure 3.1.

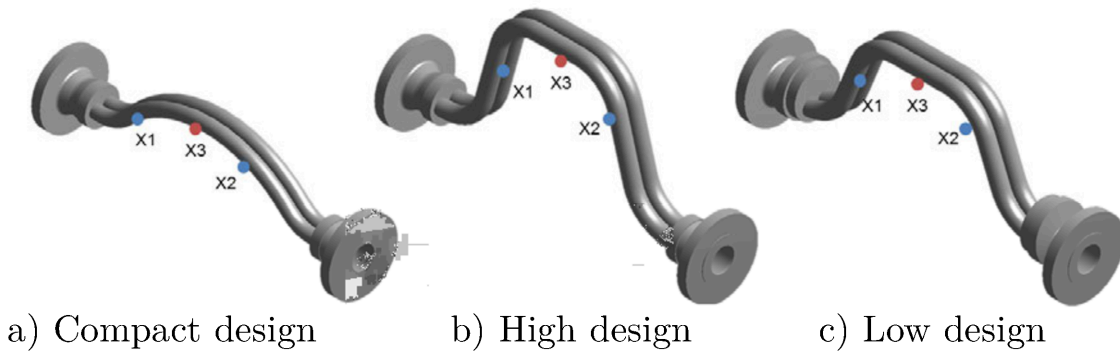


Figure 3.1: The three flow meter designs used for the aeroacoustic analysis a) compact design, b) high design and c) low design with marked monitoring points at the sensors (blue) and at the driver (red).

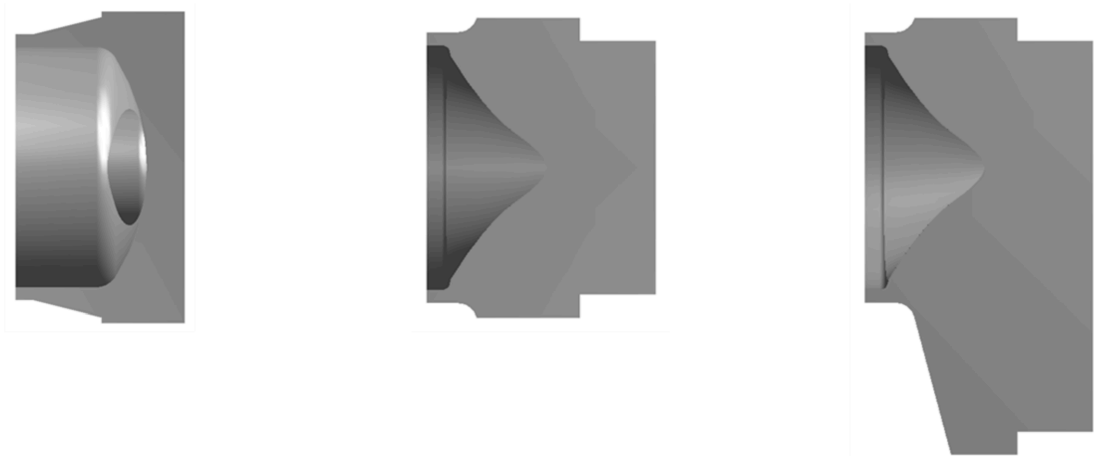
The measuring ducts in the first construction, labeled *compact*, form a flatter and smoother arch with continual radii bends. The *high* variant is constructed with more elevated u shaped measuring ducts containing sharper bends. The *low* variant is similar in construction to the *high* variant, except that the measuring ducts form a rather smaller u arch. All ducts are of the same diameter and have the same wall thickness; the measuring ducts however differ in their total length and height as listed in table 3.1 below.

Table 3.1: Comparison of the total length and height of the measuring tubes of different devices.

	Total length	Height
<i>Compact</i>	615 mm	106 mm
<i>High</i>	870 mm	258 mm
<i>Low</i>	765 mm	219 mm

The points of interest, marked with an  $X$  in figure 3.1, are assigned as monitoring points. These are placed on both measuring ducts at the sensor inlet position, sensor outlet position and at the center driver. An additional monitoring point is also placed at the flow splitter outlet.

In addition to the differing measuring tube forms, the three constructions also differ in the contours of the flow splitters. Cross-sections through the flow splitter geometries are shown in figure 3.2. The flow splitter is the geometrical component in the device which divides the flow from the inlet duct into two separate flows in the measuring tubes, and subsequently joins the two flows again before the outlet duct. The flow splitter of the *compact* variant is very rounded, while the *high* and *low* variants have a nose between the two ducts with similar expansion or contractions profiles. The diameters of the measuring ducts and the process line duct diameter,  $D$ , are constant for all models. The *low* variant flow splitter has more mass on the underside of the splitter than the other two designs.



a) Compact design

b) High design

c) Low design

Figure 3.2: Side cut-view of the flow splitters from the a) compact design, b) high design and c) low design.

The devices are modelled from inlet flange to outlet flange, with the fluid region extending  $5D$  and  $15D$  further up and downstream from the inlet and outlet, respectively. The outer mechanical housing, electronics

as well as the sensor and driver components as displayed in figure 1.1 are assumed to have a negligible effect on the aeroacoustic system and are not included in the numerical models.

## 3.2 Fluid Dynamic Simulation

The initial step in the hybrid method depicted in the flowchart of figure 1.6, is a fully turbulent and transient simulation of the fluid mechanics. In order to be able to solve (2.26), this means an incompressible simulation. For this purpose, the internal volume of the device geometries described above is extracted using a CAD modeller to form the fluid body. As mentioned above, the inlet and outlet ends are extended beyond the flanges to allow investigation of the flow regions before and after the devices. The three resulting fluid regions derived from the mechanical geometries are shown in figure 3.3. The fluid modeling and simulation is conducted using StarCCM+ V9.02.007 double precision software. All boundaries, where a duct geometry would be present, are set as walls, except for the velocity inlet and pressure outlet set at the appropriate duct ends.

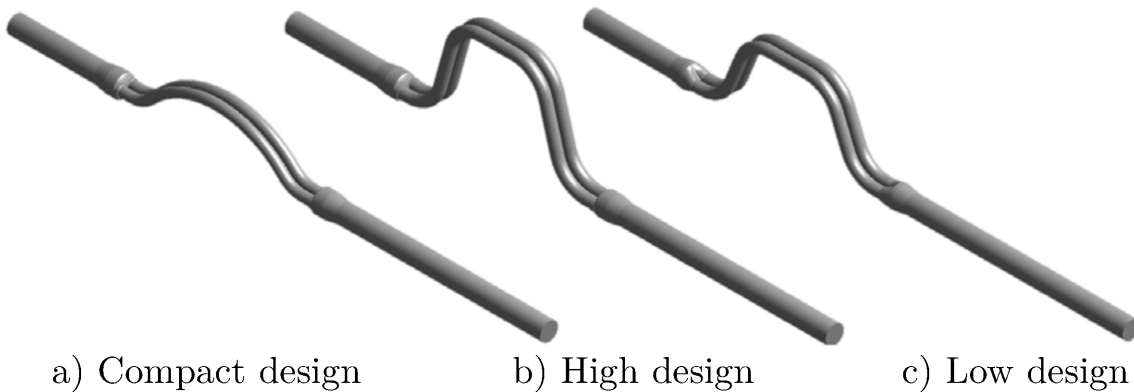


Figure 3.3: The extracted and extended fluid regions for the fluid dynamic simulation of the three constructions.

It is important to have both an adequate mesh and time step size,  $h$  and  $\Delta t$  respectively, not only for a good convergence of the solution but



such that the required frequency domain is obtained to the appropriate resolution. This can be defined using the maximum desired frequency  $f_{\max}$  and the corresponding minimum wavelength  $\lambda_{\min}$

$$\Delta t \approx \frac{1}{20f_{\max}}, \quad (3.1)$$

$$h \approx \frac{\lambda_{\min}}{20}. \quad (3.2)$$

The fluid region was meshed using polyhedral elements of base size 1.5 mm to 3 mm, depending on the Reynolds number of the flow. The use of polyhedral elements greatly accelerated solution convergence compared to hexahedral elements. Seven boundary layer elements were defined along the duct walls, and a 50% mesh refinement was applied over the device domain between the flanges. A  $y^+$  value around 30 was ensured and an all  $y^+$  wall treatment model in StarCCM+ was applied. Figure 3.4 shows an example of the mesh with the *compact* design for a low Reynolds number. Due to the large model and small element sizes, the representation has been separated into the middle and end regions. The chosen mesh size allows a wavelength resolution of up to 30 mm, which is more than adequate for this investigation. The mesh has been extended with the element size stretched at the inlet and outlet of the fluid region, also shown in figure 3.4. This deems important for the degradation of energy leaving the system, and aids against any additional reflections at the inlet and outlet boundaries which would overlay the true results. The meshes contain between one and three million cells depending on the geometry and simulated Reynolds number. The time step for the solver is set between 15  $\mu\text{s}$  and 10  $\mu\text{s}$  depending on the Reynolds number and mesh resolution. This enables a subsequent acoustic analysis of frequencies up to 3000 Hz.

The velocity inlet and pressure outlet are adequate boundaries for an incompressible simulation, since there are no compressible pressures to be reflected back into the system. In compressible simulations, free stream boundaries offered in StarCCM+ should be used to reduce these reflections, at least in one dimension. Additionally, as mentioned before, the

mesh size should be gradually increased towards the inlet and outlet to diminish the energy fluctuations leaving the system. The velocity inlet is initialized using an axi-symmetric, fully developed velocity profile for each analyzed flow rate obtained from previous periodic simulation runs on the inlet diameter.

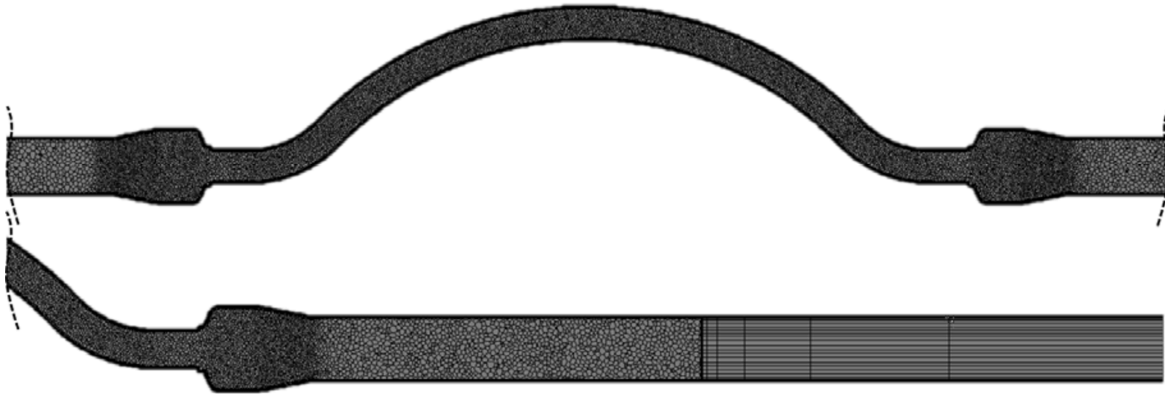


Figure 3.4: An example of the mesh used in the fluid dynamic models with a refinement on the measuring ducts (top) and element extensions at the inlet and outlet ducts (bottom).

With this setup, an initial steady simulation was run for 2500 time steps, from which the sequential transient Detached Eddy Simulation is initialized. The formulation option is set as delayed detached eddy, which shows improvement of the transition from RANS to LES models independent of grid spacing. An implicit unsteady method has been applied for the increased stability range and for the improved performance by unsteady problems, at second order for higher accuracy [40]. A coupled solver is used for its robustness in high velocity flows on a fine mesh with dominant source terms [41]. If convergence problems were encountered then the  $k$   $\omega$  turbulence and  $k$   $\omega$  turbulent viscosity under relaxation factors were lowered. The W cycle was chosen for the Algebraic Multi Grid (AMG) linear solver which improves results in stiff systems by using coarse relaxation sweeps. The group size for the cycling was set to eight. This sets the number of equations

on a given multigrid level that are agglomerated to form one equation on the next coarsest level [40]. A large group size was chosen considering previous studies which have shown that smaller group sizes tend to overestimate the peaks in pressure amplitudes. The incompressible transient simulation required a run time of 0.3 s before the solution stabilized. Conclusively the transient simulation was run for a further 0.1 s, with the incompressible pressure read out over the entire volume mesh at each time step. Additionally, the incompressible pressure over time was recorded at all monitoring points marked with an X in figure 3.1. Finally the mean velocity field for the final time period was calculated and recorded. All the data was saved as an Enight case file for each geometry at four different Reynolds numbers ranging between 0.7 million and 1.8 million, corresponding to a Mach number between 0.06 and 0.15 in the process line, and between 0.1 and 0.28 in the smaller measurement ducts. The CFD simulations were completed using a StarCCM+ student license on the vienna scientific cluster.

### 3.3 Acoustic-Mechanical Simulation

The stored data from the fluid dynamic simulations is then used to calculate the acoustic source terms on the right hand side of (2.26). The source terms are then interpolated on to a vibroacoustic mesh according to the workflow in figure 1.6. The convective wave equation according to (2.26) may now be solved for each time step. The vibroacoustic simulation was conducted using the multiphysics software CFS++ [32]. The vibroacoustic mesh contains both acoustic and mechanical regions, and allows a much larger element size for an adequate solution accuracy since the wavelengths and displacement amplitudes are of a larger scale, see figure 3.5. The mesh contains between 100'000 and 300'000 hexahedral elements and it must be assured that even in intricate regions of the geometries the new mesh elements are larger in size than the corresponding CFD elements. This is important for the interpolation method of the source term values between the meshes. Furthermore, two additional regions need to be defined at the inlet and outlet of the acoustic region,

which will serve as non-reflective boundary regions. Since such boundaries may be defined in the acoustic analysis, there is no longer need to extend the mesh and stretch the element size at the inlet and outlet ducts. These regions are meshed using the same element size as in the acoustic region with a minimum of four layers in the main direction of propagation.



Figure 3.5: An example of the vibroacoustic mesh of the compact geometry with acoustic, mechanical and boundary regions.

The boundary conditions in the acoustic simulation have a large influence on the accuracy of the results. Reflections of the acoustic waves at the duct inlet and outlet boundaries need to be addressed to avoid a falsification of the results. In the real world, the acoustic waves present in the line would eventually be reflected at an obstruction or bend in the duct network, but this is unpredictable and inconsistent between application setups. Any reflections within the duct network will thus be neglected in this work. The inlet and outlet boundaries are modelled such that the duct is numerically infinite. The use of homogeneous Dirichlet ( $p_a = 0$ ) or Neumann ( $\partial p_a / \partial n = 0$ ) boundary conditions would result in total reflection. Thus two main acoustic boundary conditions have been defined to prevent this: absorbing boundary conditions (ABC) or perfectly matched layers (PML).

Absorbing boundary conditions [32] allow the acoustic waves to pass through the boundary in only one direction. The waves exit the system, and then are not allowed to re enter the computational domain, see the top of figure 3.6 for a depiction of this boundary. This is achieved by introducing the following condition

$$\left(\frac{\partial}{\partial t} + c\frac{\partial}{\partial x}\right)p_a = 0. \quad (3.3)$$

Waves travelling in the positive x direction  $p_{a,+}(x, t) = p_0 e^{j(\omega t - kx)}$  will be allowed to pass through since condition (3.3) is satisfied

$$\left(\frac{\partial}{\partial t} + c\frac{\partial}{\partial x}\right)p_a = j\omega p_0 e^{j(\omega t - kx)} + c(-jk)\omega p_0 e^{j(\omega t - kx)} = 0. \quad (3.4)$$

However, waves travelling in the negative x direction  $p_{a,-}(x, t) = p_0 e^{j(\omega t + kx)}$  will be reflected, because condition (3.3) is no longer satisfied

$$\left(\frac{\partial}{\partial t} + c\frac{\partial}{\partial x}\right)p_a = j\omega p_0 e^{j(\omega t - kx)} + c(jk)\omega p_0 e^{j(\omega t + kx)} \neq 0. \quad (3.5)$$

This boundary condition can be extended into three dimensions, however it is only ideal if all the waves impinge orthogonal to the boundary. Otherwise, part of the wave will be absorbed and part reflected back into the system.

An improved technique for acoustic boundaries is the perfectly matched layer condition [39]. Here, an additional region is introduced surrounding the system boundary which works as a damping region, also pictured in figure 3.6. The interface between the layers is constructed such that the acoustic impedances  $Z_a$  of the neighbouring regions are exactly matched, which ensures there are no reflections at the interface between the layers. In the perfectly matched layer region, a damping function  $\sigma$  is applied

$$p_0 e^{j(\omega t - \tilde{k}x)} = p_0 e^{j(\omega t - kx)} e^{-k\sigma x} \quad (3.6)$$

such that the acoustic wave is fully diminished as it leaves the system. This technique performs well in three dimensions with individual considerations in each direction, and thus can also be used in cases involving oblique waves at the boundary. It is the PML technique that is applied here; a visualization of the boundaries used in the analysis may be found

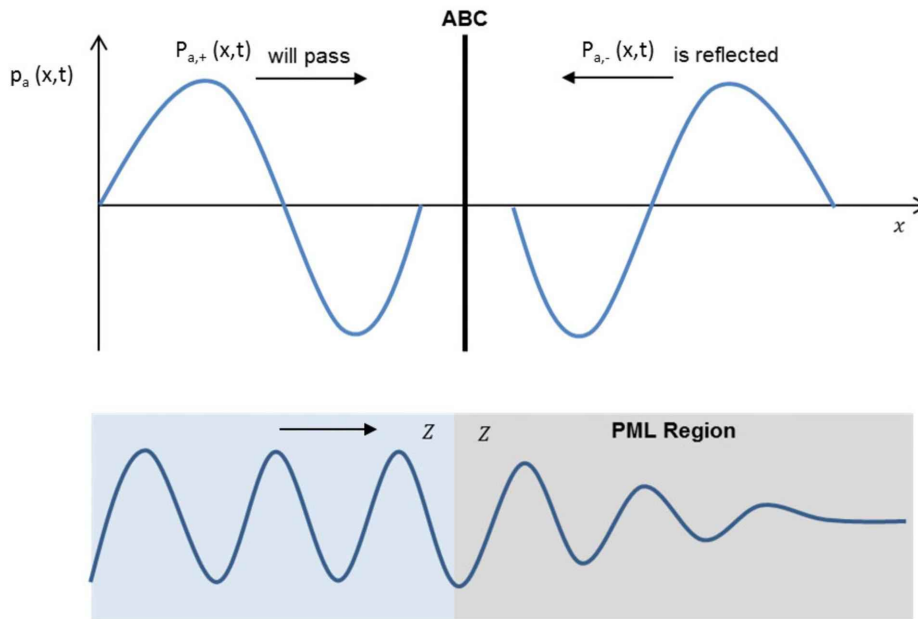


Figure 3.6: Visual representation of the ABC (top) and PML (bottom) boundary condition

in figure 3.7, where the acoustic, mechanical and coupling boundary definitions are shown. For the mechanical solution, fixed boundaries are defined at the flange surfaces, and for the coupled solution a coupling boundary is defined between the acoustic and mechanical regions. The coupling boundary is the face contact between the two regions at the inner surface of the duct. It is at this boundary that the direct coupling matrix (2.35) from section 2.3 is applied.

The number of solution steps as well as the time step are equal to that in the fluid dynamic simulation. A global factor was used to introduce the acoustic source terms to the numerical simulation for the first time steps. The factor is defined as  $1 - \cos^2(0.5\pi/15 \cdot 10^{-6}t)$ , which ensures that no acoustic shock is initialized in the system, and no overshooting of the amplitudes occur. Most settings for the numerical simulation were adopted from previous successful studies such as from Escobar [42] or Hüppe [43]. This includes a six point Gauss integration scheme and the use of the paradiso solver with a tolerance specification equal to  $1e-7$ .

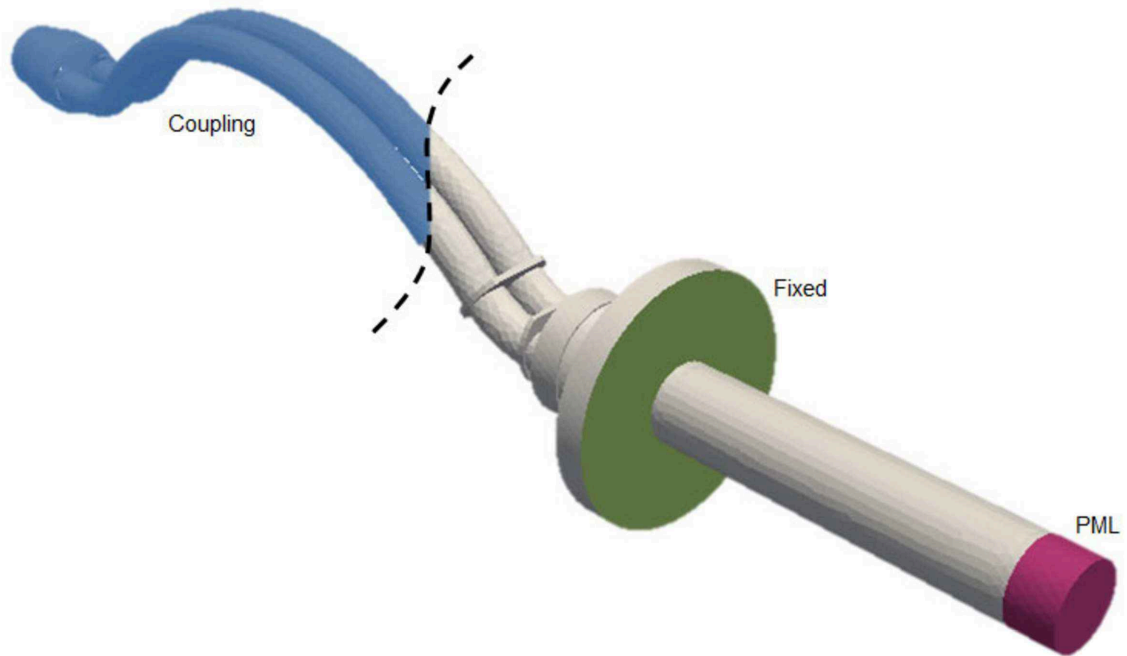


Figure 3.7: Acoustic (red), mechanical (green) and coupling (blue) boundary conditions for the vibroacoustic simulation, with the mechanical and acoustic regions shown in grey

The result is the acoustic pressure field within the acoustic (fluid) region and the mechanical displacement in the mechanic (solid) region over time. The results can be visualized in the post processing software Paraview. However, interpreting the pressure and displacement fields in the time domain is difficult. Thus a subsequential Fourier transform is performed on the pressure and displacement field data to obtain the acoustic pressures and mechanical displacement in the frequency domain. This is also done on the data from the monitoring points defined in figure 3.1. Additionally, a Fourier transform is conducted on the acoustic source term data in order to determine at what frequency the main acoustic sources in the fluid region occur. With the applied mesh size and time step a good frequency resolution could be obtained from the simulations

between 10 Hz and 3000 Hz, which is the required frequency domain to be studied for this case. In future investigations, it may be considered to reduce the time step size to improve the frequency resolution. The frequency peaks would thus be more accurately distinguishable. The mechanical displacement was obtained in X, Y and Z directions in the solid region.

The vibroacoustic analysis was conducted both with and without the excited vibration of the measuring ducts at their drive mode frequency  $f$  as shown in figure 1.2. For the case with the additional duct vibration, a sinusoidal function  $A \sin(2\pi ft)$  was applied to the driver position of both measuring tubes in opposing directions. This simulated the harmonic movement of the ducts when driven at this natural resonance frequency. The amplitude  $A$  is determined such that a maximum displacement of  $6.25 \mu\text{m}$  at the sensor positions is always achieved, in the case of the high design double the amplitude is used. Due to the different geometries, this amplitude as well as the drive mode frequency differs from device to device as listed in table 3.2 below.

Table 3.2: Drive mode frequencies and driver excitation amplitude of the device designs.

	<i>Compact</i>	<i>High</i>	<i>Low</i>
Drive Frequency [hz]	550	280	350
Amplitude Driver [ $\mu\text{m}$ ]	12.95	37.5	9.4

The method depicted in figure 1.6 is now complete. The systems have been fully described at four different Reynolds numbers in terms of fluid dynamic, acoustic and mechanical properties.



# CHAPTER 4

---

## Simulation Results

---

The numerical method from chapter three is applied for all the introduced device constructions at four Reynolds numbers between 0.7 million and 1.8 million. First the results from the fluid dynamic simulations are presented, followed by the aero and vibroacoustic results. Included in the acoustic outcome is a preliminary discussion about the different methods and definitions investigated in order to produce an optimal output for the acoustic source term in this multi duct system.

### 4.1 Fluid Dynamic Simulation Results

The fluid dynamic simulation is critical for the following aeroacoustic analysis. If the turbulent structures are not properly resolved, or there are unrealistic reflections at the inlet and outlet boundaries, the acoustic results will be falsified. One example of important modeling considerations is the mesh element stretching at the boundaries as discussed in

chapter 3. Figure 4.1 displays a comparison of the pressure levels at the driver monitoring point X3 (defined in figure 3.1) in the compact device for two differently modeled cases at a Reynolds number of 0.7 million. In the first case, mesh element stretching at the inlet and outlet boundaries was not applied and reflections of the fluctuations back into the system cause the pressure amplitudes to be overestimated. In the second case, mesh element stretching was applied at both boundaries and the pressure amplitudes improve. The peak in amplitude just above 100 Hz is probably the acoustic resonance of the entire tube length according to (1.11) since the smaller frequencies with larger wavelengths are not degraded as efficiently by the mesh stretching.

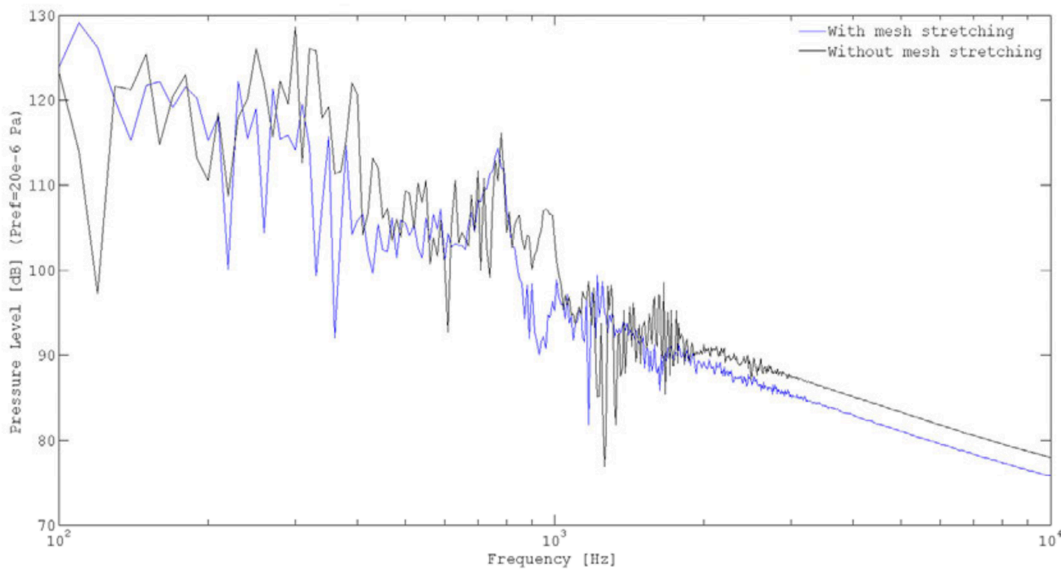


Figure 4.1: A comparison of the pressure levels in two compressible simulations of the compact design where mesh element stretching at the inlet and outlet boundaries was and was not implemented.

In all following simulations the mesh element size has thus been stretched over ten layers at the inlet and outlet boundaries, with the element size increasing hyperbolically as seen in the bottom of figure 3.4. In order to further authenticate, if the fluid simulations produce feasible results,

both compressible and incompressible simulations have been conducted with the same mesh. The pressure at the monitoring points X on the *compact* design from figure 3.1 were again monitored for the entire simulation run. Subsequently a Fourier transform was conducted on the data and the results from the two cases were plotted on the same axes, see figure 4.2. The simulations were run for all Reynolds numbers; only the results for a Reynolds number of 0.7 million and at point X1 are shown in figure 4.2.

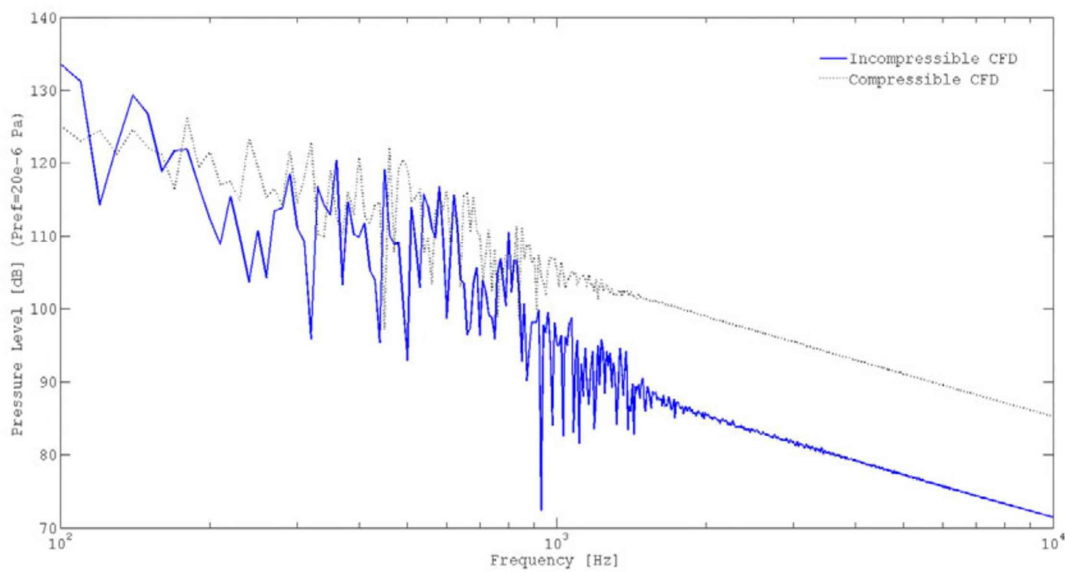


Figure 4.2: Comparison of the pressure level at monitoring point X1 in the *compact* design for a compressible and incompressible fluid simulation at a Reynolds number of 0.7 million.

The pressure level in the compressible simulation is observed to be slightly higher than that in the incompressible simulation. The compressible results also contain more peaks in the amplitude across the calculated frequency range, which is expected. The compressible model contains both acoustic and hydrodynamic pressures, while the incompressible model contains only the fluid pressure. The difference between the two plots lies thus in the acoustics. At lower frequencies the peaks in the amplitude are larger for the incompressible simulation than for

the compressible simulation. This can be attributed to increased reflections at the boundaries in the incompressible simulation case relating to an acoustic resonance of 50 Hz. Although the same mesh was used for both cases, free stream boundary conditions are only available for the compressible simulations in StarCCM+. The free stream boundary conditions are advantageous in that they are non-reflecting in the direction perpendicular to the flow, and thus handle the reflections at the boundaries more successfully than the velocity inlet and pressure outlet defined in the incompressible simulation. This must be taken into consideration when evaluating the ensuing acoustic results from the incompressible simulations, however at the moment this cannot be further optimized.

The fluid dynamic simulation was completed for all three constructions at Reynolds numbers 0.7 , 1.1 , 1.4 and 1.8 million. The most turbulent areas in the flow can be visualized using the Q-Criterion, as seen in figure 4.3 for the *compact* geometry at the highest Reynolds number. The main turbulent areas in all geometries occur at the outlet flow diverter, as well as at the inlet and bends. The highest turbulent area, for all cases and all Reynolds numbers occurs just behind the flow diverter at the device outlet where the two flows from the measuring tubes are joined. A large separation region is formed here along with many eddies.

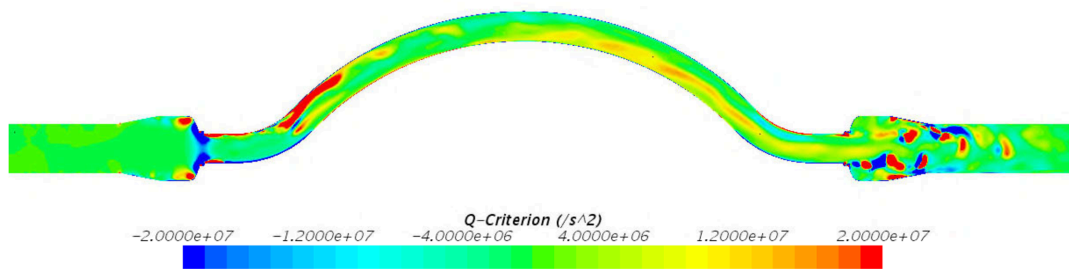


Figure 4.3: A visualisation of the turbulent areas in the *compact* geometry at a Reynolds number of 1.8 million using the Q Criterion.

The magnitude of the mean velocity in the *compact* device is shown in figure 4.4, with large velocity gradients at the flow diverters and also at the bends in the measuring tubes. The location of the main turbulences

in the three geometries is quite constant over all designs and Reynolds numbers. Since it is in these turbulent regions that the most pressure fluctuations occur, it is assumed that the main acoustic source also occurs in these regions. This can be confirmed by the following acoustic analysis.

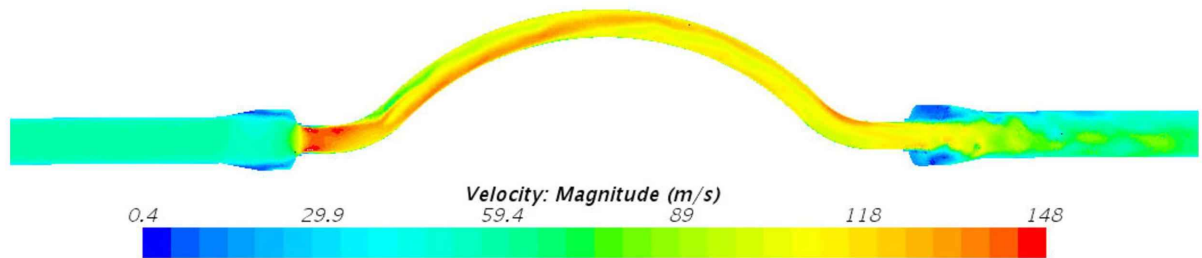


Figure 4.4: The velocity field in the *compact* geometry at the highest Reynolds number of 1.8 million at the end time step.

## 4.2 Vibroacoustic Simulation Results

### 4.2.1 Comparison of numerical approaches

The acoustic source term on the right hand side of Lighthills equation may be calculated in the interpolation script from data obtained in the fluid computation in different forms. If we use the incompressible case, then the most basic data set of the pressure and the mean velocity over time is used to calculate the acoustic source term as in (2.25). Additionally, the Laplace of the incompressible pressure may be read directly out from the fluid simulation and used to solve (2.23). Thus, the source term may also be partially computed in the fluid simulation before the interpolation script is executed, which also holds for compressible simulation cases. For example, the Laplace of the Lighthill tensor or similarly the divergence of the Lighthill tensor may be read out of the fluid simulation and used to solve (2.20). These options, using the direct incompressible pressure, the Laplace of the incompressible pressure and the divergence of the Lighthill tensor, were analysed for the compact geometry at monitoring point X1

## 4 Simulation Results

for a Reynolds number of 0.7 million. The resulting acoustic pressures from the subsequent acoustic simulations are plotted for each case in figure 4.5 in the frequency domain. Please note that the plot describing the divergence of the Lighthill tensor lies directly beneath the plot for the Laplace of the incompressible pressure.

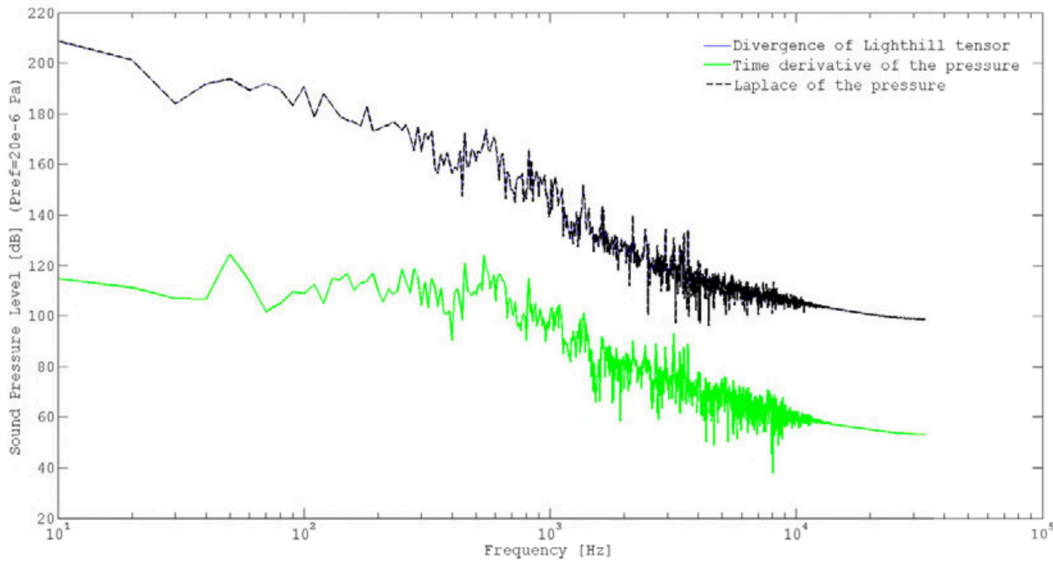


Figure 4.5: Comparison of the sound pressure level obtained in the three different source term computation cases: using the Laplace of the incompressible pressure, the second time derivative of the incompressible pressure, and the divergence of the Lighthill tensor directly from the CFD data.

The plots of the three cases reveal a similar behaviour of the acoustic pressure result over frequency, with amplitude peaks occurring mostly at the same frequencies. However, there is an overall amplitude offset between the different cases. Where the divergence of the Lighthill tensor was calculated in the fluid simulation software, the amplitude of the acoustic result is larger than expected from the results of the fluid computation in figure 4.2. This is also the case for the Laplace of the incompressible pressure calculated in the CFD software. The root cause of these offsets may lie in how the Lighthill tensor, and the divergence or

Laplace thereof, is calculated in StarCCM+. For incompressible flows, the calculation of Lighthills tensor is simplified to (2.26). In StarCCM+, however, the full Lighthill tensor according to (2.19) is still calculated, which may produce an offset. This also disregards the splitting of the acoustic and hydrodynamic pressure fluctuations such that the result is a superposition of the two pressure quantities. Furthermore, the gradient calculations in StarCCM+ differ to those in the source term calculations in the interpolation script. For the calculation of gradients in StarCCM+ a cell based least squares algorithm is used and at the boundaries zero order extrapolation is applied. This handling is different than that in the interpolation script, where the boundary elements are neglected. An additional possible discrepancy may originate from the interpolation on to the acoustic mesh. At certain regions in the geometry, where the acoustic mesh needs to be finer in order to properly resolve the geometry, such as by the intricate flow diverters, the acoustic mesh elements may not be appropriately larger than the fluid dynamic elements. Thus overlapping may occur. This would result in numerical errors when applied in the interpolation script, the extent of which is dependent on the source term form being interpolated. For the purpose of this investigation, using the pure incompressible pressure data from the fluid simulation with a subsequent second temporal derivation with respect to time achieved the most accurate results, since the full source term calculation was conducted manually in the interpolation script with no unwanted extra terms. The pressure amplitudes obtained with this method also correlated well with the fluid dynamic results seen in figure 4.2. It is thus this method which is used for the vibroacoustic analysis in this work.

### 4.2.2 Final vibroacoustic results

The interpolation of the acoustic source terms on to the vibroacoustic mesh produces the sound source over time. When this result is viewed in the frequency domain, the frequency content of the acoustic source and its main location may be identified. Using the post processing software Paraview, the acoustic source is displayed over the volume mesh at the lowest and highest Reynolds numbers. For a fair comparison, the source

is viewed at the frequency 550 Hz (drive frequency for the *compact* device) in all three devices, see figure 4.6.

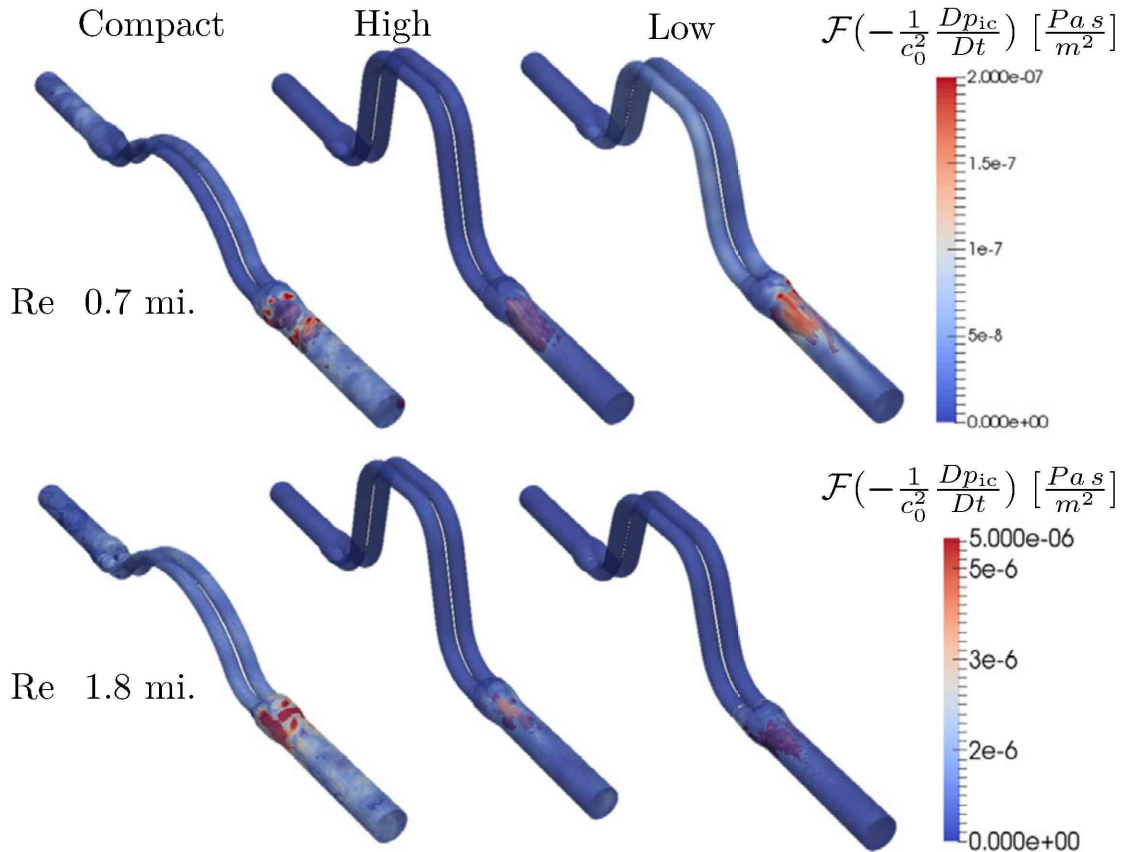


Figure 4.6: Acoustic source for the lowest and highest Reynolds numbers in all device geometries at 550 Hz.

The largest acoustic source is located at the outlet side after the flow diverter for all Reynolds numbers, geometries and also all frequencies in the studied range. The largest turbulence area identified in the fluid dynamic simulations thus corresponds to the largest acoustic source. Since this is true for all frequencies, the source is probably of a broadband nature. At a frequency of 550 Hz in figure 4.6, the amplitude of the acoustic source is comparable in all three devices over the Reynolds number range, with no device showing a much larger or smaller sound source. The nature of the turbulence is different for the three geometries due to differences in the



duct and flow diverter shape. This is reflected in the acoustic source. The amplitude of the source is similar through the devices, but the volume content differs. The *low* design has a larger volume source due to the increased turbulence in this device. The *high* and *compact* devices are similar, but the acoustic source is located closer to the duct walls in the *compact* device. This again lies in the nature of the turbulence, and the separation regions at this position in the three devices. The amplitude of the sound source increase approximately four times from a Reynolds number of 0.7 million to a Reynolds number of 1.8 million, when observing this particular frequency. It is however not so by every frequency in the studied range. At certain frequencies the acoustic source may even be larger at smaller Reynolds numbers. This phenomenon will be discussed in detail later, and again in chapter 6.

At the same Reynolds number, differences in the acoustic source can be observed across the frequency range. For example in figure 4.7 the acoustic source at three difference frequencies in the *compact* device are pictured, all at a Reynolds number of 0.7 million. It is observed that although the amplitude of the source is similar, again the volume content changes. This change is not linear with frequency, but it is larger at certain frequencies and smaller at others. This behaviour is also dependent on the frequency content of the turbulence in the ducts and will be extended upon in chapter 6.

Smaller sound source contributions can also be identified at the inlet, as well as at the radial bends in the measuring tubes. The magnitude of these sources is about ten times smaller than that of the source located at the outlet, see figure 4.8 for a direct comparison in the *compact* device. The inlet sound source increases in magnitude relative to the outlet source with increasing Reynolds number, such that the inlet source becomes more prominent with higher flow rates. This is probably due to the increased force on the surface of the inlet flow diverter when the flow is split. The acoustic source in the bends is more erratic. At certain frequencies it becomes more prominent, at others it decreases significantly, but it remains ten times smaller than the outlet source, or smaller. This behaviour is seen in all devices.

The influence of the inlet flow profile on the location of the turbulences

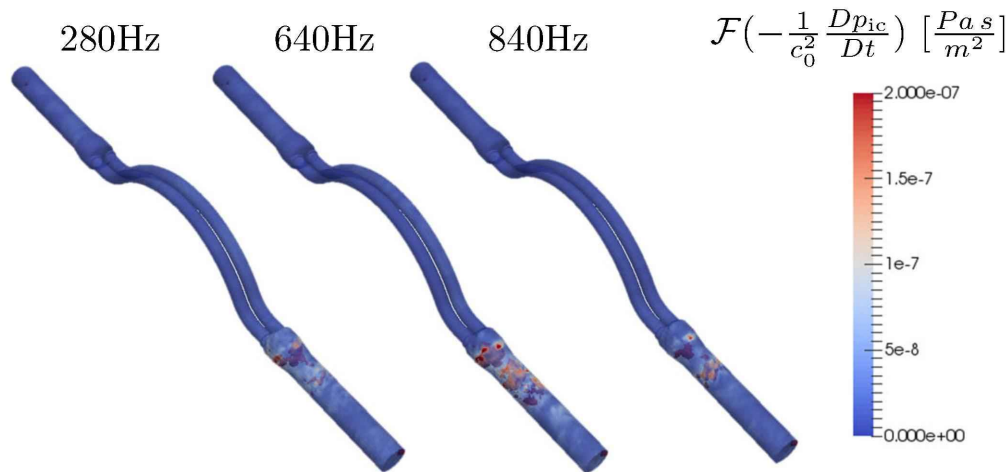


Figure 4.7: Comparison of the acoustic source at three different frequencies in the compact geometry at a Reynolds number of 0.7 million.

is also investigated. Simulations were run at all Reynolds numbers additionally with various non-axisymmetric inlet profiles. The profiles, for the cases simulated in the *compact* design, did not have an impact on the sound source location or amplitude.

Using the acoustic source data, a vibroacoustic simulation solving (2.26) and considering the coupling matrix (2.35) may now be completed. The result is the acoustic pressure in the fluid region and the mechanical displacement in the solid region over time. Firstly, the acoustic pressure is investigated at the monitoring points  $X$  named in figure 3.1. Three sound pressure level plots at monitoring point  $X1$  at the inlet sensor on one of the smaller parallel ducts for all four Reynolds numbers can be seen in figure 4.9 for the three device geometries marked *compact*, *high* and *low*.

In general, the sound pressure level increases with Reynolds number, but a clear pattern in the amplitudes can also be identified in the individual geometries. The peaks in the sound pressure level occur at the same frequency for all four Reynolds numbers simulated. However, the position of these peaks in the frequency spectrum are not the same for each geometry. For example, in the *compact* geometry clear peaks in the amplitude below 1000 Hz are visible at 270 Hz, 550 Hz and 820 Hz for all

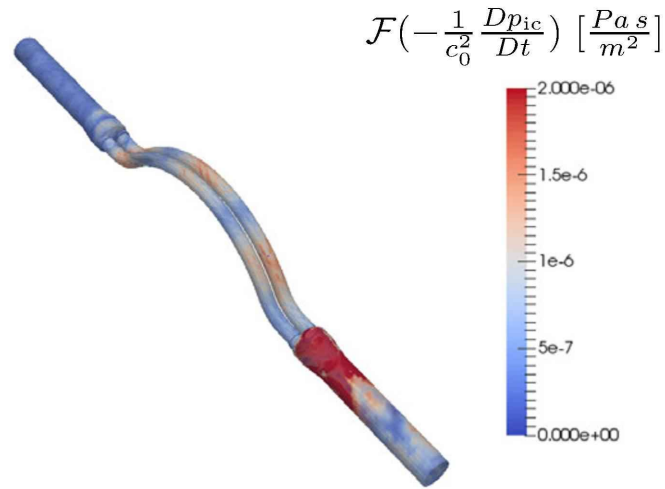


Figure 4.8: The acoustic source at the inlet and bends is about ten times smaller than the acoustic source at the outlet in the *compact* device.

Reynolds numbers are marked in figure 4.9 with dashed lines. In the *high* geometry peaks are present at 145 Hz, 390 Hz and 585 Hz. While in the *low* geometry, peaks are visible at 215 Hz, 430 Hz and 645 Hz. The pattern continues above 1000 Hz for the whole simulated range. Less prominent peaks in the amplitudes are also noticeable across the frequency domain, between the other major peaks. These mostly occur at the same frequencies for all Reynolds numbers, but also differ from device to device.

In some instances the amplitude of a certain peak is higher for a lower Reynolds number than for a higher Reynolds number. For example, in the *compact* geometry all the sound pressure levels plots increase clearly in amplitude for increasing Reynolds numbers. However, in the *high* and *low* geometries, although in general the amplitude increases with Reynolds number, certain frequency peaks show a different behaviour. This can be observed in figure 4.9 when observing the plots for Reynolds numbers 1.4 and 1.8 million.

## 4 Simulation Results

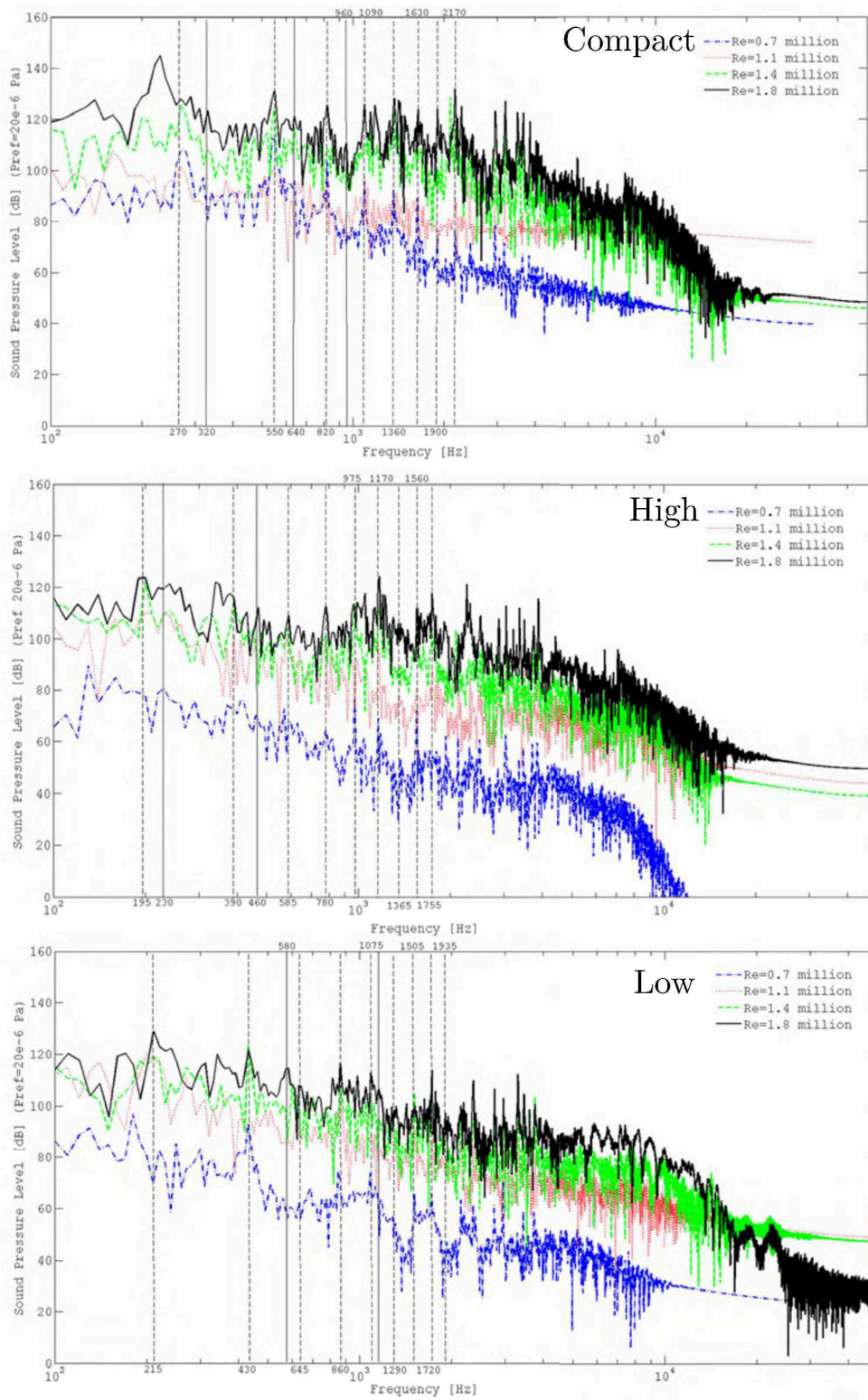


Figure 4.9: Sound pressure level at monitoring point X1 for four different Reynolds number in the three device geometries.

In the *high* geometry, the peaks in amplitude at frequencies 450 Hz, 480 Hz, 850 Hz and 1750 Hz, for example of few, are larger for a Reynolds number of 1.4 million than those for 1.8 million. In the *low* geometry the amplitude of the peaks at 180 Hz, 260 Hz, 430 Hz and 770 Hz are also higher for a Reynolds number of 1.4 million than for 1.8 million. This is an interesting behaviour, since the acoustic source shows a similar behaviour over the frequency. This topic will be further discussed in chapter 6.

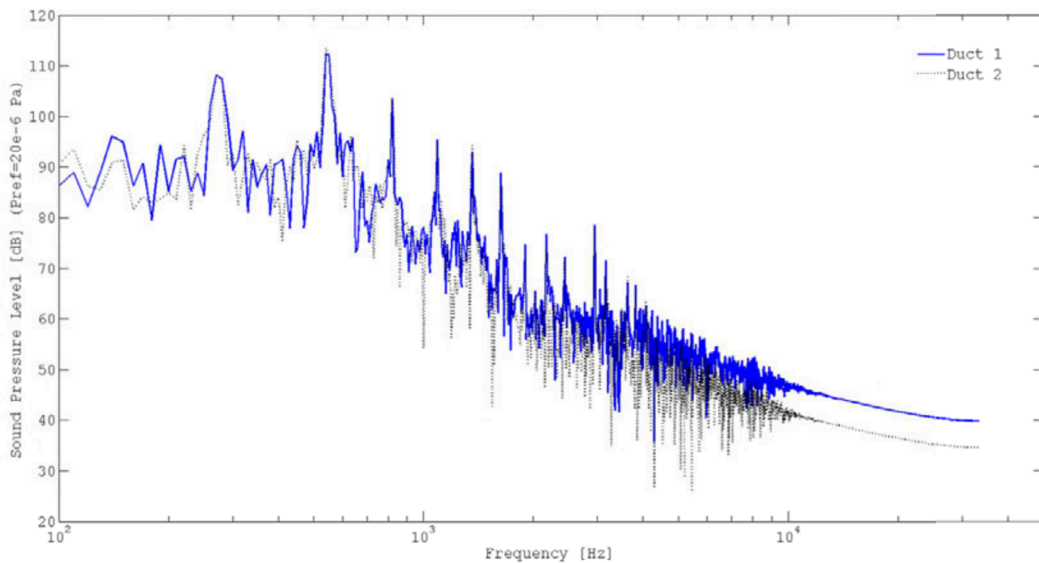


Figure 4.10: Comparison of the sound pressure level on the inlet sensor monitoring point X1 between measuring tubes in the *compact* device at Reynolds number 0.7 million.

The acoustic pressure is also compared between the two measuring ducts. In figure 4.10 the sound pressure level is plotted for the inlet sensor monitoring point X1 on both ducts in the *compact* device. The sound pressure level is seen to be almost exactly the same in both channels. Any differences seen may be attributed to asymmetrical eddies and source terms, or perhaps asymmetry in the CFD or acoustic mesh.

Differences can, however, be distinguished in the sound pressure level along the length of the smaller ducts. Figure 4.11 plots the sound pressure level in one of the channels of the *compact* device at the inlet sensor X1,

## 4 Simulation Results

driver position X3 and outlet sensor X2 monitoring points.

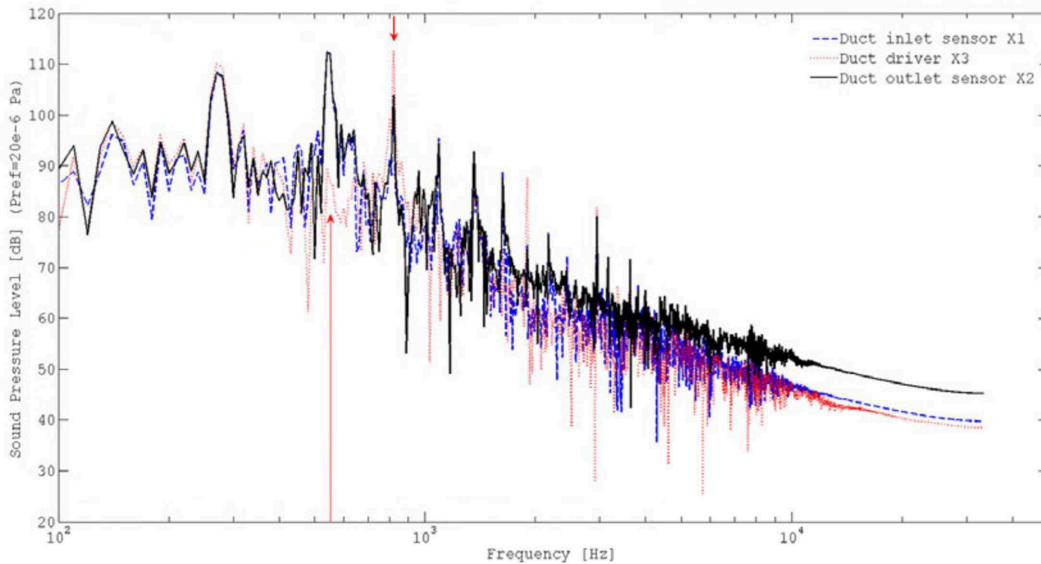


Figure 4.11: The sound pressure level on the inlet sensor, driver position and outlet sensor along one measuring tube of a *compact* device.

At a frequency of 550 Hz the sound pressure level at the driver position X3 is much smaller than the sound pressure level seen at the two sensor positions X1 and X2. At the frequency 820 Hz, the driver position X3 sees a larger sound pressure level than the two sensor points. This can be explained by looking at the volume solution in the post processing software Paraview in the frequency domain. In figure 4.12, for example, the acoustic pressure in the *compact* geometry at 550 Hz is pictured. For this frequency, peaks in the amplitude are very present at the sensor inlet and outlet monitoring points but diminished at the driver position. This can be attributed to the positions of the main acoustic pressures at this frequency, which are large at the inlet and outlet positions but close to zero at the center of the pipe. Thus, although the sound pressure levels tends to be identical in both measuring tubes, the distribution of the sound pressure along the length of the tubes is more complex depending on the frequency studied. This needs to be considered when studying

monitoring point results of the sound pressure level.

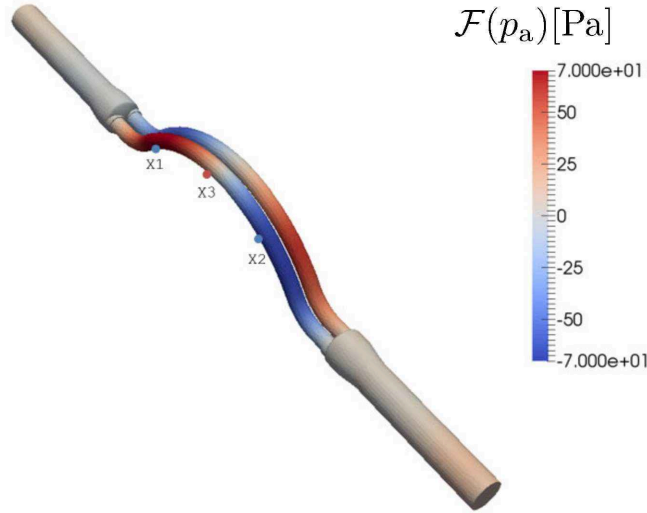


Figure 4.12: Volume representation of the acoustic pressure at 550 Hz in the *compact* geometry for a Reynolds number of 0.7 million.

These acoustic pressures are coupled directly to the mechanics of the system through (2.35) for a complete vibroacoustic analysis. In this way, the mechanical displacements caused by the acoustic pressures in the device may be separated from the hydrodynamic influences and explicitly quantified. The displacements at the sensor positions X1 and X2, and the driver position X3 may be analysed. Plots of the total mechanical displacement at the measuring point X1 in all geometries are shown in figure 4.13. Similar to the graphs of the sound pressure levels at the inlet monitoring point in figure 4.9, peaks may be identified at the same frequencies in each geometry. The peaks once again occur at the same frequencies for all flow rates, but are different from device to device. Furthermore, larger displacements may also be identified for lower Reynolds numbers as in the sound pressure level results and at the same frequencies. For example in the *high* device at 450 Hz, 480 Hz, 850 Hz and 1750 Hz, and in the *low* device at 180 Hz, 260 Hz, 430 Hz and 770 Hz.

## 4 Simulation Results

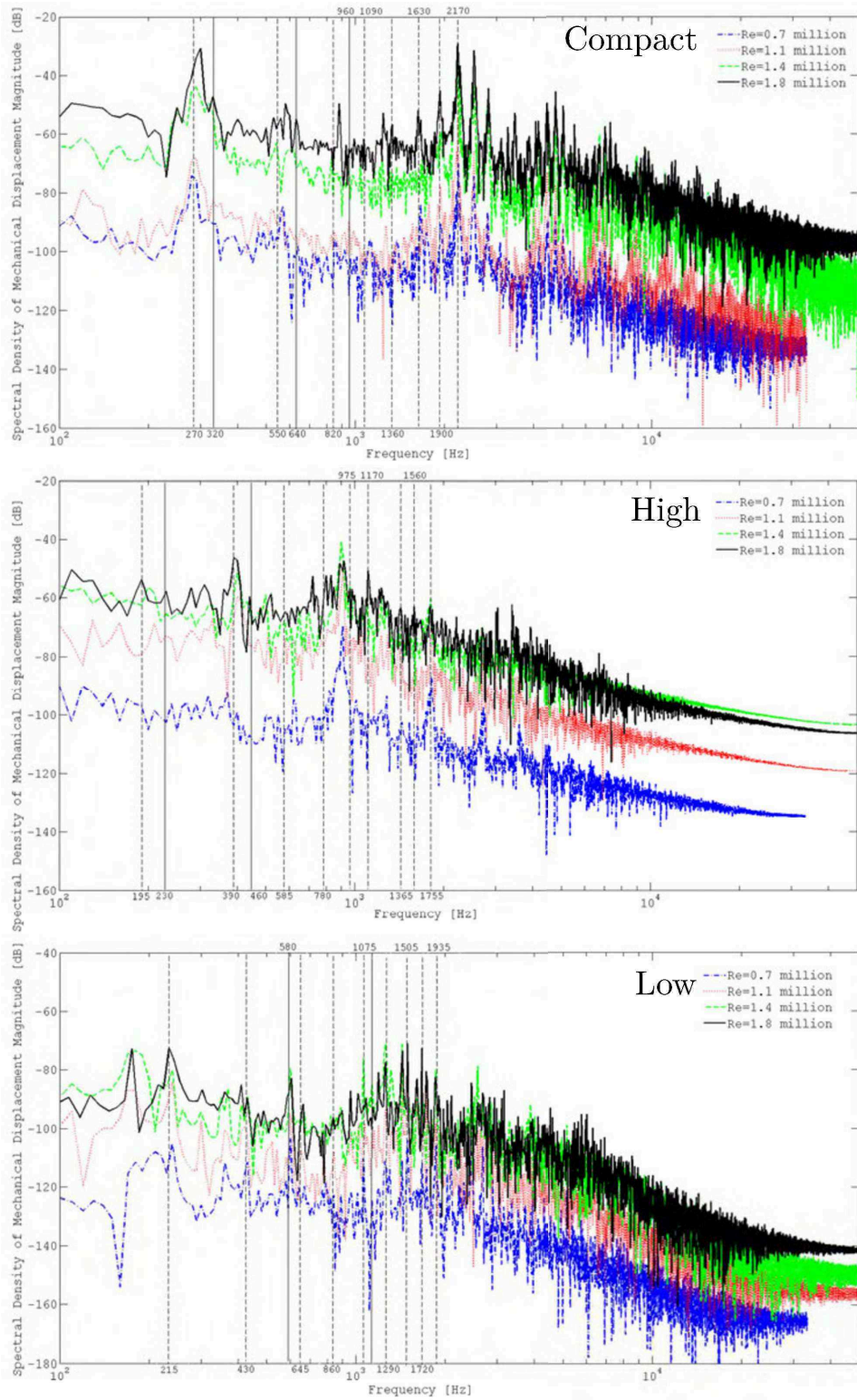


Figure 4.13: Total mechanical displacement at the sensor inlet for all devices at four Reynolds numbers relative to  $12.5 \times 10^6$  m.



Similarly, the volumetric results may be pictured using Paraview, such as in figure 4.14, showing the same frequency of 550 Hz as in figure 4.12. The same shape of the sound pressure levels can be identified in the mechanical system. The mechanical displacement may be broken down into its x, y and z components. The most influential to the measurement quality here is the x component, since it is the vibration direction perpendicular to the flow and allows the most movement due to the device design. The sound pressure level along the length of the duct thus has a direct effect of the mechanical displacement on the ducts due to the acoustics in the system. The total displacement magnitudes, for example in the *compact* device, range from a few nanometers at a Reynolds number of 0.7 million to a maximum of approximately  $4\ \mu\text{m}$  at a Reynolds number of 1.8 million.

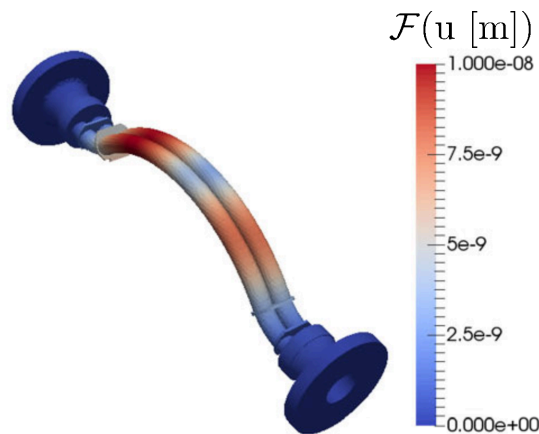


Figure 4.14: Total mechanical displacement of the *compact* device at 550 Hz and Reynolds number 1.8 million.

Although the sound pressure level is seen to be similar in the three devices, the amplitude of the mechanical displacement differs over the frequency range. This can be linked firstly to the sound source amplitude and secondly to the mechanical differences of the duct systems, which can also be frequency dependent. For example, the different mechanical damping or the quality factor,  $Q$ , of each device. The quality factor describes how under damped a resonator system is, and also characterizes

its bandwidth relative to the center frequency. A higher quality factor indicates a lower rate energy loss relative to the energy stored in the resonator and thus the frequency is less damped. It is defined as

$$Q = \frac{2\pi W}{-\dot{W}T}, \quad (4.1)$$

with  $W$  being the energy at the start of a vibration period and  $\dot{W}$  the loss of energy during the period. The values  $W$  and  $\dot{W}$  can be defined using the total energy per vibration  $W_0$  and the damping  $\zeta$  as

$$W = W_0 e^{-2\zeta t} \quad (4.2)$$

and

$$\dot{W} = -2\zeta W. \quad (4.3)$$

Substituting these relations into definition (4.1) for the quality factor, and using the logarithmic decrement  $\delta$  of the amplitude over time due to the damping  $\delta = -2\zeta t = \ln \frac{x}{x_0}$ , results in a quality factor of

$$Q = -\frac{\pi f t}{\ln \frac{x}{x_0}}. \quad (4.4)$$

The quality factor was measured for the three device constructions using an acceleration sensor and FFT analyser. In order to achieve the most accurate results by avoiding any additional damping of the system, the devices are placed on rubber prisms. The devices are excited using a small hammer on the carrier tube and the time that is required for the resonance frequencies to fall to a specific value is measured. The results are recorded in figure 4.15.

The *compact* device shows a high quality factor at its drive frequency of 550 Hz and then the value decreases in both frequency directions abruptly. The *high* device shows a similar behaviour, but also has a high quality factor at approximately double the drive frequency 560 Hz, and then again at 720 Hz. The *low* device also has a high quality factor at its drive frequency of 350 Hz, but then also has many peak values with large quality

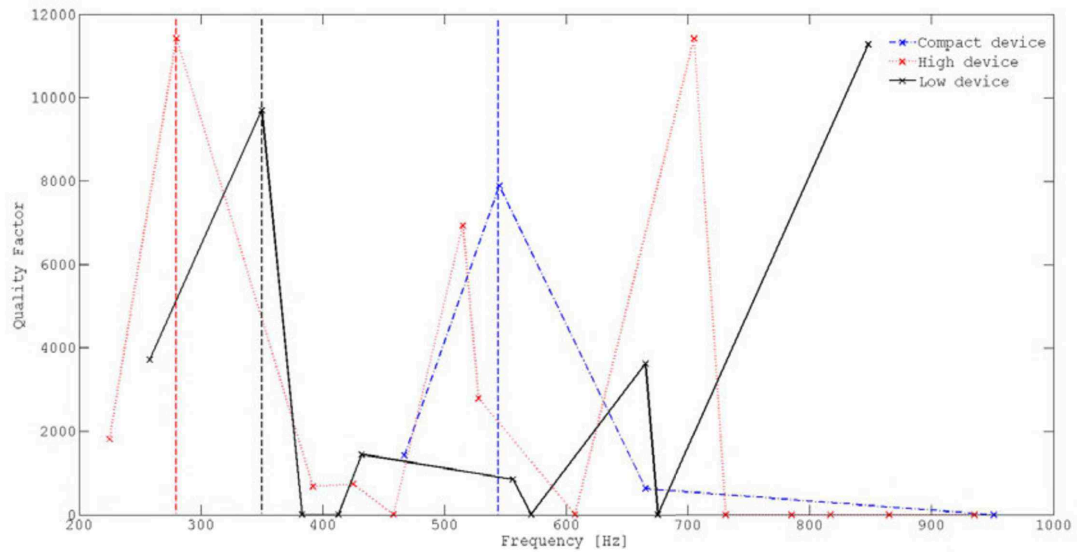


Figure 4.15: Quality factor of the three devices in the frequency range 0 Hz to 1000 Hz with marked drive frequencies.

factors, especially at high frequencies. Where the quality factor is high, the mechanics of the device may be easily influenced by a disturbance in the same frequency range. This behaviour can be optimised through mechanical design using the shape of the measuring tubes, and the amount of coupling elements between them. Usually, dual-channel mass flow meters are designed such that the quality factor is always high at the drive frequency.

Differences in the mechanical displacements at the sensors can also depend on the position of the monitoring points, or sensor positions, on the device. If the monitoring point is placed closer to a peak sound pressure zone the resulting mechanical displacement at this point will be larger. The difference between devices in this case is however not large, since the sensor position is normally chosen such that it is exposed to the largest Coriolis force, and is usually relatively equal when comparing lengths of the ducts. Here it is important to remember that all pipes are made of the same stainless steel material and are of the same wall thickness and diameter.

The mechanical displacement caused by the acoustic pressures has to

be seen relative to the driven vibration of the dual channel measurement devices. Usually all devices are driven such that a displacement of  $12.5 \mu\text{m}$  is achieved at the sensor positions as listed in table 3.2. The high device, with its long tubes, can be driven at twice this displacement. To see the relation between the displacements, the vibroacoustic simulations were run again with an applied harmonic function at the driver positions as described in chapter 3. This imitates the drive frequency of the device. It is confusing to look at the total displacement in this case, since it is unclear which displacements to compare. The main vibration displacement according to the applied function occurs in the direction perpendicular to the flow axis, in this case the x-axis. The same displacement plots as in figure 4.13 are created, now only in the x-direction and with the vibration overlay, see figure 4.16.

Now the drive frequencies are very prominent in the plots, and have been marked with a solid vertical line. The second harmonic of the drive frequencies are also very prominent. Peaks in the amplitude, at the same frequencies as in figure 4.13, can be identified here as well however at a much smaller relative amplitude to the drive frequency. These frequencies have again been marked with dashed vertical lines. In some cases these disturbances are seen in all Reynolds number plots, but mostly they only become noticeable at the larger Reynolds numbers. Additionally, the multiple frequencies of the drive frequency have been marked in this figure using arrows up to 1000 Hz. It is at and around these marked frequencies, as well as at and near the drive frequency, that disturbances may enter the signal processing through the band filter of the device.

Before these results are fully interpreted, they need to be verified for accuracy. This is achieved firstly through numerical verification simulations and finally by measurements on a gas calibration rig.

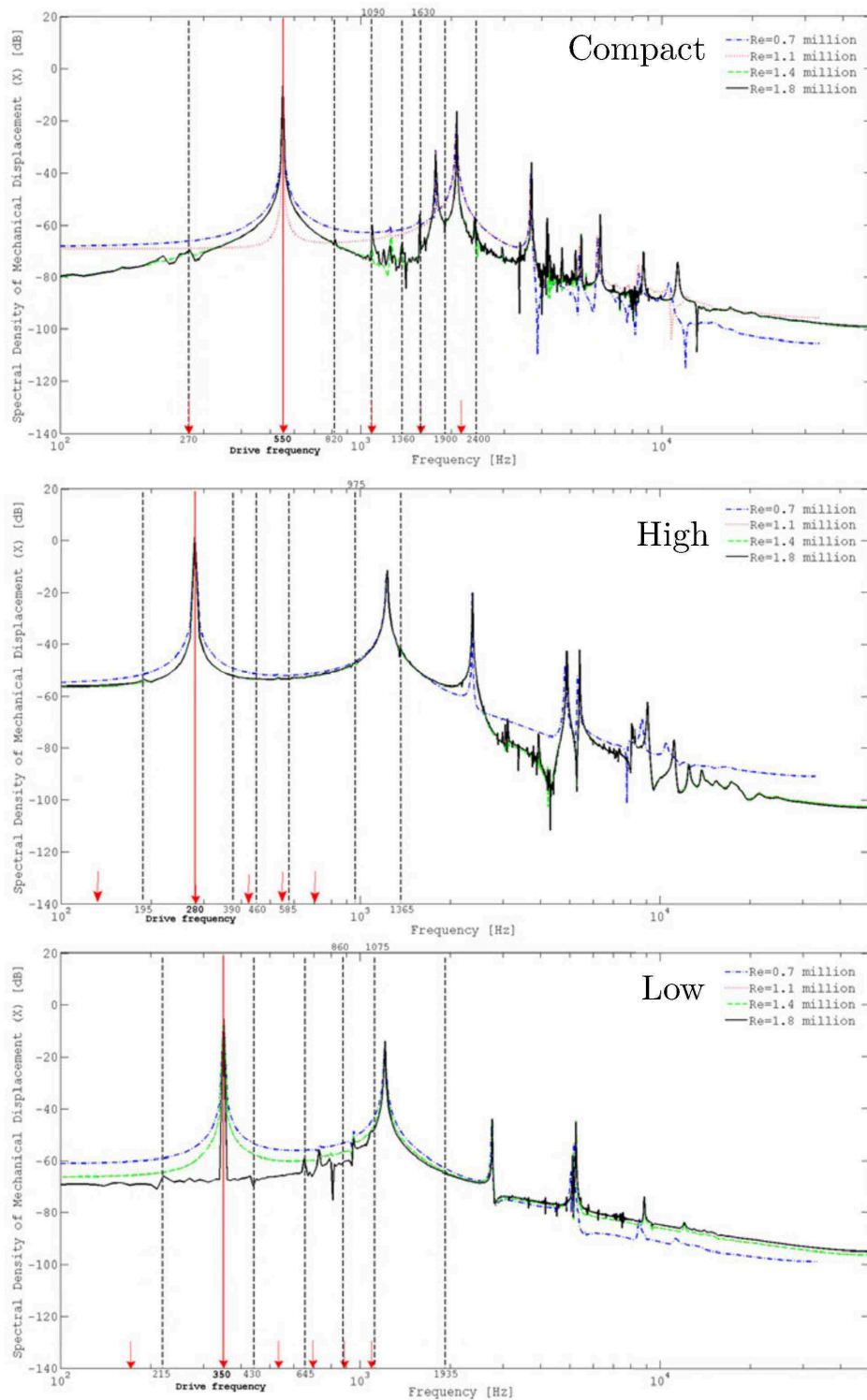


Figure 4.16: Mechanical displacement in the x axis (perpendicular to flow) at the sensor inlet for all devices at four Reynolds numbers with overlaid vibration at the respective drive frequencies.

# CHAPTER 5

---

## Verification of Simulation Results

---

The simulation results are verified using two approaches: first through numerical consistency where the validity of the simulation method and models is tested, and secondly by carrying out measurements on a gas calibration rig. In this way, errors due to insufficiently defined models may be precluded and the legitimacy of the acoustic pressure magnitudes and frequencies established.

### 5.1 Numerical Verifications

The numerical model introduced in chapter 3 is varied in numerous ways, including adaptations to the mesh, boundary conditions and turbulence models. If discrepancies appear between the results, the differences need to be justifiable or else the results are not conclusive. The numerical model is thus evaluated individually for the following different configurations: a 30% finer CFD and acoustic mesh, a hexagonal CFD mesh,

a large eddy simulation model, a pressure inlet definition, asymmetrical geometrical models, various acoustic global functions and acoustic absorbing boundary conditions. Additionally the perfectly matched layer condition was validated on a straight pipe model. All verifications are carried out on the *compact* design at a Reynolds number of 0.7 million. In most cases the numerical model could be easily validated, for example when applying 30% finer mesh or a large eddy turbulence model. A comparison of the acoustic pressure results at the monitoring point X1 for these two cases in comparison to the original model is shown in figure 5.1.

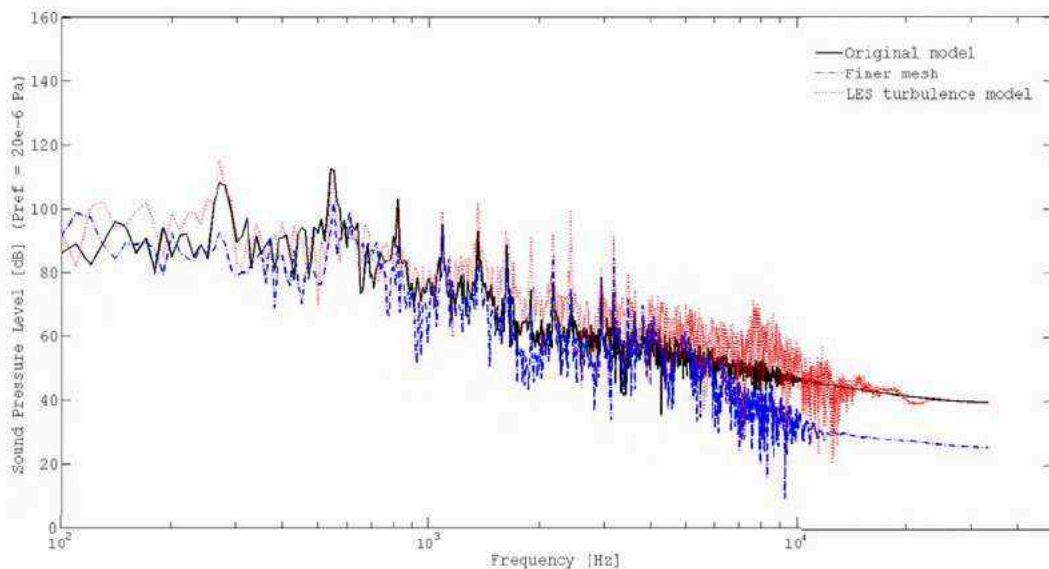


Figure 5.1: Comparison of the SPL at the sensor inlet X1 in the original simulation with two models of a finer mesh and applied LES turbulence model.

The magnitude of the pressure results obtained remains similar and the behaviour in the frequency domain is analogous to the original model for both cases. The large eddy simulation, as expected, does not resolve many of the smaller peaks in the pressure amplitude as observed in the detached eddy simulation results. The finer mesh produces equally good results as the original model. Some of the peaks in the amplitude are

## 5 Verification of Simulation Results

smaller than with the initial mesh, but still occur at the same frequency. To save calculation time, and since the results are very similar, the coarser mesh will be retained.

The use of a hexahedral CFD mesh produced similar results to the original model with polyhedral elements, however the time to reach convergence was greatly increased. This is the main advantage of a polyhedral CFD mesh, even though the interpolation becomes more complex. Due to the large amount of required simulations with the three geometries and four flow rates, a polyhedral mesh is retained. The verification model applying a pressure inlet, alternative to the velocity inlet, did produce slightly altered results. This can be attributed to the difficult initialization of the pressure value at the inlet. The pressure drop in the device is estimated with approximately 10% error, and the final defined pressure at the inlet was subsequently too large. This explains the difference in magnitude when comparing the results to the original model, shown in figure 5.2.

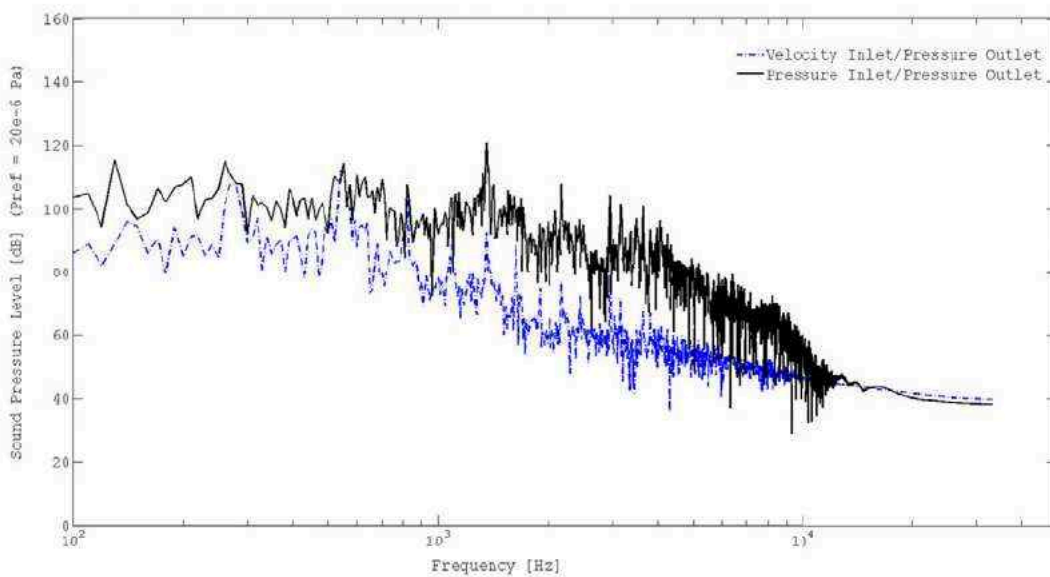


Figure 5.2: Comparison of the SPL at measuring point X1 with application of different inlet boundary conditions.

The behaviour across the frequency domain is however comparable be



tween all cases, considering that the frequency content of the turbulence varies with the flow rate. The main peaks in the amplitude may still be distinguished.

Models with built-in asymmetries on the measuring ducts were simulated in preparation for the measurements on the calibration rig. Not all dual-channel mass flow meters can be assumed to be exactly equal in weight distribution and geometrical form, which is especially true for the ducts due to their complex production process. The effect of these discrepancies or asymmetries on the CFD and vibroacoustic simulations was quantified such that the magnitude of possible result divergences between the simulations and measurements on the calibration rig may be clarified. The tolerances in the weight difference between the ducts is equal to 5 g. Models with asymmetries did not show an influence on the simulation results as long as the values were within the specified tolerances given to the suppliers.

The acoustic global function as discussed in section 3.2 is applied to the acoustic source term for the first time steps of the acoustic simulation and ensures that no acoustic shock is initialized in the system. Originally defined as  $1 - \cos^2(0.5\pi/15e - 6t)$ , it was altered in size and impact time for the same acoustic simulation. No differences between the results could be found, showing that this initialization is not of great importance to the acoustic simulation. A comparison of the sound pressure level in the simulation cases can be found in figure 5.3.

Absorbing acoustic boundary conditions generally result in increased reflection at the inlet and outlet boundaries compared to perfectly matched layer boundaries. This resulted in higher peaks in the acoustic pressure values. This was expected since these absorbing boundary conditions are only non-reflective in one direction, parallel to the flow. The PML boundary condition was further tested on a straight, simple pipe with a center noise source. Through this simple simulation, the reflection or absorption at the inlet and outlet boundaries could be observed over time and the function of the PML could be verified in the implemented software CFS++. It could be observed that the perfectly matched layers adequately damp the outgoing acoustic waves, with no reflections at the boundaries. Their objective is thus verified for this simulation case.

## 5 Verification of Simulation Results

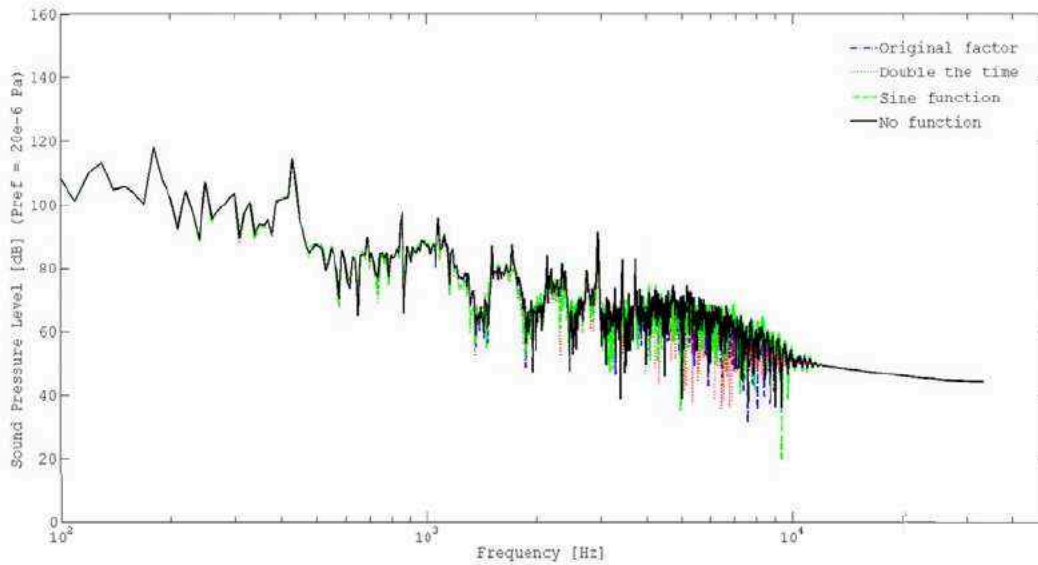


Figure 5.3: Comparison of the SPL at the measuring point X1 when applying various global factors in the acoustic pressure initialization.

The various adaptations to the initial numerical model resulted in no discrepancies in the results, which could not be suitably explained. The boundary conditions and mesh of both CFD and acoustic models are numerically verified and the numerical model is primarily deemed suitable in describing the dual-channel mass flow devices, on condition that the following measurement results also concede.

### 5.2 Measurements

Three prototypes of the geometries *compact*, *high* and *low* were constructed and assessed on a gas calibration rig. The conditions were kept as close to the numerical environment as possible, the fluid used being air at 10 bar and 20°C. The four Reynolds numbers were similarly established with flow rates between 2000 kg/h and 5000 kg/h, corresponding to Reynolds numbers of 0.7 million and 1.8 million respectively. The calibration rig includes three master devices which are used as the cali

bration reference depending on the mass flow through the rig. Only one master is used per measurement. For larger mass flows there are turbine meters and for smaller mass flows there is a piston meter. A layout of the rig can be seen in figure 5.4, where the three masters are installed parallel to one another.

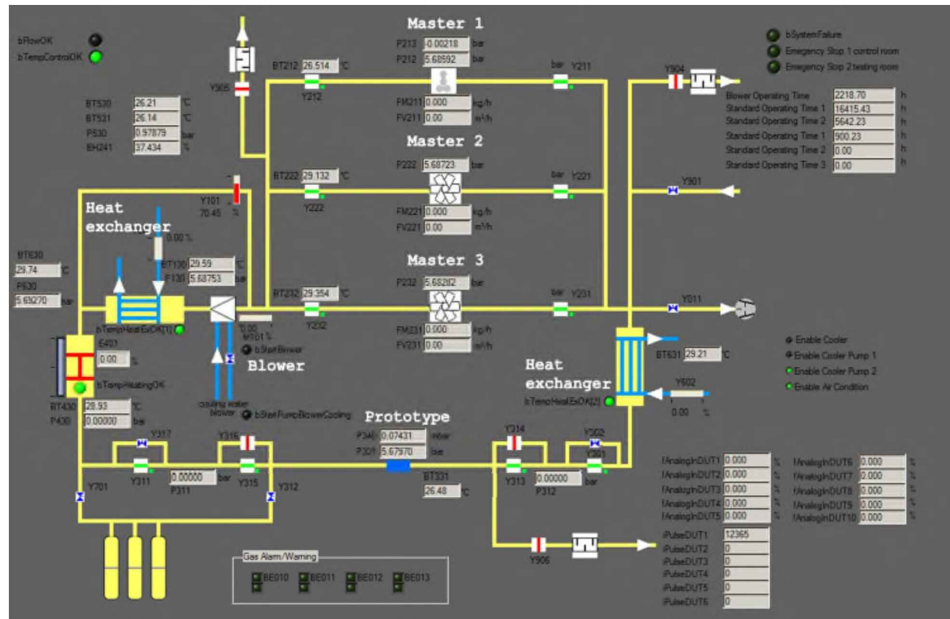


Figure 5.4: A visualization of the gas calibration rig used in the verification measurements.

The prototype being tested is installed in the fourth parallel line at the position of the blue rectangle representation in the figure. The mass flow is regulated by a blower and valve. The fluid passes through a heater and two heat exchangers in the rig, once before the measurement device and once after. This controls the temperature of the gas within a defined tolerance. Air can be measured up to 10 bar and 100°C on the rig. If the measurement requires pressures above 6 bar, a compressor is used to compress the air up to a maximum of 10 bar. The required flow rate, temperature, repeat counts and the respective tolerances are specified in the software window shown in figure 5.5.

The pressure, temperature and flow rate are measured at many points

## 5 Verification of Simulation Results

The screenshot shows the 'Measure' configuration window with the following settings:

- Flow Control Mode:** Mass flow [kg/h]
- Flow Rate:** 5500.00 m<sup>3</sup>/h / 5500.00 kg/h
- Temperature:** 25.00 °C
- Flow Tolerance:** 1.00 %
- Temperature Tolerance:** 5.00 °C
- Measurement Time:** 60 s
- Flow Stability:** 10 s
- Temperature Stability:** 1 s

Standard Density	1.29286	kg/m <sup>3</sup>	Gas Density	1.2929	kg/m <sup>3</sup>
Process Expansion factor Ref.	0.99808		Compressibility Standard	0.9981	
Process Viscosity Ref.	1.87094E-5	Ns/m <sup>2</sup>	Dyn Viscosity	18.70943E-6	Ns/m <sup>2</sup>
Process heat capacity Ref.	1019.98761	J/kg K	Heat Capacity	1019.9876	J/kg K
Standard Expansion factor	0.99953		Standard Compressibility	0.9995	
Process Expansion factor DUT	0.99820		Compressibility Mut	0.9982	
<input checked="" type="checkbox"/> Use Gas Engine			Mass Cor Factor	1.00568	

Additional settings:  Auto Update, Repeat Count: 10,  Use "Continue" after pre. run. Buttons: Start, Continue, Cancel.

Figure 5.5: The flow rate, temperature, tolerance and repetition specifications of the measurements made with the gas calibration rig.

throughout the rig and the values can be monitored. These values are used to control the specified flow rate and temperature values required for the measurement. The Gas Engine software automatically updates the gas density and viscosity values. Furthermore, the measurement time, flow stability waiting time and the amount of measurement repeats may be specified. For the purpose of the current measurements, a measurement time of 60s, a flow stability time of 10s and a repeat count of ten measurements per flow rate was specified. The flow rate tolerance and temperature tolerance values were set to 1% and 5% of the measured value respectively. The prototypes were singly installed between two butterfly valves, as seen in figure 5.6. These were both fully open during the measurement phase but could be closed individually before and after the measurement to control the zero point setting, the stability, of the device. The electronics of the prototypes were connected to the calibration rig such that the number of pulses recorded during the

measurement phase may be read out. This value is used to calculate the flow rate value which is then compared to the flow rate value of the appropriate master. The flow rate, temperature and oscillation frequency as seen by the device electronics was also recorded using a measurement laptop and the appropriate software.



Figure 5.6: A dual-channel mass flow meter installed in the calibration rig and the laser vibrometer measurement points at the sensor positions for the displacement measurement.

In order to study different effects on the measurement values, measurements were also repeated on the devices with differing parameters. The parameters include oscillation amplitude at the sensor, weight at the sensor and weight at the driver. For this purpose either the amplitude was adjusted in the electronics using the software Remote Control, or extra magnetic weights were added to the sensors and driver of the device. The three devices were measured without the housing component such that the measurement ducts of the device were exposed. This was done so that parallel to the gas measurement, two laser vibrometers could be used to measure the velocity at the two sensor points of the device. Removing this housing may shift the resonance frequencies of the body of the device, but not that of the measurement frequency. The Polytec laser OFV302 from Endress+Hauser Flowtec is an older version of the Polytec OFV534 laser borrowed from the Vienna University of Technology. However since a Nikon 50 mm lens has been attached to the laser the quality of the laser point reached was comparable. The older laser vibrometer controller OFV2600 was only able to measure the velocity of a point, so for a direct comparison the new laser vibrometer controller

## 5 Verification of Simulation Results

---

OFV5000 was also set to measure the velocity of the sensor point. The laser OFV302 was positioned at the outlet sensor and the laser OFV534 at the inlet sensor and measurements were made simultaneously at different flow rates. The values were also read out simultaneously using a wavesurfer 424 200MHz Oscilloscope. The time division was set at 10ms/div and the voltage output to 1V/div for the older vibrometer and 500mV/div for the newer vibrometer. This was due to the fact that the vibrometer settings differed: the older vibrometer has the scaling of 25 mm/s/V and the newer vibrometer of 50 mm/s/V. These settings allowed a measurement over approximately 0.1s which, relative to the measurement frequency, recorded between 20 and 50 sensor oscillations. The older and newer laser vibrometers have a resolution of 0.5 mm/s and 0.15 mm/s respectively. The maximum measured velocities of the sensors were between 25 mm/s and 100 mm/s. This provides satisfactory measurement accuracy. The reflection of the points measured by the laser was increased using silver adhesive strips. The lasers were set upon a movable wagon which was positioned at the optimal distance from the measurement point according to device, and then locked in place. The height and orientation of the lasers was adjusted using metal blocks such that the lasers themselves were stable and did not move during the measurements.

The measurement results against the master devices produce two useful values. The first is the absolute deviation against the master and the second is the scattering of the measurements results at a single mass flow. Ideally the deviation and scattering should both be as small as possible. The cause for a large deviation from the master device is not necessarily the same cause for large scattering in the measurement values. The deviation of the three prototypes to the master device is plotted in figure 5.7. Results are shown for flow rates between 1000 kg/h and 5500 kg/h with ten measurements taken at each flow rate. The *compact* and *high* devices show a similar performance, with less deviation from the master device as the *low* device. All devices show a degree of scattering in the ten measurement points at all flow rates.

A case where the scattering amplitude of the device could be reduced was to set a larger vibration amplitude at the driver. For example in

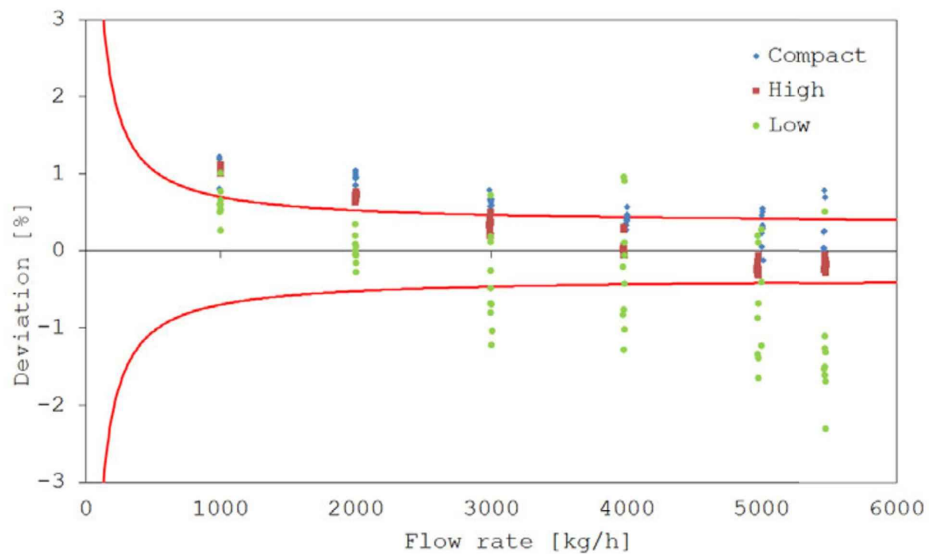
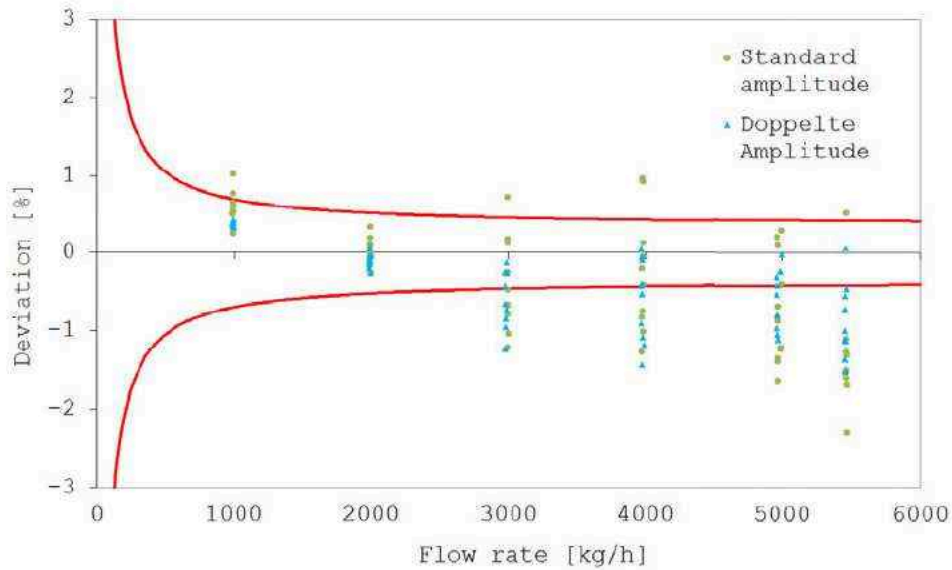


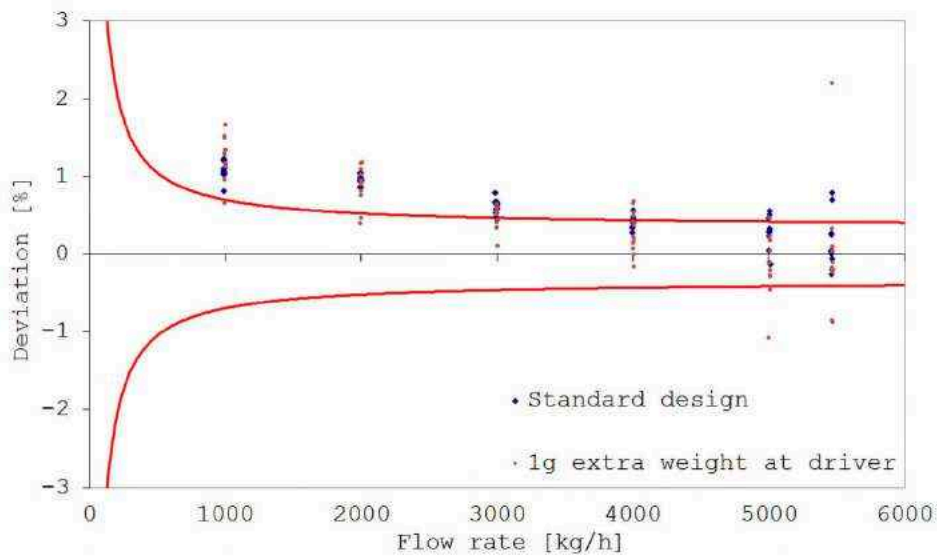
Figure 5.7: Deviation of the dual-channel mass flow meters from the master devices with ten measurements per mass flow rate.

figure 5.8 a) the results are compared in the *low* device for the original vibration amplitude of  $12.5\ \mu\text{m}$  and double this amplitude. This occurs since the vibration amplitude is now larger relative to the disturbance frequencies which have not increased, and the signal is less disturbed which enters the electronic signal processing circuit. In a further investigation, extra weight was added to the sensor position or driver position on one duct, such that the ducts became more unsymmetrical. This had the result of worsening the scattering effect over all flow rates. Figure 5.8 b) shows a comparison of the original prototype with a device containing an intended asymmetry of 1 g at the sensor. Since for these cases no change was seen in the simulations, it is assumed that the general measurement performance and balance of the device is worsened by asymmetrical conditions, which is known, but does not necessarily affect the acoustic behavior in a prominent way. At the most, it causes an increase in the difference in behavior of the two ducts, such that the acoustics has more or less effect on one duct than the other. However, this effect should be smaller compared to the effect of the decrease in the balance of the device.

## 5 Verification of Simulation Results



- (a) An improvement in the reproducibility was achieved by increasing the vibration amplitude of the device, pictured here for the *low* device.



- (b) The reproducibility was worsened when the weight balance between the ducts was affected, pictured here for the *compact* device.

Figure 5.8: The scattering amplitude of a device could be altered by changing the vibration magnitude or bringing asymmetries to the device.



Since the overall deviation from the master devices is not the primary optimization goal, a plot comparing the scattering amplitude over the flow rate has been produced in figure 5.9. Overall, the scattering of the measurement point is worst in the *low* device at all flow rates. The *compact* and *high* devices are similar in scattering magnitude but differ in the behaviour with flow rate. The scattering in the *compact* device, increases with flow rate, especially at higher flows. The *high* device experiences more scattering at a flow rate of 4000 kg/h, corresponding to a Reynolds number of 1.4 million, than at a flow rate of 5000 kg/h, corresponding to a Reynolds number of 1.8 million. The same behaviour can also be seen in the *low* device. A similar behaviour has already been observed in the acoustic pressure levels and mechanical displacements from the simulation results, where at certain frequencies both magnitudes were higher at a Reynolds number of 1.4 million than for 1.8 million.

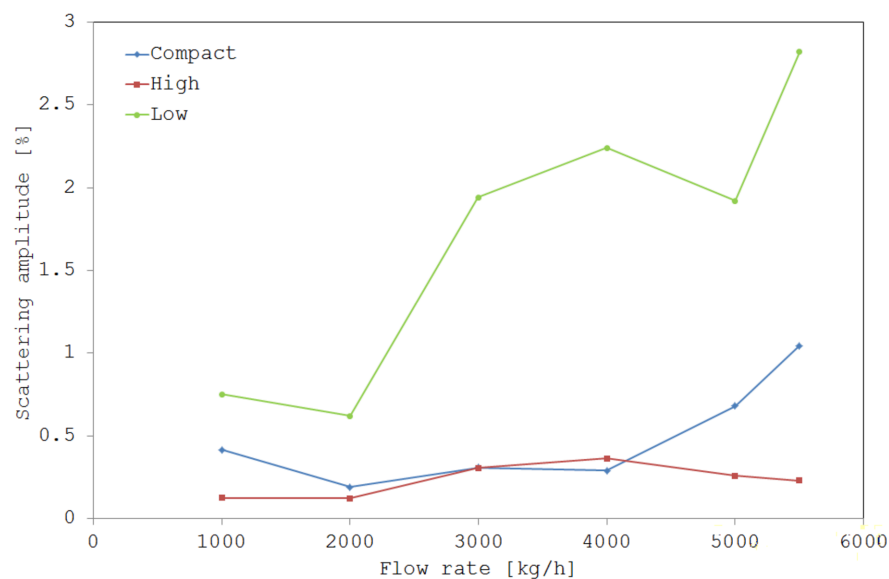


Figure 5.9: The amplitude of the measurement scattering in the three prototypes at all flow rates.

Additional results are obtained from the laser vibrometer measurements. The laser vibrometers capture the displacement of the device at the sensor points. Since they are placed to the side of the calibration rig

with the laser focused on the duct, they capture mainly the x component of the displacement when related to the coordinate system of the simulation results. This relates to movement perpendicular to the flow direction and duct arch. The x-component also has the most influence on the accuracy of the devices since it is the main vibration direction of the ducts at the drive frequency as shown in figure 1.2. When applying a Fourier transform to the difference between the signals, dominant frequencies present at the sensor positions can be identified in similar plots to those in figure 4.13. As can be observed in the plots of the measurements in figure 5.10, there are definitely disturbing frequencies acting on these sensor points, apart from the drive frequency. Additionally, these disturbances are observed to be at the same frequency positions as those identified in the numerical simulations. A further confirmation of the simulations can be found in the plots of the *high* and *low* devices at Reynolds numbers 1.4 and 1.8 million. As also identified in the plots from figure 4.13, there are frequencies where the sound level pressure is higher for a lower Reynolds number. Now in figure 5.10, larger displacements at the sensors can also be distinguished for a lower Reynolds number, for the same devices. For example at 450 Hz, 480 Hz, 850 Hz and 1750 Hz for the *high* device and 180 Hz, 260 Hz, 430 Hz and 770 Hz for the *low* device.

Although the position of the peaks match well, as shown by the dashed vertical lines, the amplitude can be expected to differ slightly from the simulations, since there are distinct differences between the prototype and numerical model. For example, in the numerical model the mechanical geometry was defined as one part and defined using the properties of one single material. In the prototypes, the couplers, tubes and flow diverters are all made from slightly different steels and are brought in contact through rolled, soldered and welded joints. Furthermore, differences arise due to the calibration rig itself, which contains numerous additional acoustic sources such as the blower, diameter changes and bends. In the numerical model this system was simplified to a never-ending straight duct. Additionally, the laser vibrometer measures axially in a fixed position, which means that it lies on slightly altered points of the tube as it vibrates. The monitoring points X, however, are fixed to the tube.

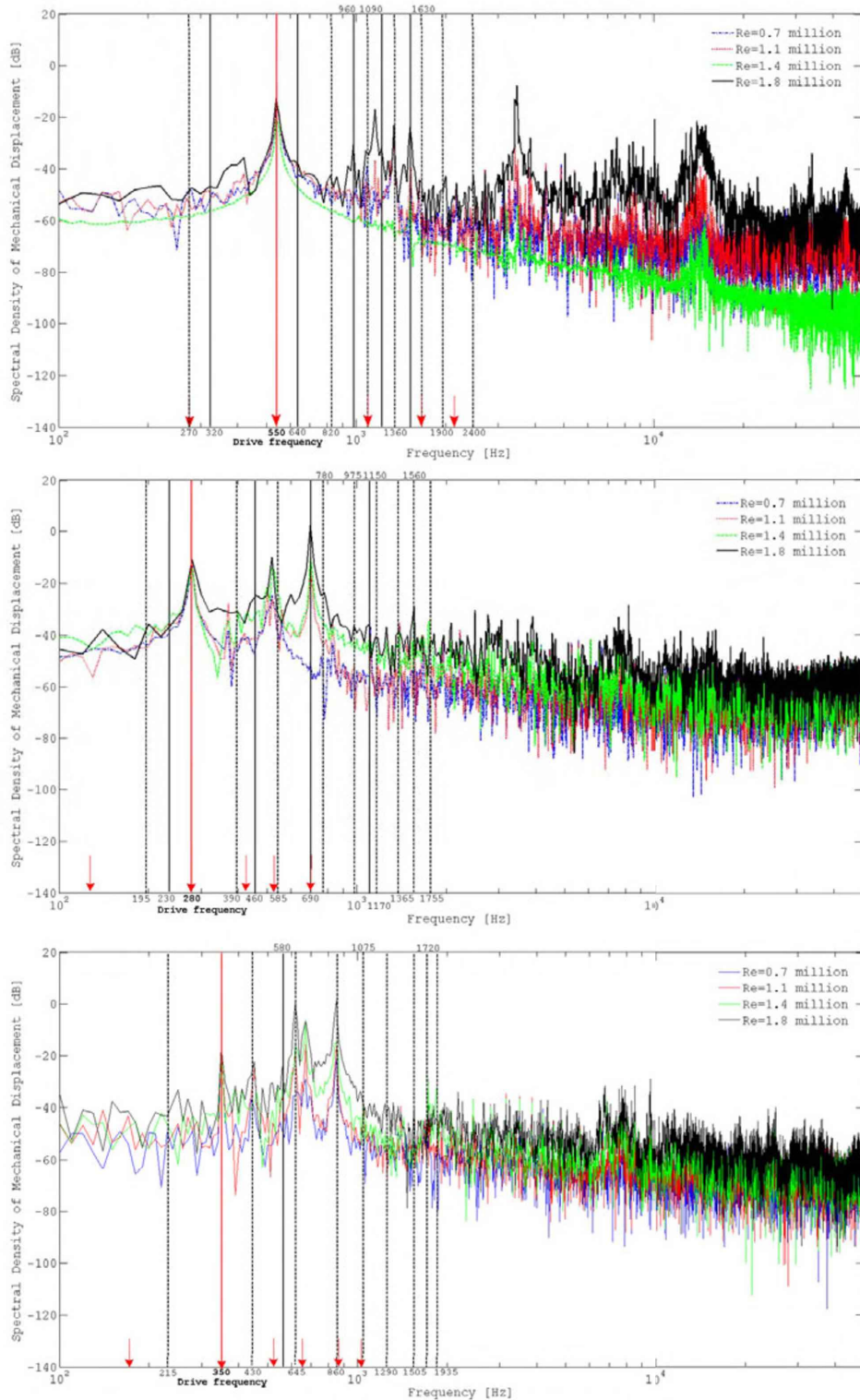


Figure 5.10: Total mechanical displacement as measured at the sensors with a laser vibrometer for all devices at four Reynolds numbers relative to the norm sensor displacement of  $12.5 \mu\text{m}$ .

## 5 Verification of Simulation Results

---

Overall, the measurements produced results which may be related to those obtained in the numerical models. The same disturbance frequencies were observed, with similar scales and the behaviour over Reynolds number could be confirmed. The peaks in the amplitudes occurred at the same frequencies and the behaviour with increasing or decreasing Reynolds number could be confirmed. Due to the good correlation of the measurement results with the simulation results, and due to the numerical verification, the simulations models are deemed to produce results close to reality and may thus be interpreted to produce an evaluation of the acoustic phenomena in dual-channel mass flow devices.

# CHAPTER 6

---

## Interpretation of device performance

---

With the positive verification of the numerical model, the simulation and measurement results can be further analyzed. In this section the link between the scattering of the measurement values and the flow induced sound will be drawn, reasons for the non linear behavior will be considered through closer study of the acoustic sound source region and the simplification of the problem using one dimensional acoustics will be introduced. In conclusion, the general influential factors of the device design will be discussed.

### 6.1 Clarification of measurement error

In each investigated geometry, peaks in the acoustic and resulting mechanical displacement amplitude spectra occur at frequencies across the simulated range. These peaks coincide with yet unexplained disturbance frequencies identified in the device geometries during the measurement on

the calibration rig. When these peaks in the acoustic and mechanical amplitude are large, and furthermore very close to the drive frequency of the respective measurement device, an increase in the scattering of the measurement values during experiments at each flow rate is observed. This means that when ten measurements are taken at the same flow rate, results are scattered between  $\pm 1\%$ , or even  $\pm 3\%$ , of the actual value. The increased scattering of measurement values leads to a decrease in the repeatability accuracy of the device. An increase in scattering is also observed when the peaks in the acoustic and mechanical displacement amplitudes occur close to multiples of the drive frequency, or for example half the drive frequency. The reason lies in the filter band-stop of the electronics, centered on the drive frequency as pictured in chapter 1 in figure 1.3. With this filter, disturbance frequencies up to 50 Hz away may be seen by the electronics, and these disturbances may also be folded up or down if they lie near multiples of the drive frequency. The closer these disturbances to the drive frequency, or to factors thereof, the more the disturbance will affect the measurement. Generally this means that if we reduce or eliminate the disturbing frequencies, the repeatability of the measurement values should improve. In order to achieve this, it must first be understood where these peaks originate from, and their interdependencies on other factors.

The position of the peaks in the acoustic and mechanical displacement amplitude spectrum is geometry dependent, since the location of the peaks differ for all three devices. However, for each device the peaks remain at approximately the same frequency for all Reynolds numbers, with increases or decreases in the amplitude according to the mass flow. The sound pressure level plots obtained in both the smaller channels were the same, but varied along their lengths, as seen in figures 4.10 and 4.11. The behaviour was observed in the numerical results and also confirmed by the measurements on the gas calibration rig. This leads to the presumption that there are excited acoustic resonances in the system, which are dependent on the duct geometry according to the following equation

$$f_n = \frac{nc_0}{2L}, \quad (6.1)$$

where  $f_n$  is the  $n$ th acoustic resonance of a duct length  $L$  containing a fluid where the speed of sound is  $c_0$ . These acoustic resonances are excited on a broad scale, where the main acoustic source must be acting as broadband sound source directly at the outlet flow diverter of the device as shown for all devices in figure 4.6. Applying (6.1) to the smaller parallel ducts, the amplitude peaks are seen to correlate with the acoustic resonances which could occur between the two flow splitter geometries as listed in table 6.1. Slight differences occur due to the neglect of the duct end correction factors, as well as due to the 10 Hz resolution of the simulated frequencies.

Table 6.1: Comparison of the drive frequency, first simulated amplitude peak and first calculated acoustic resonance frequency in the three geometries.

	<i>Compact</i>	<i>High</i>	<i>Low</i>
Drive Frequency [Hz]	550	280	350
First amplitude peak [Hz]	270	195	215
First acoustic resonance [Hz]	280	210	230

Additional acoustic resonances must also be present in the results, such as between the bends in the ducts or between other diameter changes. These acoustic resonances are however much less prominent than the resonances between the inlet and outlet flow diverters. The acoustic resonances between the flow diverters can be identified when observing the acoustic pressures in the entire device in the frequency domain. To illustrate this, the first two acoustic resonances for all the geometries, relating to the first disturbance frequencies, have been pictured in figure 6.1 for the highest flow rate using Paraview. The modal shapes of the resonances are the same, but occur at different frequencies for each device according to equation 6.1.

This is the first time that a link between the repeatability errors in

dual-channel mass flow measurement devices and the flow induced sound in the duct system could be established. The errors experienced in the field thus do not arise from direct acoustic pressure forces at the inlet, outlet or in the bends which could be interpreted from the initial fluid

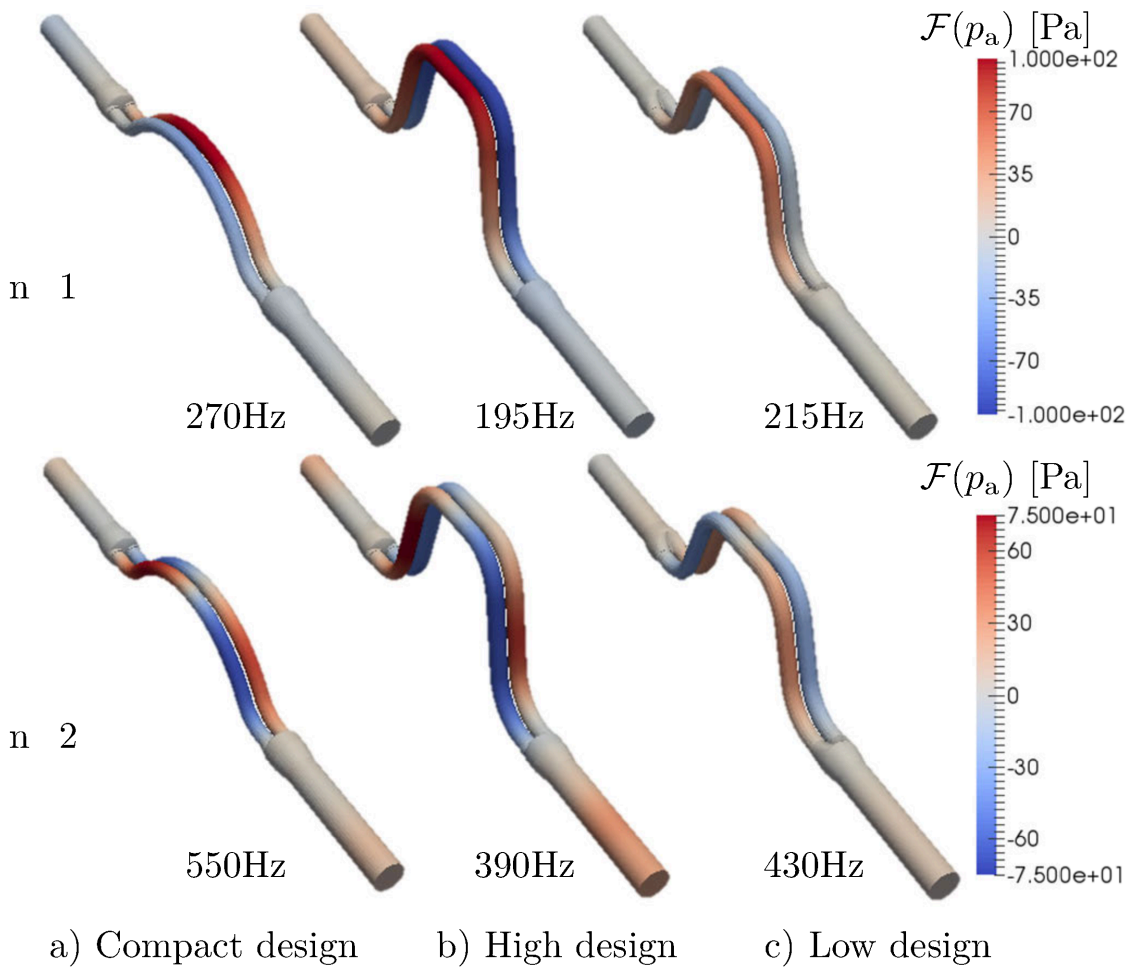


Figure 6.1: Modal view of the first and second acoustic resonances in the fluid between the flow diverters in all three geometries.

dynamic results pictured in figures 4.3 and 4.4. The fluid dynamic results showed large vorticity in all three of these areas. The errors also do not arise due to propagating circumferential or pulsating modes in the system as discussed in the introductory chapter. The repeatability



accuracy is affected by the excited acoustic resonances due to a broadband noise source acting at the outlet flow diverter, shown in figure 4.8 in comparison to the other source areas. The acoustic pressures themselves are perhaps of too small scale, at least compared to the arising hydrodynamic pressures in such a system, to have any direct influence on the stiff, stainless steel duct wall. However through their excitation of the acoustic resonances in each specific geometry, the disturbances acting on the duct wall become large enough that measurement errors can occur. The size of the final measurement error depends once again, amongst other factors, on the proximity of the disturbance frequencies to the drive frequency of the respective devices.

The acoustic pressures, now amplified through resonance, interact with the duct walls and cause mechanical displacement of the channel according to the modal shape of the acoustic resonance. These displacements can have a maximum at the center of the pipe, near the ends, or at many points along its length. See figure 6.2 for an example of the mechanical displacements caused by the first two modes in the compact geometry for the highest flow rate.

Here the link between the acoustics and the mechanical displacement of the duct can be drawn. For the dual channel device system, the displacements on the duct walls is what is measured by the inductive sensors with an accuracy in the nanometer range. Thus it is important to understand how much deflection comes from the measurement effect, and how much from disturbances. Thanks to the hybrid numerical method, the pure acoustic pressures present in the system have been resolved, and thus the displacements resulting from the directly coupled acoustic mechanical model indicate the pure disturbance displacements resulting from the acoustic pressures. The mechanical system itself is a stiff stainless steel tube structure, which is one of the stiffest geometries. It is thus significant that the acoustic pressure can cause any deflection at all, that would result in erroneous measurements. This capability to produce deflections at the sensors starting at 30 nm for the lowest flow rates up to 5  $\mu\text{m}$  for the highest flow rate is again attributed to the acoustic resonance behaviour. The maximum disturbance in comparison to the normal drive frequency displacement at the inlet sensor for the three geometry types

is listed in table 6.2 for all flow rates. As explained in the beginning of the chapter, when the displacements occur at a frequency which can pass through the band filter, they will be used in the algorithm to calculate the flow value, and cause large scattering in the flow measurement values.

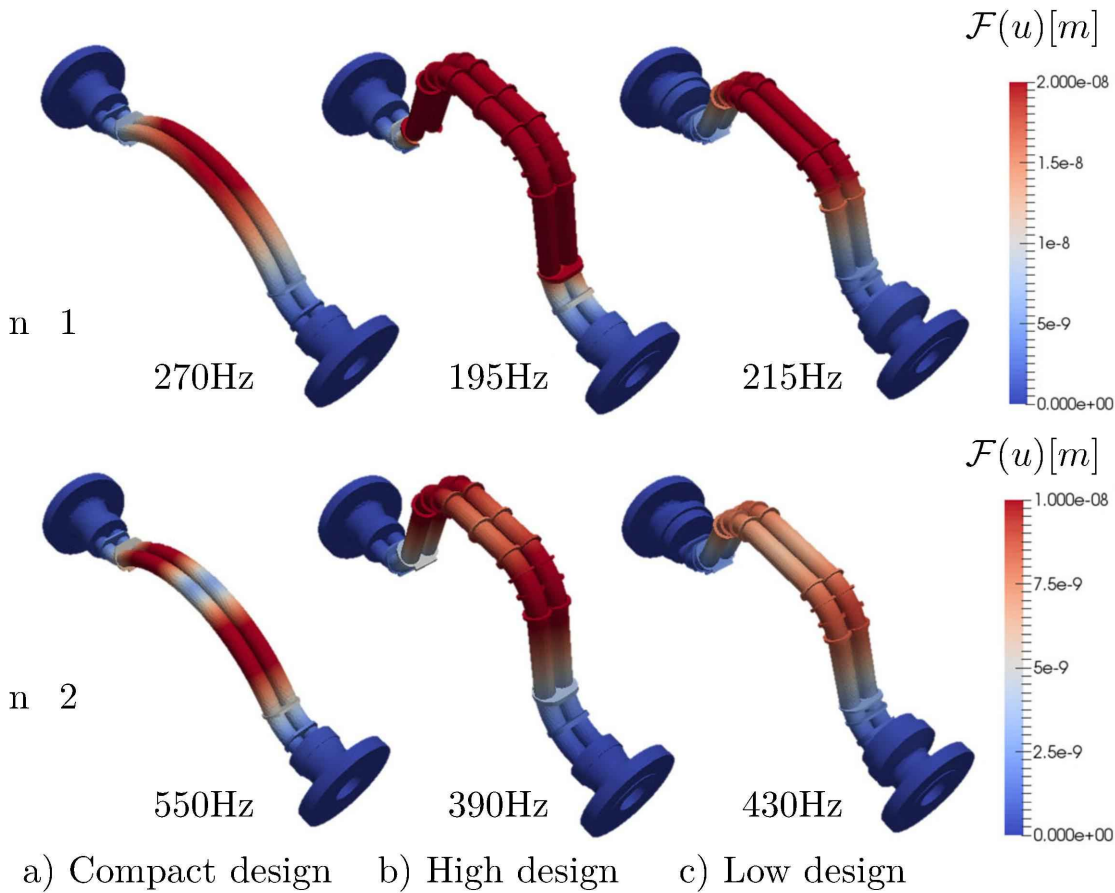


Figure 6.2: Modal view of the influence of the first and second acoustic resonances on the mechanical system in all three geometries.

In table 6.2 these disturbances are shown to be nearly 50% of the normal drive frequency displacement which occurs at the sensor position. The disturbance in the *high* device is possibly lower due to the high arch form, since the sound source and resonance were otherwise comparable to the other two designs.

At this point it is important to again note other factors affecting the influence of the acoustic resonances on the dual-channel mass flow devices,

Table 6.2: Maximum magnitude of displacement at the sensor position in the three geometries at the highest flow rate.

	<i>Compact</i>	<i>High</i>	<i>Low</i>
Driving displacement [ $\mu\text{m}$ ]	12.5	25	12.5
Maximum disturbance displacement [ $\mu\text{m}$ ]	4.37	0.96	5.2

the first of which is the damping of the mechanical structure. Dual-channel mass flow devices are not actively damped, but as a result of the large effort put into their effective and accurate design, a mechanical damping results from the structure itself which tends to be lower around the drive frequency than for other frequencies. A good example of this can be seen in the *compact* design when studying figure 4.15. The quality factor is very high at the drive frequency of 550 Hz, and reduces rapidly at all other lower and higher frequencies. It can thus be expected, that disturbance frequencies acting on the structure that are not directly at the drive mode are to a large extent damped and will not have a large influence on the mechanical displacement of the duct. The *high* device also shows this behaviour at its drive frequency of 280 Hz, but also at two additional frequencies, around 500 Hz and 700 Hz. The possibility that disturbance frequencies in these areas will affect the flow measurement is thus increased. The *low* device displays the worst design in this consideration, with a total of five frequencies with high quality factors in the considered range. Thus almost all disturbance frequencies will cause larger mechanical displacements of the duct. A further factor affecting the influence of the acoustic resonances on the flow devices is the amplitude of the vibration at the drive frequency. It has been observed in the measurements that dual channel devices have an improved repeatability accuracy when the amplitude of the driving vibrations are larger. This is understood to be an effect of the relative displacements. When the vibration amplitude is doubled, the disturbance frequencies are not, and thus their relative effect on the mass flow measurement is decreased. This is pictured in figure 4.16 in chapter 4, where the vibration frequencies are seen to overlap the disturbances frequencies such that they can no longer

be identified until very high flow rates.

An intriguing, and somewhat deceptive, behavior is that the amplitude peaks in the acoustic pressure and mechanical displacement do not always increase with increasing flow rate. In some cases, the peaks in the amplitudes are larger at a lower Reynolds number than the same peak for a higher Reynolds number. For example, this can be seen in the behaviour of the *high* device in the sound pressure level figure 4.9 at frequencies around 450 Hz, 480 Hz and 850 Hz, among others, for the two largest flow rates. The peaks in the amplitude for a Reynolds number of 1.4 million are higher than the peaks at Reynolds number of 1.8 million. The first logical understanding of the acoustic and mechanical displacement amplitudes would be that, as the flow rate increases so does the turbulence in the duct and thus the amplitude of the broadband sound source. This stronger acoustic source thus results in a higher excitation of the acoustic resonances and the peaks in the amplitudes should increase for all cases. This is in fact true for most of the frequencies when looking at the plot, but definitely not for all amplitude peaks. The behaviour is repeated in the mechanical displacement results, seen in figure 4.13 at the same frequencies. An initial verification for this behaviour seen in the numerical results is that the scattering amplitude measured on the gas calibration rigs also showed nonlinear behaviour across flow rate. This was picture in figure 5.9 where for the *high* and *low* devices a larger scattering amplitude results at a mass flow of 4000 kg/h than for 5000 kg/h, respectively Reynolds numbers equal to 1.4 and 1.8 million. This indicates that the outlet turbulence contains a specific acoustic pressure frequency spectrum depending on the Reynolds number, and it is reproducible. In this regard, it is interesting to study the statistical values of the turbulence at the outlet area for different Reynolds numbers.

### 6.2 Statistical values of turbulence

A turbulent flow is by its nature irregular and random, which means a deterministic approach to turbulence is impossible [44]. Turbulence excites a broad spectrum of fluctuations observant in most turbulent

quantities such as the velocity [45]. The turbulence energy spectrum is a method used to display the energy content of the turbulence over wavenumber or frequency. It is defined using a correlation tensor  $R_{ii}(a, t)$  between velocities at two different points separated by a distance [44],

$$R_{ii}(a, t) = \langle u_i(x, t)u_i(x + a, t) \rangle, \quad (6.2)$$

where  $u_i$  is the velocity component with defined spatial direction  $i$ . The Taylor hypothesis states that for fully developed turbulence, the spatial average and the time average are equivalent [46]. Since the turbulent velocity field is assumed to be homogeneous and isotropic the correlation tensor is a function only of the distance between the two points and not on their location. The three dimensional energy spectrum is then

$$E(f) = \frac{1}{2} \mathcal{F}[R_{11}(a, t) + R_{22}(a, t) + R_{33}(a, t)] \quad (6.3)$$

which, by performing the Fourier transform yields

$$E(f) = \frac{1}{2} \sum_{i=1,3} \tilde{u}_i(f) \tilde{u}_i^*(f) \quad (6.4)$$

where  $\tilde{u}_i$  is the Fourier transform of the velocity in the  $i$ th direction and its conjugate is marked with \*. An example of the general form of a turbulence energy spectrum is shown in figure 6.3.

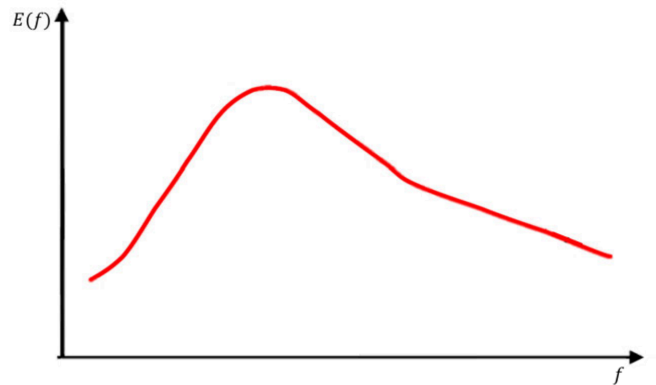


Figure 6.3: Schematics of a turbulence energy spectrum [47]

From figure 6.3 it can be observed that for a particular turbulent flow, the turbulent energy is highest for a certain range of frequencies, and then decreases again. This curve is derived from the correlation of the velocities with one another.

For the case of the multi channel geometries, the main acoustic source is located directly at the outlet side of the flow diverter. It is here that the velocities in all three directions need to be read out at specific points. A balance between the amount of data and the validity of the results needs to be obtained. Points chosen too far downstream shift the frequency spectrum away from the true source nature. Only when points very close to the acoustic source were chosen, interpretable results were achieved. Points in a pattern as pictured below in figure 6.4 were chosen for the analysis. The *high* geometry has been used for this analysis, due to the nonlinear nature of the repeatability accuracies with flow rate.



Figure 6.4: The monitoring points (in red) used to build the turbulence energy spectrum from the velocity vectors in the *high* device.

The three dimensional velocity data was additionally read out for each of these points for every time step in the previous CFD simulations for the four flow rates in the *high* geometry. The data was used to form the turbulence energy spectrum using Matlab. The energy spectrum for the four Reynolds numbers at the outlet sound source area is shown in figure

6.5. The general form of the spectrum shown in figure 6.3 is mirrored here, however there is no specific range of frequencies that contain more or less turbulent energy when comparing the flow rates.

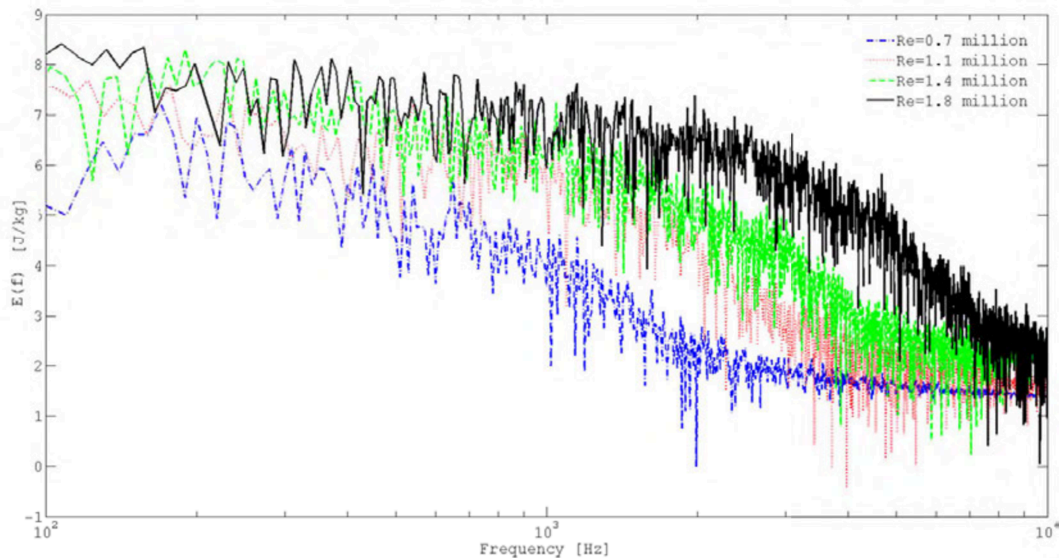


Figure 6.5: Turbulence energy spectrum in the *high* device in the acoustic source region.

However, it is more interesting to study the peaks in the amplitudes at specific frequencies across the range. It is observed that at specific frequencies the magnitude of the energy spectrum is larger at a Reynolds number of 1.4 million than 1.8 million, as in the simulation results. The position of these frequencies correspond to the same frequencies observed in figures 4.9 and 4.13, namely around 450 Hz, 480 Hz and 850 Hz, amongst others.

This provides a link between the increase in scattering of the measurements values at a Reynolds number of 1.4 million in the *high* device, the corresponding peaks in the sound pressure levels in the same geometry which were higher for this Reynolds number of 1.4 million than for a Reynolds number of 1.8 million and the energy spectrum of the turbulence.

A similar behaviour is achieved by plotting the sound power level of

## 6 Interpretation of device performance

the acoustic pressures at an additional monitoring point, as displayed in figure 6.6. This monitoring point is placed at the acoustic source area on the wall of the outlet flow diverter. Once again, the amplitude differences reoccur at the same frequencies as named previously when comparing the Reynolds numbers of 1.4 million and 1.8 million.

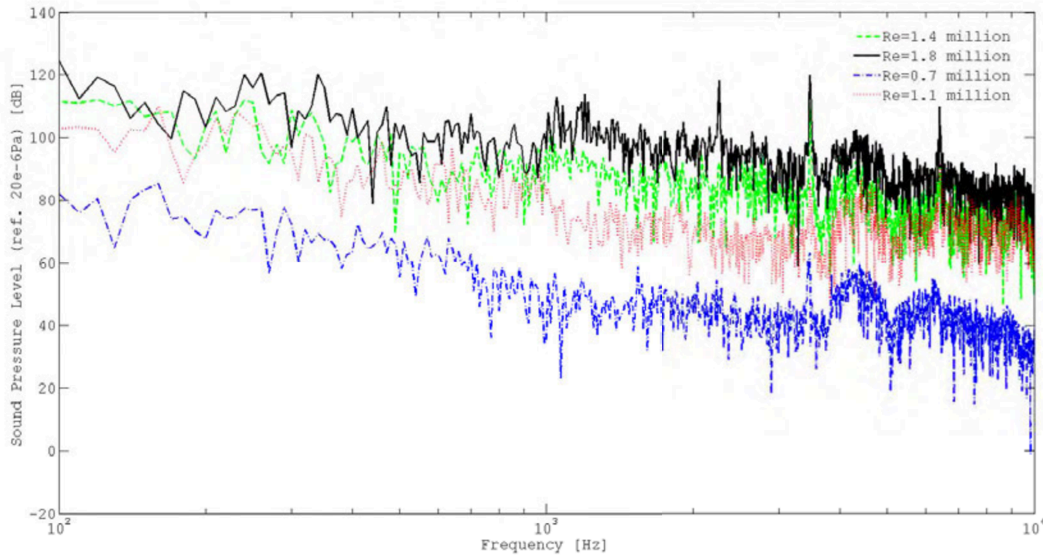


Figure 6.6: Sound pressure level at flow diverter monitoring point on the *high* device for all Reynolds numbers.

The turbulence energy spectrum over the Reynolds number theorizes that the behavior of the acoustic pressure in the smaller pipes is controlled by the behavior of the main acoustic source at the outlet over Reynolds number. At the same frequencies that can be identified in figures 4.9 and 4.13, the energy content of the turbulence is greater. This causes an increase in the acoustic pressure and mechanical displacements at the monitoring points placed on the device sensors. This means the energy content of the turbulence over frequency is Reynolds number dependent and reproducible. This also explains the intriguing behavior of the amplitude peaks, or scattering of the measurement values, which increase at certain Reynolds numbers.

It is important to note that this behaviour is also seen for other Reynolds



number pairs, such as for 1.1 million and 1.4 million, where a nonlinear increase in the scattering of the measurements was not observed. This can be attributed to the location of the relevant disturbances in relation to the drive frequency. A lower Reynolds number may show a larger sound pressure level or energy content at a certain frequency, but if this disturbance is located far away from the critical frequencies then it will not influence the device signal processing and the scattering of the measurement values will not increase. To properly confirm this behaviour further study is required.

### 6.3 Device performance factors

Of the three investigated devices, acoustic resonances were present in all of them. The amplitude of these acoustic resonances were similar for the same resonant mode, and the amplitude of the acoustic sources were comparable for the same Reynolds number. However, all three devices measured with different repeatability accuracies, or scattering magnitudes of the measurement values. There are thus additional factors to consider when evaluating the quality of a device for high speed gas measurement. All these factors need to be considered when finding an improved concept for a device design.

#### **Distance of the acoustic resonance frequencies to the drive frequency**

The acoustic resonances result in a larger disturbance when they lie close to the drive frequency of the measurement devices, because the band stop filter is centered at this frequency. The acoustic resonances also cause a larger disturbance if they are close to multiples of the drive frequency, such as twice or three times, or even half the drive frequency. This point is hard to avoid, since there will almost always be an overlap of some kind in the device, especially since by good design of the system the mechanical and acoustic resonances often lie close together.

### **Symmetry of the resonance mode according to the two sensor positions**

The mass flow rate is measured using the phase difference between the two sensor positions on the smaller ducts, one at the inlet side and one at the outlet side. If the modal form of the acoustic resonance affects both of these sensor positions equally the total effect on the measurement value should be close to zero. Only when the two sensor positions are affected out of phase, or asymmetrically, will an acting disturbance effectively be measured.

### **Amplitude of the sensor vibration**

The amplitude of the sensor vibration relativizes the amplitude of the disturbance. If the drive amplitude of the device is doubled, for example, the disturbances resulting from the flow induced sound still remain the same. Thus the true mass flow rate signal has double the weighting in the following signal processing steps than the disturbance frequencies, and thus the repeatability accuracy improves.

### **Filter bandpass**

The disturbance frequencies are to an extent allowed through to the signal processing by the current bandpass filter. Factors such as the bandpass width and signal processing time affect how many disturbances are included in the flow rate calculation.

### **Amplitude of the source**

The amplitude of the sound source in the three discussed geometries was comparable, however there are geometries which contain larger sound sources for the same mass flow rates. When the sound source amplitude is larger, the total effect on the system also grows respectively.

### **Mechanical damping of the constructive geometry**

The mechanical damping of the dual-channel mass flow meter design assists in damping out disturbance frequencies. An optimal design has a high quality factor around the drive frequency of the device and close to zero at all other frequencies. In the mechanical damping, not all dual-channel mass flow meter designs are equally effective, as observed in chapter 4.

### **Sensitivity of construction to disturbances**

Apart from the mechanical damping of the device, other mechanical design factors also play a role in the influence of the disturbances on the system as a whole. Design factors include the duct thickness, arch height, and connections to the other components which effect the stiffness of the device. Additionally, the stiffness of the sensor holder also affects the influence of disturbances transferred to the actual sensor position.

### **Amount of disturbing resonances**

The main disturbances in the current system were the acoustic resonances between the two flow diverters. Depending on the acoustic impedance of the system components, and additionally on the mechanical damping, more or less disturbance frequencies may build in a dual channel mass flow device. The more disturbance frequencies there are, the larger the possibility that they are in a position which will negatively affect the measurements.

### **Amplitude of the acoustic resonance**

Where the sound source magnitude is the same, the excited acoustic resonances in the system do not necessarily also have to be equal. The acoustic resonances, although primarily excited by this sound source, are also able to build due to the geometrical properties of the devices which affect the acoustic impedance. Different geometries, especially at the

## 6 Interpretation of device performance

---

points of the sound reflection, lead to varying amplitudes of the acoustic resonances.

# CHAPTER 7

---

## Improved design

---

Now that the mechanism behind the repeatability error in the dual channel mass flow devices has been understood, measures may be taken which aim to improve their performance for high flow rates where turbulence, and consequently the flow-induced sound, is large. In this section the various approaches for possible design improvements will be discussed and evaluated. A prototype will be constructed using the best optimization approach and the measurement results of the new dual channel mass flow device design will be presented. Conclusively, an optimization tool has been developed in order to speed up future acoustic analysis of dual channel flow meters.

### 7.1 Methods for design improvement

There are five approaches which could be identified during the result interpretation to improved the dual-channel mass flow meter design:

- Targeted design of the acoustic resonances and drive frequency
- Increased driven vibration amplitude
- Improved filter in the device electronics
- Decreased acoustic source amplitude
- Reduced effect of the acoustic source on the sensors

The aim, when looking for a solution to the acoustically induced in accuracies, is to be able to adapt existing dual channel meter designs such that their measurement error lies within a 0.35% limit. Optimally, this should be done with minimal effort by applying the same improvement to all design types and sizes with as few geometrical adaptations as necessary.

### 7.1.1 Targeted design of the acoustic resonances and drive frequency

The disturbance frequencies resulting from the flow-induced sound are seen to cause errors when they are near the drive frequency or multiples thereof. Dual-channel mass flow meters could thus be adapted such that these acoustic resonances lie at least 100 Hz away from the drive frequency and its multiples. Unfortunately, this requires a high design effort since there are many interdependent geometrical parameters. Dual channel mass flow devices are foremost optimized in their general measurement performance. Parameters include the duct shape and length, the position of the duct couplings, the use of stiffening rings and flow-optimized flow diverters. Once the device has been optimized in this regard, any changes in order to shift the acoustic resonances could be detrimental to the otherwise optimal design. Furthermore, designing the geometry such that the acoustic resonances lie at least 100 Hz away from the drive frequency and its multiples proves to be difficult, since these frequencies naturally lie close to each other, and there are many collision points. This problem is illustrated in figure 7.1 for the *high* design, where many disturbance frequencies are less than 100 Hz away from the critical frequencies for this device. The problem is further amplified when measuring different

mediums, for example air and water. The drive frequency of a device depends on the weights of the narrow channels and can be shifted up to 120 Hz depending on the medium being measured. A targeted frequency design for air will thus not suffice if the device is subsequently used for other fluids.

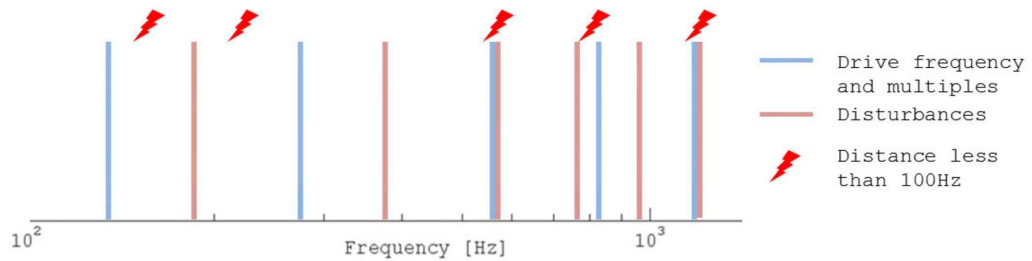


Figure 7.1: Position of the drive frequency with its multiples compared to the disturbance vibration frequencies in the *high* device.

Additionally, the production process of the dual channel devices allows for geometrical tolerances such that the frequencies also have a certain tolerance allowance. This method has overall proved too problematic with all device geometries, and it has been decided not to include this technique in the optimization of the dual-channel mass flow devices.

### 7.1.2 Increase the driven vibration amplitude

The verification measurements showed that an increased vibration amplitude of the ducts at their drive frequency results in an improvement in the repeatability accuracy of the devices. This would indeed be an easy way to improve the device performance, however the improvements seen do not bring the total measurement error below 0.35%. The scattering amplitudes remain too large. A further drawback of this method is the increased cyclic fatigue of the duct constructions. Some dual channel mass flow meters are able to withstand larger vibration amplitudes, such as the *high* device in this study, because of their specific construction. This includes a combination of factors such as the arch height and duct wall thickness. If this method would be implemented, many existing geometries of the mass flow meters would need to be altered. This method has

thus also been dismissed for the device optimizations due to the meager measurement improvement and the large effort required for changes in the current designs. However, designs which can withstand the increased amplitude should take advantage of this improvement and always employ a larger driven vibration amplitude.

### 7.1.3 Improved filter in device electronics

The current filter band-stop of the electronic processing unit allows signals up to 50 Hz away from the drive frequency of the meter to be partially included in the mass flow calculation. Unfortunately, this bandwidth cannot simply be narrowed to within a few Hertz, since the processing speed of the mass flow signal will be greatly reduced. This will affect the dynamic measurement capability of the devices, which is important for accurate measurement with rapidly changing flows, for example in a milk filling station. The dependency of the signal processing speed on the bandwidth was shown in figure 1.4. A reduction of the filter bandwidth from 50 Hz to 12 Hz results in a signal processing time more than three times longer.

A solution to this problem would be to use a dynamic filter, which increases the bandwidth of the filter bandpass when it detects a change in flow rate. This would be an improvement to the current filter, however the initial flow rate change would still be detected quite late and thus the accuracy of the meter would still be decreased due to the narrowing of the bandpass. This may be improved in future, but in this work it has been decided to focus on the sensor design. The aim is to eliminate any disturbance frequencies from the system before they are able to enter the signal processing.

### 7.1.4 Decreasing the acoustic source amplitude

The most forthright approach to improved device performance would be to decrease the amplitude of the acoustic sources. When the sound source is eliminated or at least reduced, then the acoustic resonances will not be strongly excited and the disturbances due to the acoustic



pressures will decrease. These lower disturbance amplitudes would result in an improved repeatability accuracy of the device. Since the strongest acoustic source exists at the outlet flow diverter, it is here where the main improvements should be made. Additionally the smaller sound sources at the inlet flow diverter and at the bends may also be further reduced.

The flow diverter results in an area of flow separation at the outlet which is the principle source of the flow induced sound. In literature recommendations can be found for the reduction of the turbulences in such regions. For example, expansions should be in the form of conical sections with an angle not exceeding fifteen degrees, and sudden area changes and narrow bends which increase the level of turbulence and should be avoided [48]. Bends also result in a higher sound transmission than a straight pipe section of the same diameter and wall thickness due to mode conversion [48]. A solution with an improved flow diverter could be easily substituted into all flow meter designs, without any major changes to the duct shapes or height.

The outlet flow diverter has thus been adapted with the aim of decreasing the turbulence caused by the rejoining of the two flows from the smaller ducts, as well as with the aim to minimize any dipole sources on the separation surfaces. The main changes to the flow diverter are the introduction of a filleted nose starting between the two smaller ducts and

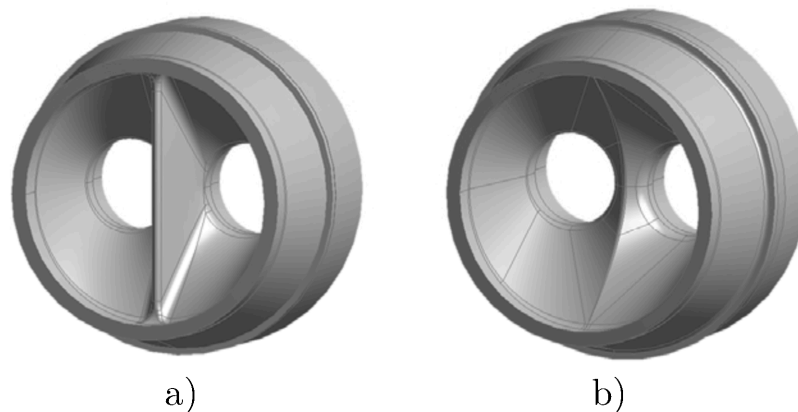


Figure 7.2: Two example flow diverter designs, a) flow diverter 1 and b) flow diverter 2, to reduce the flow induced sound at the outlet.

leading in to the wider duct. The nose allows for a more steady combination of the two flows. Furthermore, the shape of the cavity is amended to achieve an optimal flow field and reduce the dipole sources. Two examples of new flow diverter geometries are shown in figure 7.2. The first flow diverter illustrates a case with a nose between the two narrower ducts, the second flow diverter focuses rather on the curvature of the junction itself. The geometries pictured in figure 7.2, as well as many more geometries of a similar form, were substituted in to the outlet side of the *compact* design and were analyzed using the numerical method described in chapter 3. Unfortunately, none of the designs brought a reduction to the amplitude of the acoustic source at the flow diverter outlet. Figure 7.3 compares the sound pressure level of the original *compact* design to that in the two *compact* geometries containing flow diverters 1 and 2 respectively at the highest Reynolds number. All designs show a similar, or higher, sound pressure level over the whole frequency range at the inlet monitoring point x1.

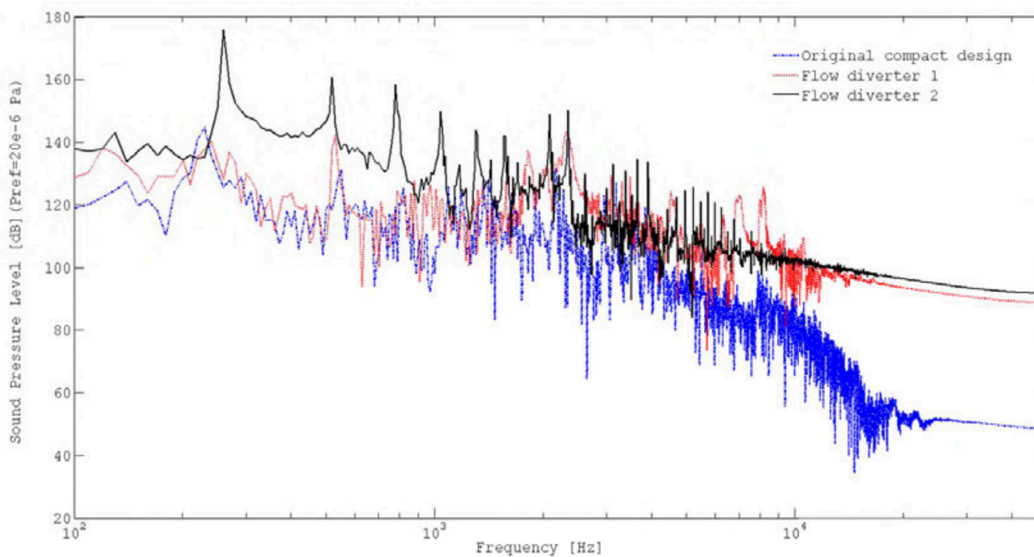


Figure 7.3: Comparison of the sound pressure level at the inlet sensor for the highest Reynolds number in the original *compact* design and designs containing two new flow diverters.

Especially flow diverter two produced very strong acoustic resonances

shown in the large amplitude at 230 Hz and 550 Hz. The first flow diverter produces similar results to the original design. The changes to the flow diverter were not enough to bring improvement to the acoustic source. In order to understand the process a little better, the original *compact* design has been altered in two ways regarding the length of the narrow ducts before the outlet flow diverter. Firstly, the length of the narrow ducts were increased after the last bend in the axial direction such that the flow could reach a less turbulent state before entering the flow diverter. Secondly, the length of the narrow ducts was increased before the last bend, in order to see what influence the bend has on the magnitude of the acoustic source at the outlet. The acoustic source, when observed at the same frequency at the outlet flow diverter in all cases, does change aesthetically. However the magnitude remains the same, as shown in figure 7.4 at the position of the main source.

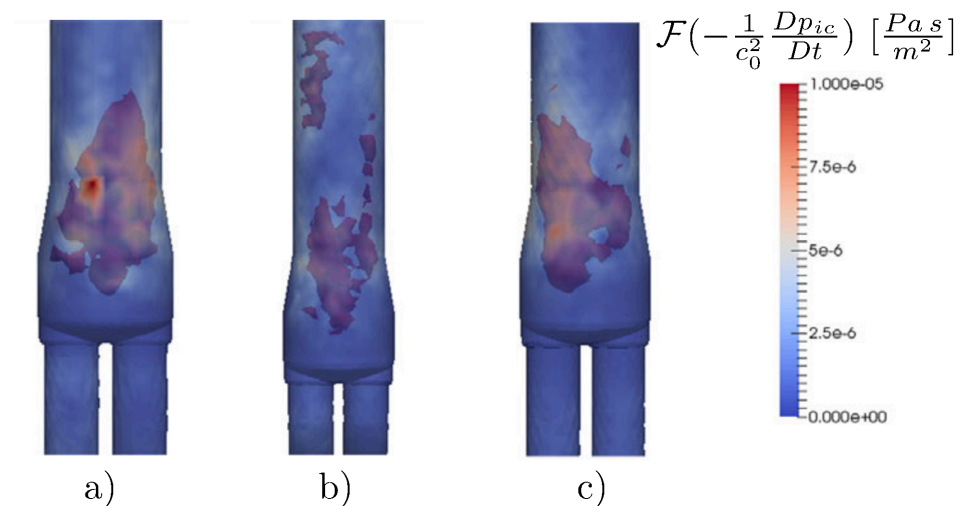


Figure 7.4: Comparison of the acoustic source at the outlet flow diverter for the highest Reynold number for the cases a) original, b) long before bend and c) long after bend.

Thus the geometry before the outlet flow diverter has little influence on the magnitude of the sound source. As expected the sound pressure levels at the acoustic resonances are also of similar magnitude at the inlet sensor shown in figure 7.5. Note that the peaks in the amplitudes occur at different frequencies due to the change in length of the ducts between the

two flow diverters which results in different acoustic resonances according to equation 6.1. The two altered geometries are pictured in the same sound level pressure plot in figure 7.5.

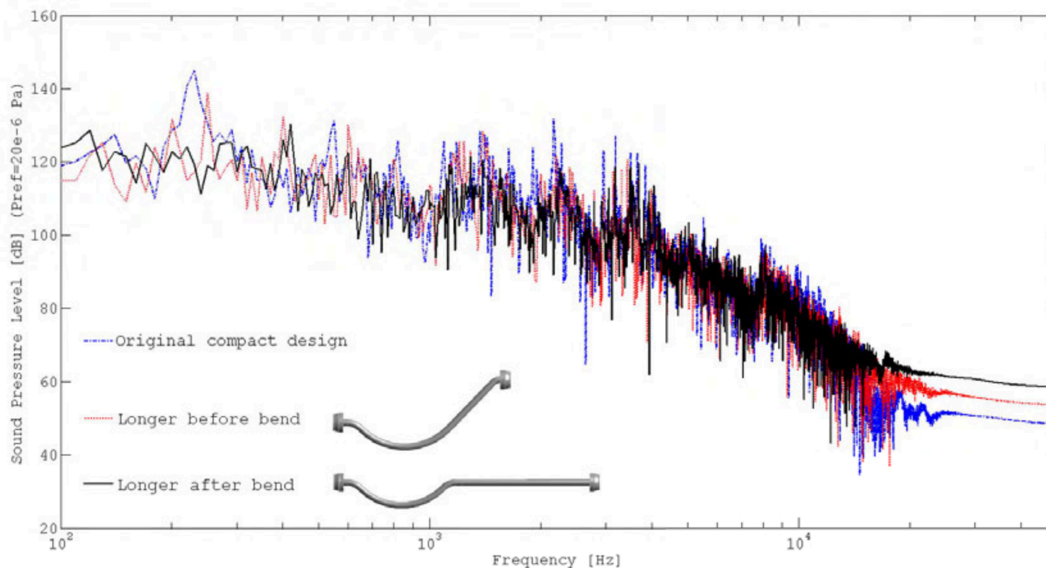


Figure 7.5: Comparison of the sound pressure level at the inlet sensor for the highest Reynolds number for different outlet cases.

After many attempts to decrease the acoustic source with no success, this solution method was disregarded. A certain level of turbulence is always present in such junctions at high flow rates, and although the geometry may be optimized, a complete suppression of the flow-induced sound does not seem to be possible. Thus any further implemented methods must realize that the flow-induced sound cannot be dismissed and take it into account in the solution. Furthermore, different design rules need to be implemented to enable an optimized design.

### 7.1.5 Reducing the effect of the acoustic source on the sensors

The magnitude of the sound source could not be successfully reduced, but the possibility of minimizing the effect of the sound source on the system still remains. Many concepts can be found in literature, which range from the use of various porous materials to reduce the broadband

spectra [49] to the utilization of reflective or dissipative silencers [48]. Reflective silencers function by causing a reflection of waves by an impedance mismatch, for example with a side-branch resonator. The reflective silencer, intended for the plane wave range, is primarily used for damping singular frequencies. The application of other materials in dual channel mass flow meters is tenuous since many of the meters are used at very high pressures, temperatures and even for hygienic applications with very high demands on the fluid contact surface. Also the addition of a side branch proves difficult in such systems due to the increased pressure loss [50]. The pressure loss requirements on dual-channel mass flow meters are relatively strict, and a low pressure drop offers a competitive advantage in industry. Optimally, the pressure drop of the devices should also not be negatively affected.

A further adaption would be the Helmholtz resonator which is largely used to control acoustic instabilities in combustion chambers. The resonator damps oscillations at the design frequency very well, but it unfortunately has a narrow range of actuation close to the design frequency [51] as shown in figure 7.6 for the simple Helmholtz resonator design. The design can also be made more complex, as in the second plot of figure 7.6, where several frequency ranges can be damped simultaneously. Since there is a broad range of the disturbance frequencies present due to the flow induced sound in the mass flow meters, targeting a narrow frequency band, or even several thereof, will not suffice for design improvement. This is especially true when measuring a variety of mediums, for example air or water, where the frequencies shift along the spectrum and outside of the damped regions. Furthermore, the resonator presence can modify the spectrum of frequencies, and even result in the amplification of certain oscillations [51].

Considering industrial pipelines in general, the problem of flow induced sound is largely present mostly due to sharp elbows and control valves. During the design phase of such pipelines, considerations are taken to reduce the noise. For example, the distance between an elbow and valve is required to be ten times the pipe diameter for flow into the valve, and twenty times the diameter for flow into the elbow [54]. Furthermore junctions should not occur at ninety degree angles and the pressure drop

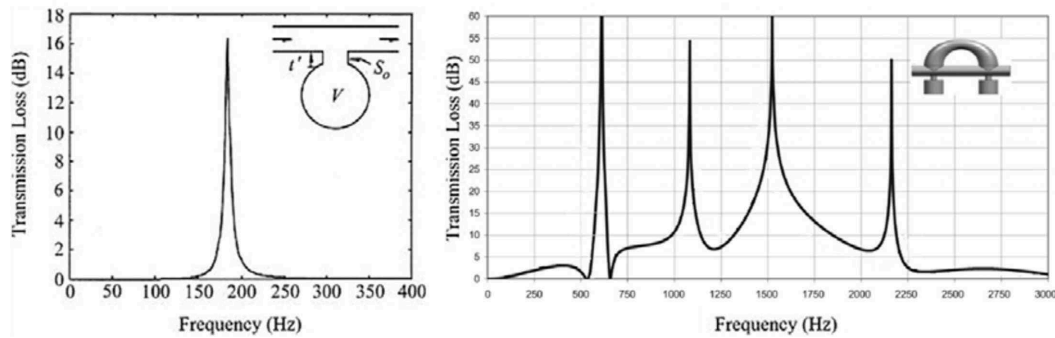


Figure 7.6: Working range of two different Helmholtz resonators [52, 53].

should be split into stages, without any extreme diameter or direction changes [54]. The design of the flow meters cannot be lengthen too much in order to incorporate such specifications. These specifications may be taken in to account in a pipeline, but in the dual-channel mass flow device which are to be compact as possible, these design recommendations cannot be easily implemented.

The general topic of altering the geometry such that no drastic changes occur is however a good one, especially if the system is considered with regard to the acoustics. The fundamental problem in the mass flow device is incidentally not the flow induced sound. The acoustic pressures produced at the outlet flow diverter are, relative to the hydrodynamic pressures, very small and their direct effect on the duct is minuscule. The disturbance arises, in that these acoustic pressures excite the acoustic resonances in the smaller parallel ducts and thus the pressures are amplified to a magnitude where they start to take a larger effect on the duct wall. Thus, the flow induced sound does not necessarily need to be minimized, but rather the magnification through the acoustic resonances. This method is a promising technique to reduce the disturbances on the mass flow devices and is extended upon the the next section.

## 7.2 Acoustic impedance, resonators and horn theory

Resonance occurs when a system is driven to vibrate at one of its natural frequencies, which results in magnified displacement amplitudes. This can be due to an external force, or in this case, an acoustic pressure. Acoustic resonances are able to build when an effective acoustic system is created between two boundaries. The vibration of a mechanical duct at its resonance frequency is easy to picture because the boundaries are clear. In an acoustic system the boundaries are more difficult to distinguish, as they are defined by a change in the acoustic impedance.

Acoustic impedance is the measure of opposition presented to an acoustic flow, the longitudinal propagation of the acoustic pressures. It characterizes the relationship between the acting sound pressure and the resulting particle velocity [28]. There is a close analogy with electrical impedance, which measures the opposition that a system presents to the electrical flow when electrical voltage is applied to the system. Two situations affect the acoustic impedance in a system. The first occurs when there is a change in the medium through which the acoustic waves are propagating, and thus a change in the propagational velocity. In such a case the specific acoustic impedance,  $Z_a$ , is defined as

$$Z_a = \frac{p_a}{v_a} \quad (7.1)$$

where the speed of sound  $v_a$  is medium dependent. Thus, the acoustic impedance that is acting in opposition to the wave propagation increases with an increase in medium density as well as an increase in the speed of sound. This is however not relevant for dual-channel mass flow meters, since only one medium is present in the duct, in this case air at 10 bar. In the flow meters the acoustic impedance depends not only on the type of medium, but also on the dimensions of the enclosed volume. The acoustic impedance is now calculated using the acoustic volume flow  $q_a$  [56]. The definition of the acoustic impedance  $Z_a$  becomes

$$Z_a = \frac{p_a}{q_a} A, \quad (7.2)$$

where the area  $A$  of the wave propagation comes into effect. The larger the surface of a radiating sound source or the cross section of a column of air is, the lower the acoustic impedance that opposes its motion will be. Changes to the acoustic impedance may result from diameter changes, junctions and even bends [55]. Usually this impedance varies strongly with change in frequency. The acoustic impedance at a particular frequency indicates how much sound pressure is generated by a given air vibration at that frequency [? ].

The acoustic source present at the outlet flow diverter, distributes energy in to the smaller sensor ducts. The amount of energy in each duct is the same for both channels since the device is symmetrical, apart from unavoidable production tolerances. The acoustic pressures thus propagate into the two smaller channels, in this case the plane wave. A large impedance discontinuity will result in maximized energy reflection [57]. In the dual-channel mass flow meters the main disturbance takes form as the two flow diverters. The acoustic pressure in the small ducts is thus partially reflected back at the two ends at the flow diverters and back in to the narrow ducts. This enables the building of standing waves and excites the acoustic resonances between the two flow diverters. In this case the acoustic impedance is much higher or lower than the value calculate with equation 7.2, depending on whether the pressure of the returning wave is in phase or out of phase with the driving pressure [? ]. This may be a reason why the main resonance modes seen in the dual channel flow mass meter are the out-of phase modes between the two ducts as seen in figure 6.1. The in-phase modes may also be observed, but their amplitudes are much lower.

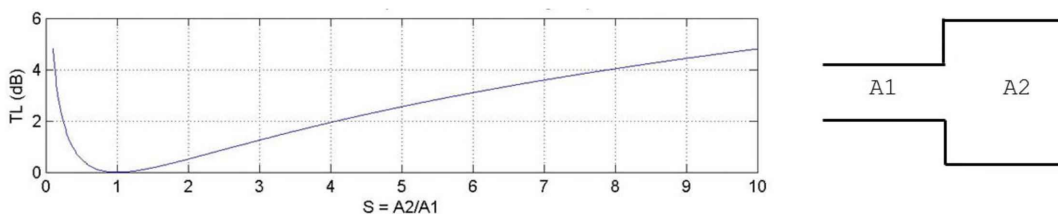


Figure 7.7: Transmission loss in a duct expansion dependent on the ratio of the two areas [58].



When simplifying the system to an expansion from area  $A_1$  to area  $A_2$  as in figure 7.7, the transmission loss  $TL$  is given as

$$TL = 10 \log \frac{(1 + S)^2}{4S} \quad (7.3)$$

with the area ratio given by  $S = A_2/A_1$ . It can be observed that when the areas of the pipes are equal, and the disruption to the impedance is practically zero, the transmission loss is also zero. The larger the fraction  $S$  becomes, the higher the transmission loss or the higher the reflections [58].

The difference between the wave traveling into a narrower or wider duct is outlined by Heller [59]. A wave traveling down an expansion and contraction is pictured in figure 7.8. Assuming  $A_2$  is much bigger than  $A_1$  and the wavelength of the wave is large relative to the duct diameters, the quantity of medium flowing from duct one,  $\rho u_1 \pi a_1^2$ , to duct two must be equal to the quantity of medium in duct two,  $\rho u_2 \pi a_2^2$ . Since the density is constant, the relation

$$u_1 a_1^2 \sim u_2 a_2^2 \quad (7.4)$$

evolves with  $a_1$  as the radius of area  $A_1$  and  $a_2$  as the radius of  $A_2$ . The fluxes of the acoustic flow velocity in the two ducts,  $I_{a,1}$  and  $I_{a,2}$ , can be written as

$$\begin{aligned} I_{a,1} &\sim \rho c u_1^2 a_1^2 \\ I_{a,2} &\sim \rho c u_2^2 a_2^2, \end{aligned} \quad (7.5)$$

and the ratio of the transmitted energy incident from duct one in to duct two results

$$\frac{I_{a,2}}{I_{a,1}} \sim \left(\frac{a_1}{a_2}\right)^2 \ll 1. \quad (7.6)$$

Thus only a small fraction of the acoustic energy is transmitted from a narrow to a wide duct. Furthermore, it has been observed that a short wavelength sound will escape the pipe more readily than a long

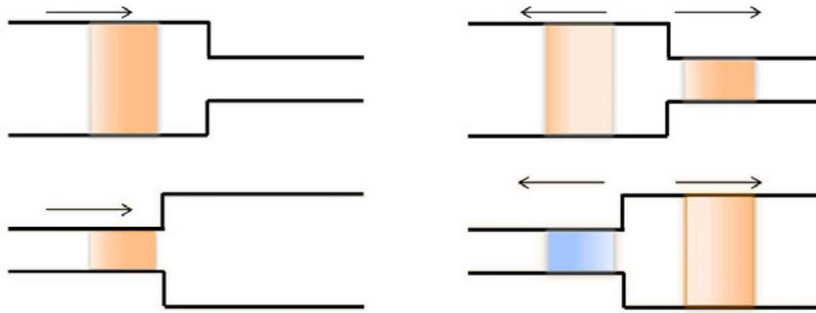


Figure 7.8: Reflection of a propagating wave traveling from a narrow duct in to a wider duct and vice versa [59].

wavelength sound [59]. The frequency is higher for a shorter wavelength, so a cell just inside the tube may not get an in phase, reinforcing reflection from the impedance boundary in time to increase its impedance. Meaning for the lower frequencies in the dual-channel mass flow meter, the reflections will be more trapped.

This behaviour can be influenced by the design of the intersection of the narrow and wider channels, such as in the design of a trumpet. Lower frequencies are reflected at the throat of the trumpet and promotes the building of standing waves at the fundamental frequency. The harmonics, or larger frequencies, are high enough to pass the throat and are radiated outwards. The throat and horn can be designed such that certain frequencies are allowed to pass, see figure 7.9. The flatter and narrow scaled horns transmit relatively small amounts of the sound energy outwards, and rather promote reflection back into the instrument. Steeper and widely scaled horns are louder since they promote the transmission of the sound energy and restrict the reflection back in to the instrument where there is only a weak building of standing waves [60].

Relating this to a dual-channel mass flow meter, the device may become louder itself, but without the excited acoustic resonances the acoustic pressures would probably cause a smaller disturbance in the narrower ducts where the sensors are present. There are diverse algorithms available to calculate the horn shape, which meet the needs of the design. Solving the wave equation (2.16) in three dimensions for a horn is very

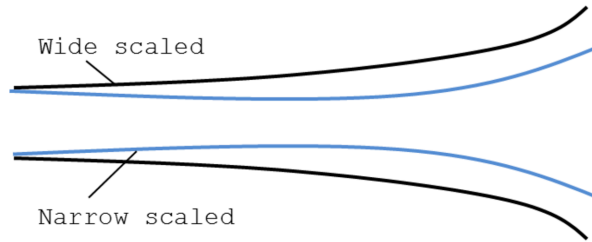


Figure 7.9: Narrow and wide scaled horns show different behaviours regarding the transmission and reflection of sound [60].

complex. A solution has been proposed to simplify the problem to a one dimensional case, by assuming that the sound energy is uniformly distributed over a plane wave front perpendicular to the horn axis. For the case where the area of the duct changes along the direction of propagation, an altered version of the continuity of mass from (2.1) must be formed using the changing area  $A(x)$

$$A \frac{d\rho}{dt} + \rho_0 A \frac{du}{dx} + \rho_0 u \frac{dA}{dx} = 0. \quad (7.7)$$

Substituting the equation of state for the density, the result is the Webster Horn equation [61]

$$\frac{1}{c^2} \frac{\partial^2 p}{\partial t^2} - \frac{\partial^2 p}{\partial x^2} - \frac{\partial(\ln A)}{\partial x} \frac{\partial p}{\partial x} = 0. \quad (7.8)$$

Using this equation in the optimization of the velocity potential along  $x$ , two well known designs result, the exponential horn and later the spherical horn. The initial exponential horn follows the design

$$A(x) = A_0 e^{2\alpha x} \quad (7.9)$$

along the horn middle axis with horn constant  $\alpha$ , and ends with a  $90^\circ$  opening angle. The form was first thought to produce the best transmission since the wave was assumed to propagate in an even form, as used in the Webster equation (7.7). This means that the sound along the middle axis of the horn had a shorter length of travel than the sound at the

boundaries. This is however not true. The wave in fact propagates with a round front meaning the sound at the middle axis of the horn advances further than the sound at the boundaries. If the exponential expansion in equation (7.5) is now applied to this rounded form, a spherical horn results. Improved sound transmission is obtained using a spherical horn, with a  $180^\circ$  opening angle, see figure 7.10 [62].

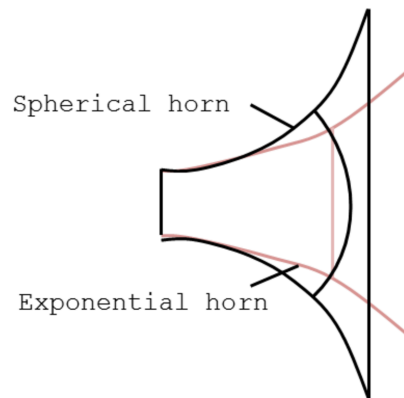


Figure 7.10: The exponential and spherical horn designs with assumed even and rounded front sound propagation forms [62].

Two possibilities have been presented which may improve the dual channel mass flow meter design:

- Impedance matching between the narrower and wider channels.
- A horn design of the wider channel expansion which promotes the transmission of sound.

A combination may be used in a new design of the flow divider. The total area change between the two narrow ducts and wider duct can be minimized, and this area can then be widened using horn design to meet the correct diameter of the outlet duct. This would be an attractive design change for dual-channel mass flow meters as only the flow diverters would need to be changed while the rest of the duct design which produces an optimized measurement performance may remain untouched. This solution is also applicable for the entire frequency range and not just

at certain tonal sounds, which meets the requirements of a dual channel mass flow meter better than for example a Helmholtz resonator. The overall cost of the device, depending on the intricacy of the flow diverter design should also not be drastically affected. Optimizing the impedance change is also beneficial to the transportation of the fluid in the duct with minimized energy loss [57]. It is this method that will thus be attempted in solving the repeatability accuracy issues in the devices. It is however not yet known how much of an improvement these two design considerations mentioned above may bring, and if the repeatability error can be brought within the 0.35% limit as required. There are also other impedance jumps in the system, such as at the bends and in the duct system as a whole, but these seem to have a smaller effect on the disturbances on the device. Thus the flow diverter will first be optimized.

### 7.3 Prototype design and verification

The first design rule to be applied is the impedance matching between the narrow and wider duct sections. To achieve this the sum of the two areas of the narrow ducts,  $A_1$  and  $A_2$ , must be equal to the area of the wider duct  $A_3$  and this area should remain constant through the junction

$$A_1 + A_2 = A_3. \quad (7.10)$$

In this way the total flow area remains the same through the joining of the two flows. However, the result is that the area  $A_3$  is smaller than the required norm outlet duct which attaches to the flange. This means that the area  $A_3$  subsequently needs to be increased to the final standard area depending on the size of the mass flow device. Here the second design rule relating to horn design is applied. The area  $A_3$  is thus subsequently increased using, optimally, an exponential horn function which promotes maximal sound transmission. Through these two design steps of impedance matching and subsequent horn design, the reflection of the sound should be minimized between the two flow diverters, and the acoustic resonances should either be much weaker or not be able to build at all. This means that both flow diverters need to have an optimized

design, at the inlet and outlet.

Practice proves to be more complex than the theory, and an optimal application is difficult to achieve. Due to the limited space and production limitations of the design contours in the flow diverters the geometries cannot be perfectly optimized. Furthermore, the junction is not completely circular since the two narrow ducts together are wider than they are high. A number of different design variations have been perceived in order to meet the requirements as well as possible, with different degrees of complexity. Figure 7.11 shows the designs from a cut side and top view such that the contours may be distinguished. All designs attempt to keep the area change from the two narrow ducts to the one wider duct as small as possible. This is partly achieved through a nose between the two narrow ducts which decreases in size as the areas are slowly joined. Other designs, such as design four in figure 7.11, try to achieve the same affect through the outer curvature of the junction.

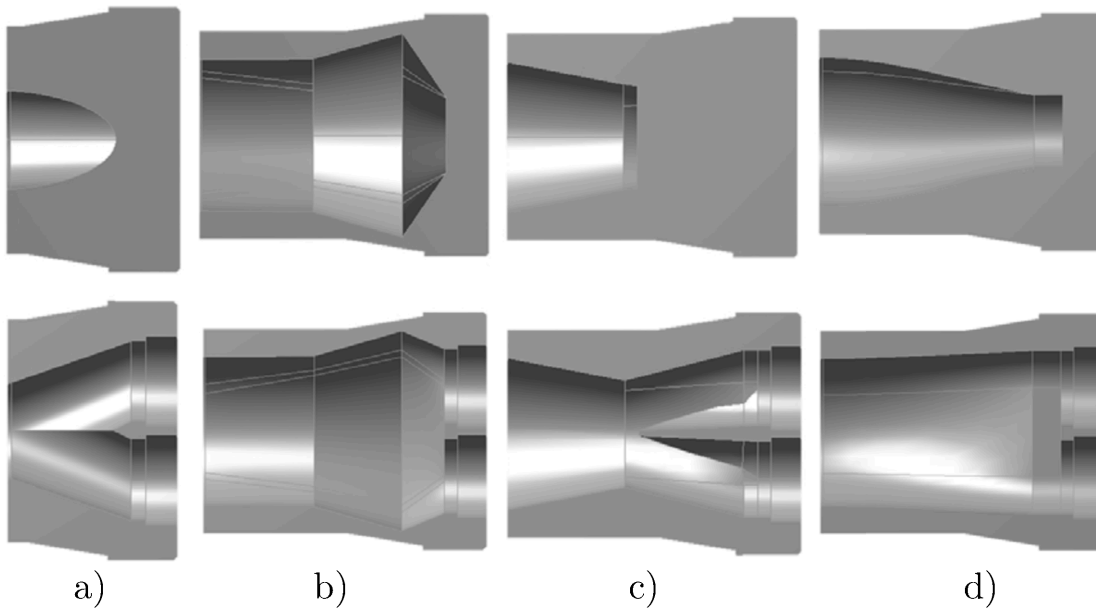


Figure 7.11: A few examples of the new flow diverter designs, a)-d) designs 1 4, based on impedance matching and horn design.

Horn design is applied to the designs as much as possible, but it is dif

difficult to achieve a spherical horn shape, due to the ovality of the junction area and the joining of the two areas into one single area. Exponential curvatures have resulted, which are partially optimized. In compromise, the length of the flow diverter has been increased to assist in finding a greater optimized solution. The total device length is increased by approximately 10 cm. Once the method has been verified a further optimization may be run for a shorter design. Before a prototype is built, the same numerical analysis was conducted on mass flow meter devices of the *compact* design with all four new inlet and outlet flow diverters shown in figure 7.11. As expected the acoustic source at the outlet flow diverter is still present in all cases, at a similar amplitude to the original designs, see figure 7.12. Although the volume of the acoustic source is smaller, the amplitude is similar to the original designs and as such acoustic pressures will still propagate with the plane wave in to the narrower ducts. This confirms again that this acoustic source cannot be eliminated, and future designs must consider the source as a constant.

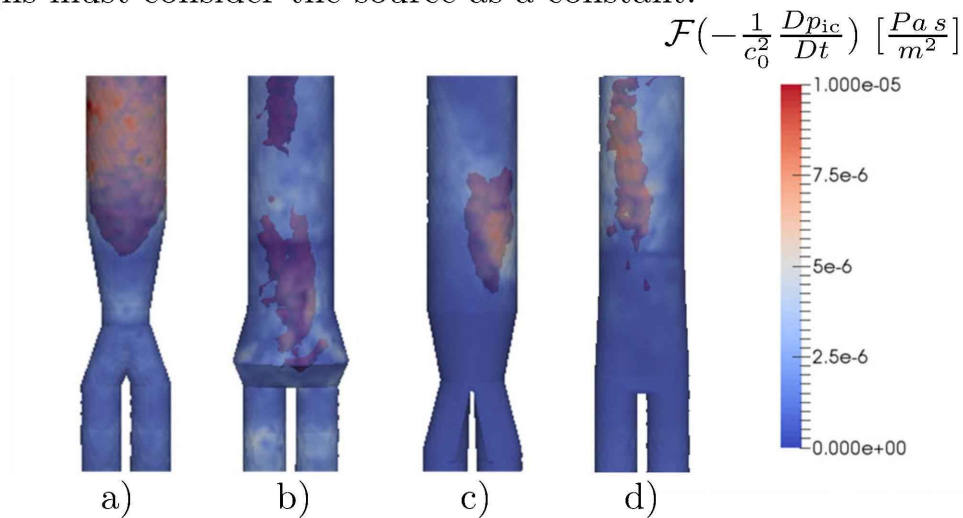


Figure 7.12: Comparison of the acoustic source in the four new flow diverter designs at the outlet side a) d) designs 1 4.

Leaving the acoustic source area and focusing now on the narrow ducts, the effect on the sensor positions seems to be able to be optimized. The plots in figure 7.13 show the sound pressure levels at the sensor position x1 on the simulated devices over frequency at the highest Reynolds num

## 7 Improved design

ber. Designs 1 and 2 still contain large peaks compared to the original compact design, but designs 3 and 4 show much lower peaks in the amplitude at the known acoustic resonances. Overall the sound pressure level in these two designs is between 5–20 dB lower than the sound pressure level in the compact device at this Reynolds number, depending on the frequency. When studying the volume plots of the acoustic pressures the distinctive acoustic resonances between the flow diverters were either not present or only weakly present. The disturbances to the devices caused by the acoustic pressures are now best visualized using the volumetric mechanical displacement as shown in figure 7.14. The compact device, pictured first, is compared to the total magnitude of the displacements in the other four designs using the same scale with a maximum displacement set to 10 nm at the drive frequency, or second acoustic resonance of the original compact device.

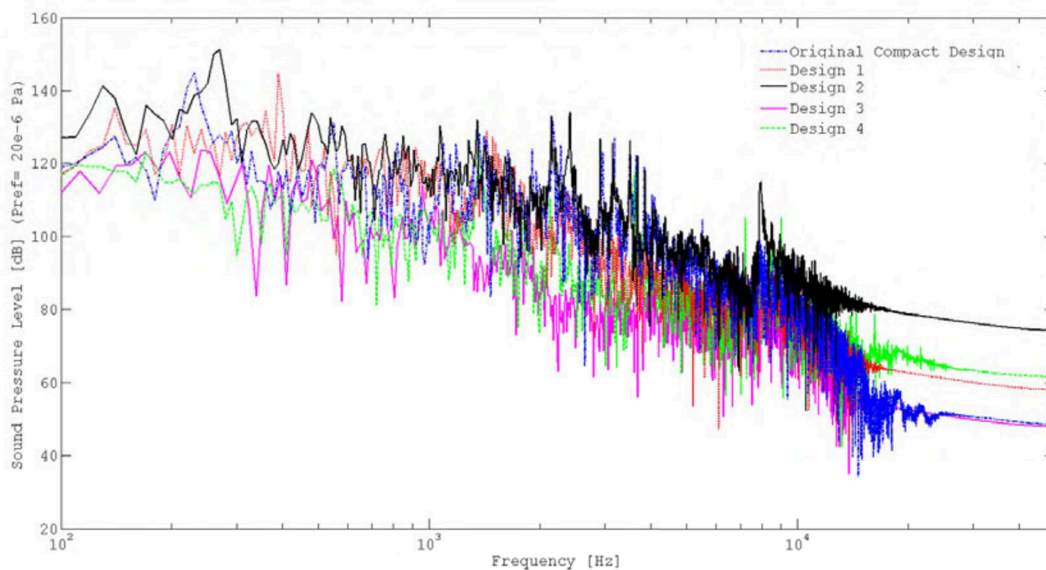


Figure 7.13: Sound pressure level plots of the new flow diverter designs compared to the original compact design at the highest Reynolds number at the inlet sensor monitoring point x1.

Designs 1 and 2 show little improvement with similar or worse magnitudes than the original device, but designs 3 and 4 show almost ten



times less disturbance displacement than the original design. With these promising results the two designs 3 and 4 are built as prototypes for further verification of the improvement on the gas calibration rig.

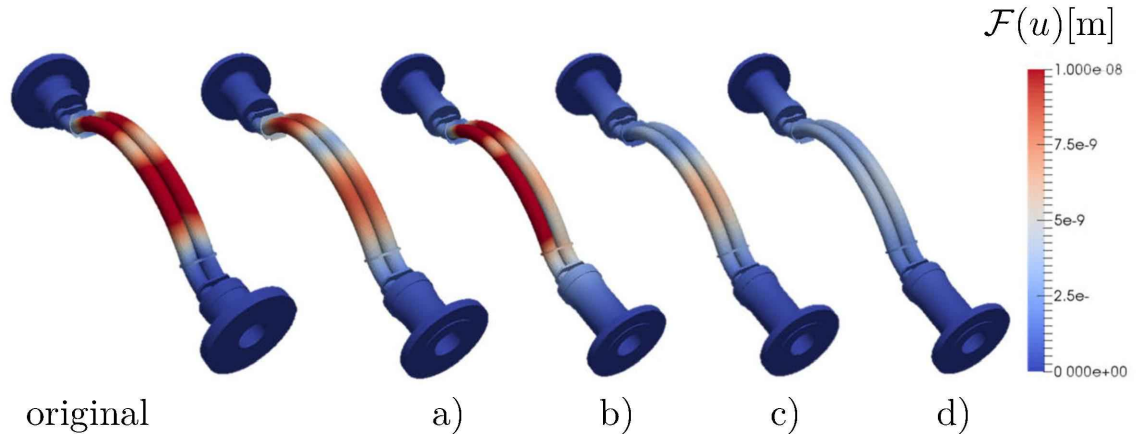


Figure 7.14: Volumetric plots of the displacement magnitude in the original and new *compact* geometries, a) d) designs 1 4, at the highest Reynolds number and the drive frequency of the compact device, also the second acoustic resonance.

The two designs were, as the original designs, verified on a gas calibration rig with air at 10 bar. Again the same mass flow rates were measured as calculated in the numerical simulations with ten measurement points at each flow rate. Subsequently the scattering of the measurement values could be observed over mass flow rate.

The initial results for the two designs are shown in the plot in figure 7.15 compared to the original *compact* device measurement results. Two improvements can be observed. Firstly, the deflection from the zero axis at the lower flow rates is decreased and secondly the scattering of the flow measurement values at the higher flow rates is greatly reduced.

A notable observation could be made with design 3, in that as the flow rate in the calibration rig was increased, an increasing tonal frequency could be clearly heard outside of the device. This confirms that although the device has now become louder, like a trumpet, the performance is nevertheless still improved because the acoustic resonances are not able to build as strongly. When the scattering magnitudes of the measure

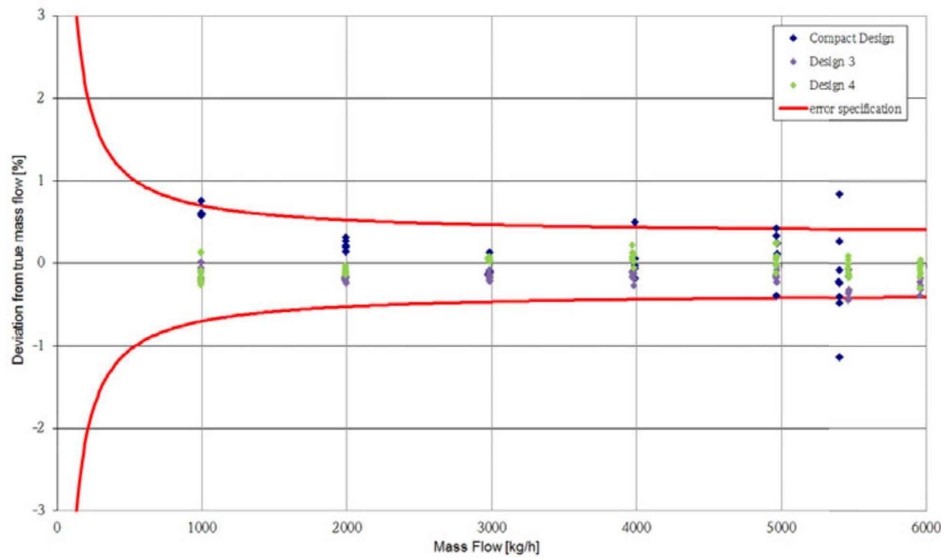


Figure 7.15: The deviation from the true mass flow for the compact device and the two new prototypes with ten measurements taken at each mass flow on the gas calibration rig.

ments are directly compared in figure 7.16, an improvement from 0.33% maximum scattering in the original compact design to 0.14% maximum scattering in design 3 and 0.07% in design 4 has been achieved.

Design 4 is the best geometry, but also more complex to produce than design 3. Depending on the requirements in industry, both design 3 and design 4 offer good solutions to high speed measurements with fluids. Overall, this design method has resulted in an improvement in the repeatability accuracy of the device and brought the total error to well within 0.35%. With these design alterations, the dual-channel mass flow meter can be successfully used to measure high speed mass flows, especially high speed gas flow with good repeatability of the measurement values. This is the first design of a dual-channel mass flow meter based on acoustic design rules, which shows the best repeatability accuracy for a 50 mm diameter device on the market and a patent application has been filed. The new flow diverter designs may be easily integrated in to current flow meter devices since only the flow diverter components need to be changed. The designs do not have greatly increased costs, and the

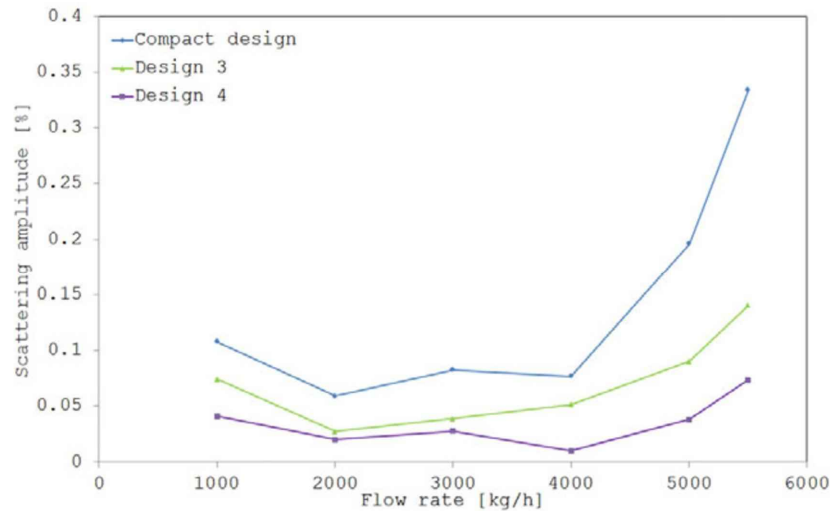


Figure 7.16: Scattering amplitude of the measurements at each flow rate for the compact and new designs.

material does not need to be altered. The length of the dual channel mass flow meter is still longer than the standards allow. In order to optimize the designs much more effectively and efficiently, and optimization tool needs to be developed. Such a tool may be integrated in to the general dual-channel mass flow meter optimization algorithm.

### 7.4 1D Acoustics and a design tool for dual-channel meters

The numerical method described in chapter 3 is the best approach for a detailed analysis of the flow-induced sound in dual-channel meters, where the detailed influence of the acoustic fluctuations on the duct walls may be investigated. For the interpretation of the flow induced sound phenomena occurring within the system, this method is undeniably necessary and important, particularly when studying different flow rates.

Now that the underlying mechanism has been understood, a simplified and accelerated calculation method for dual-channel mass flow meter designs may be adopted. This method does not need to quantify the detailed influences of the disturbance frequencies but should optimize the effect relative to the original design. Before this tool is developed, a closer look

at a simplification of the acoustic system into a one dimensional case is taken.

A one dimensional acoustic analysis may be implemented since the main excitation of the system is initiated by the plane wave. The sound pressure of a traveling plane wave in terms of space and time may be described as

$$p_a(x, t) = (p_+ e^{-jkx} + p_- e^{jkx}) e^{j\omega t}, \quad (7.11)$$

where the direction of the propagation in the pipe is indicated by + and -. Similarly the acoustic particle velocity is given by

$$u_a(x, t) = \frac{1}{\rho c} (p_+ e^{-jkx} - p_- e^{jkx}) e^{j\omega t}. \quad (7.12)$$

Substituting the definition of the acoustic impedance (7.1) and the initial value relations

$$p_0 = p_+ + p_- \quad (7.13)$$

$$u_0 = \frac{1}{Z_a} (p_+ - p_-), \quad (7.14)$$

into the equations for the acoustic pressure and particle velocity, the transfer equations for an acoustic homogeneous pipe from inlet to outlet are achieved, a full derivation may be found in [63]

$$\begin{pmatrix} p_o(x, t) \\ u_o(x, t) \end{pmatrix} = \begin{pmatrix} \cos(kx) & -jZ_a \sin(kx) \\ -j\frac{1}{Z_a} \sin(kx) & \cos(kx) \end{pmatrix} \begin{pmatrix} p_i(x, t) \\ u_i(x, t) \end{pmatrix}. \quad (7.15)$$

Here the inlet and outlet values are related by a transfer matrix  $K$ . By inverting the transfer matrix, a description in terms of the sound volume flux  $q_a$  is obtained

$$\begin{pmatrix} p_i(x, t) \\ q_i(x, t) \end{pmatrix} = \begin{pmatrix} \cos(kx) & jZ_a \sin(kx) \\ j\frac{1}{Z_a} \sin(kx) & \cos(kx) \end{pmatrix} \begin{pmatrix} p_o(x, t) \\ q_o(x, t) \end{pmatrix}. \quad (7.16)$$

Description (7.16) may be extended to more complex systems, for example where reflections occur. Such situations evolve when there are diameter changes along the pipe length. In this case a total transfer matrix  $K_{\text{total}}$  is used to connect the inlet and outlet values using the product of the partial matrices  $K_t$

$$\begin{pmatrix} p_i(x, t) \\ q_i(x, t) \end{pmatrix} = \prod_{t=1}^n K_t \begin{pmatrix} p_o(x, t) \\ q_o(x, t) \end{pmatrix}. \quad (7.17)$$

Also a common feature in duct systems, junctions between two or more pipes may be represented. Junctions may be classified as serial or parallel, depending on the relation to the acoustic impedance to the main duct. In general, serial junctions are described using a transfer matrix of the form

$$K_s = \begin{pmatrix} 1 & Z_j \\ 0 & 1 \end{pmatrix}, \quad (7.18)$$

including the acoustic impedance of the junction  $Z_j$ . Similarly, parallel junctions are described using the transfer matrix

$$K_p = \begin{pmatrix} 1 & 0 \\ 1/Z_j & 1 \end{pmatrix}. \quad (7.19)$$

When simplifying a dual-channel mass flow meter into a one dimensional case, a system containing three partial transfer matrices may be established, as depicted in figure 7.17. Additionally, an impedance of the junction  $Z_j$  is present for the separation of the flow into the two smaller ducts, which are parallel to the main duct.

The total transfer matrix needs to consider the diameter change from partial system 1 to partial systems 2 and 3, as well as the impedance experienced at the junction. In such a case, the input impedance of

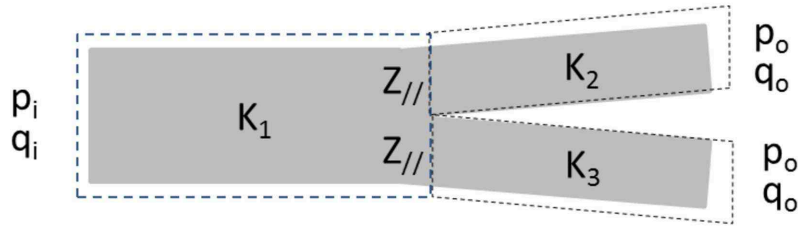


Figure 7.17: Simplification of dual-channel mass flow meter into a one dimensional system.

partial system 2 would be inserted into the transfer matrix of partial system 3 and vice versa. However, since both partial systems are equal in diameter and impedance change, the system is considered as transfer and impedance symmetric, with  $K_j = K_{23} = K_{32}$ . The description of the system is thus represented by

$$\begin{pmatrix} p_i(x, t) \\ q_i(x, t) \end{pmatrix} = K_1 \cdot K_2 \cdot K(Z_j) \begin{pmatrix} p_o(x, t) \\ q_o(x, t) \end{pmatrix} \quad (7.20)$$

$$\begin{pmatrix} p_i(x, t) \\ q_i(x, t) \end{pmatrix} = K_1 \cdot K_3 \cdot K(Z_j) \begin{pmatrix} p_o(x, t) \\ q_o(x, t) \end{pmatrix}. \quad (7.21)$$

Of course if the diameter changes are not simple cross sectional jumps but continual changes over the length, such as an exponential horn, then the transfer matrices need to be adjusted accordingly. For example if the partial system 1 has an exponential change in diameter, then the transfer matrix  $K_1$  would be altered to

$$\begin{pmatrix} p_i(x, t) \\ q_i(x, t) \end{pmatrix} = \begin{pmatrix} e^{\alpha x} (\cos(\beta x) - \frac{\alpha}{\beta} \sin(\beta x)) & j Z_a(x) \frac{k}{\beta} \sin(\beta x) \\ j \frac{1}{Z_a(x)} \frac{k}{\beta} e^{\alpha x} \sin(kx) & e^{-\alpha x} (\cos(kx) - \frac{\alpha}{\beta} \sin(\beta x)) \end{pmatrix} \begin{pmatrix} p_o(x, t) \\ q_o(x, t) \end{pmatrix}, \quad (7.22)$$

with horn constant  $\alpha$ , propagation constant  $\beta$  and the acoustic impedance  $Z_a$ , which is a function of the position  $x$ . Considering the description of the one dimensional dual-channel flow meter system, the same conclusion may be reached as in the previous section. In order to optimize the

design such that no acoustic resonances are to be excited, the change in the diameters and in the acoustic impedance at the junction needs to be minimized. A simplified tool may be used for this purpose, which only considers the plane wave propagation in the system design. The acoustic geometry from the previous investigations is read into the simulation software Comsol, where a pressure acoustics study is set up in the frequency domain.

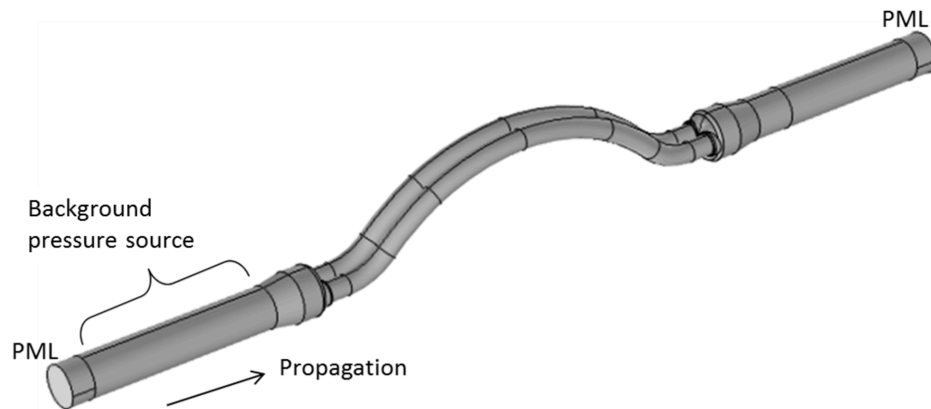


Figure 7.18: Simplified acoustic model of a dual-channel mass flow meter in Comsol.

For this purpose, a background acoustic source is applied to the outlet side of the duct, as a broadband sound source between the frequencies 0 Hz and 1000 Hz, as shown in figure 7.18. Two PML regions at the inlet and outlet of the duct are defined and the reaction of the system to the source is studied. This analysis is carried out for the original geometry, as well as for the two improved prototypes from section 7.3. As expected, the acoustic resonances identified in the previous investigation are once again excited. For example, figure 7.19 shows the excitation of the known second acoustic resonance in the original geometry at 550 Hz. When comparing the original geometry to the two improved prototypes from section 7.3, the excited acoustic resonances in the newer geometries are seen to be smaller in amplitude. This confirms that the two new designs show an improvement in the acoustic behaviour of the narrow tubes, with smaller disturbance amplitudes due to the induced acoustic

resonances between the flow splitters. A direct comparison is made using a monitoring point at the sensor position in figure 7.20.

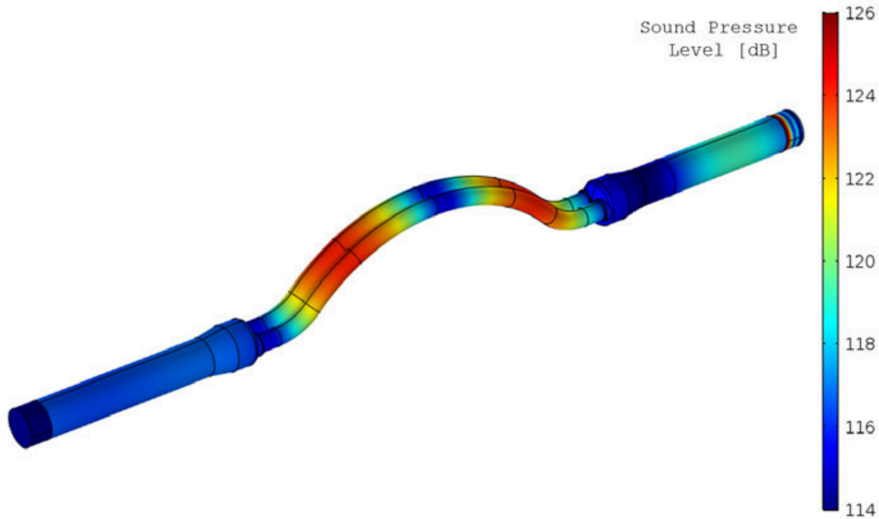


Figure 7.19: The excitation of the second acoustic resonance of the original geometry in Comsol.

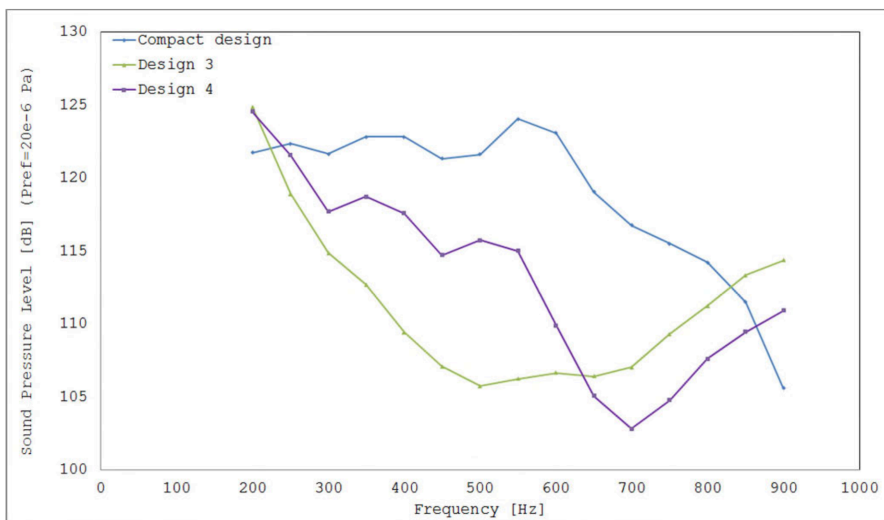


Figure 7.20: A comparison of the sound pressure level at the sensor in the original, and two new prototypes from section 7.3.



## 7.4 1D Acoustics and a design tool for dual channel meters

---

This simple simulation requires less than thirty minutes run time, and is satisfactory for the optimization of an adapted geometry relative to an original design. It allows the quick optimization of the dual channel mass flow meters regarding the acoustic behaviour, and will be used in further investigations related to this work.

# CHAPTER 8

---

## Conclusion

---

### 8.1 Summary

This dissertation set out to resolve the issue of the large scattering in the measurement values consequent of measuring high speed flows with dual-channel mass flow devices. The phenomenon was successfully linked to flow-induced sound when the turbulences in the ducts are large. Due to the complexity of the system, with the sound source occurring directly in the device, the acoustic quantities could not be directly quantified. Three different mass flow devices were thus analyzed using a hybrid computational aeroacoustic method using Lighthills analogy and the separation of the pressure into its incompressible and acoustic components. Through subsequent direct coupling of the mechanical and acoustic values, a vibroacoustic analysis was conducted. The fluid dynamic results showed large turbulence areas at the inlet and outlet flow diverters and at the bends in the ducts. The acoustic analysis confirmed that the main acous-

tic source was in fact at the outlet flow diverter, with the sources at the inlet and bends almost ten times smaller across the frequency spectrum. Observation of the volumetric acoustic pressures in the frequency domain revealed the building of strong acoustic resonances. The strongest of these resonances occur between the two flow diverters within the narrow ducts. At these acoustic resonances, the mechanical displacements of the narrow pipes increases drastically and these disturbances are partially able to enter the signal processing of the measurement signal causing scattering of the values. This behaviour has been confirmed through measurements of the three devices on a gas calibration rig with air at 10 bar. When the disturbances were close to the drive frequency of the meters, or to multiples thereof, a large scattering of the measurement values resulted. Furthermore, the disturbances could be measured on the narrow ducts at the inlet sensor using two Doppler laser vibrometers. The position and amplitude of these disturbances correlated well to those observed in the numerical investigations. The non linear behaviour of the degree of scattering, which increased at certain Reynolds numbers, could be linked to the energy spectrum of the turbulence at the main acoustic source location. The energy content of the turbulence over frequency is Reynolds number dependent and reproducible. At certain Reynolds numbers, different frequencies contain more energy, and correspondingly the acoustic resonances are more or less excited according to the energy supplied to the narrow ducts. Multiple improvement possibilities to the dual channel mass flow devices could be identified, but only reducing the effect of the incessant acoustic source on the sensors was successful in subduing the disturbances on the ducts over the whole frequency range such that the current error specification of 0.35% was achieved. For this purpose, novel flow diverter designs using impedance matching and horn theory were implemented. It is not the acoustic pressures directly which cause the disturbances to the sensors, but their amplification through the acoustic resonances. If the resonances are not able to build, then the disturbances are not as strong. The scattering amplitude was successfully decreased by a factor a five in the *compact* design, with increased stabilities at lower flow rates. The total error specification of the device is within 0.25% of the mass flow reading which is the best performance available in industry.

A patent application on the flow diverter designs has been filed.

### 8.2 Outlook

Acoustic considerations of the devices will be included in the overall optimization algorithm of dual-channel mass flow meter design in future, to ensure highly accurate measurements of rapid flows in all dual-channel mass flow devices. The new flow diverter designs do not increase the cost of the devices, do not require new materials and may be easily substituted in to existing dual-channel mass flow devices. However, there is future work to be completed:

- The total length of the flow diverters could be shortened, if no acoustic benefits are lost, such that the devices comply with the standard device length for their diameter class.
- The effect of the geometry changes on the pressure loss in the system needs to be properly quantified, since this is a critical sales factor.
- Supplementary qualification measurements on the turbulence energy spectrum should be conducted to verify the preliminary results presented here. For this purpose measurements with a pressure sensor at the outlet flow diverter could be made on the calibration rig.
- Although not a focus for this thesis, the overall sound volume of a dual-channel mass flow meter is being investigated. Since the meters may be installed close to residential areas or workplaces the sound volume has to apply to certain specifications which were not regarded in this thesis.
- An additional improvement brought by the new flow diverter designs apart from improving the scattering of the measurement points, was an improved the stability of the device at the lower fluid flows. This may be investigated further for low speed flows with denser fluids to increase the overall performance of the devices.

---

## Bibliography

---

- [1] F. Durst *Fluid Mechanics. An Introduction to the Theory of Fluid Flows* . Springer, 2008.
- [2] N. Witkowski, M. Kaltenbacher *Comparison of Compressible and Incompressible CFD Methods for the Acoustic Analysis of Flow Induced Noise in Confined Flow*. DAGA 41. Jahrestagung für Akustik 2015.
- [3] M. Kaltenbacher, A. Hüppe, A. Reppenhagen, M. Tautz, S. Becker, W. Kühnel, *Computational Aeroacoustics for HVAC Systems Utilizing a Hybrid Approach*. SAE International Journal of Passenger Cars Mechanical Systems V125 6EJ, 2016.
- [4] J. Zhu, X.Q. Wang, W.C. Xie, R.M.C. So, *Flow induced instability under bounded noise excitation in cross-flow*. Journal of sound and Vibration 312 (2008), 476495.
- [5] S.S. Chen, *Flow Induced Vibrations of circular Cylindrical Structures*. Argonne National Laboratory, Base Technology 1977.

- [6] S. Ziada, *Flow excited acoustic resonance in industry*. Journal of Pressure Vessel Technology 132 (2010), 19.
- [7] D. Firth, F.J. Fahy, *Acoustic Characteristics of Circular Bends in Pipes*. Journal of Sound and Vibration 97 (1984), 287303.
- [8] J. Lirvat, F. Mendonca, *Flow and Acoustic Excitation mechanisms in a Nuclear Reactor Steam line and Branch Network*. 18th AIAA/CEAS Aeroacoustics Conference, 2012.
- [9] R.G. Huff, *Noise Generated by Flow Through Large Butterfly Valves*. NASA Technical Memorandum 88911, 1987.
- [10] N.K.Singh, P.A. Rubini *Large Eddy Simulation of acoustic pulse propagation and turbulent flow interaction in expansion mufflers*. Applied Acoustics 98 (2015), 619.
- [11] G.J. Bennett, J. Kennedy, C. Meskell, M. Carley, P. Jordan, H. Rice, *Aeroacoustics research in Europe: The CEAS ASC report on 2013 highlights*. Journal of Sound and Vibration 340 (2015), 3960.
- [12] A. Holmberg, M. Karlsson, M. Abom, *Aeroacoustics of rectangular T-Junctions subject to combined grazing and bias flows - An experimental investigation*. Journal of Sound and Vibration 340 (2015), 152166.
- [13] S.A. Hambric, D.A. Boger, J.B. Fahnline, R.L. Campbell, *Structure and fluid-borne acoustic power sources induced by turbulent flow in 90<sup>circ</sup> piping elbows*. Journal of Fluid and Structures 26 (2010), 121 147.
- [14] L.Xin, W. Shaoping, *Flow field and pressure loss analysis of junction and its structure optimization of aircraft hydraulic pipe system*. Chinese Journal of Aeronautics 26(4) (2013), 10801092.
- [15] E. Alenius, M. Abom, L. Fuchs, *Large eddy simulations of acoustic flow interaction at an orifice plate*. Journal of Sound and Vibration 345 (2015), 162177.

- 
- [16] X. Gloerfelt, P. Lafon, *Direct computation of the noise induced by a turbulent flow through a diaphragm in a duct at low Mach number*. Computers & Fluids 37 (2008), 388401.
- [17] G.G. Coriolis, *Memoire sur le principe des forces vives dans les mouvements relatifs des machines (On the principle of kinetic energy in the relative movement of machines)*. J. de Z'Ecole Polytechnique, 13, Cahier 21, pp. 268 302, 1832.
- [18] H.R. Tränkler, L.M. Reindl, *Sensortechnik: Handbuch für Praxis und Wissenschaft*. Springer, 2014.
- [19] c. Sujatha, *Vibration and Acoustics: Measurement and Signal Analysis*. Tata MyGraw Hill Education, pp.428 431, 2010.
- [20] Y. Hussein, W. Favell, C.N. Rolph, V. Cook, *Mass Flow Meter composed of two measuring Tubes with a connecting Device between them*. U.S. Patent 7,275,449, October 2007.
- [21] T. Wang, C. Rolph, G. Jones, *Coriolis Mass Flow Meter*. U.S. Patent 20,150,377,671, June 2015.
- [22] G. Li, *Coriolis mass flow meter with micro-bend tubes*. U.S. Patent 8813576, August 2014.
- [23] Y. Hussein, W. Favell, C.N. Rolph, V. Cook, *Method and apparatus for non invasively measuring physical properties of materials in a conduit*. U.S. Patent 20150212045, July 2015.
- [24] L. Gouy, F. Allouche, *Apparatus and method for calibration of coriolis meter for dry gas density measurement*. European Patent 2749854, July 2014.
- [25] N. Sukemura, T. Motomiya, *Coriolis flowmeter*. European Patent 2843375, March 2015.
- [26] P.M. Morse, K.U. Ingard, *Theoretical Acoustics*. McGraw Hill, New York, 1968.

- [27] M.P. Norton, M.K. Bull, *Mechanisms of the Generation of external Acoustic Radiation from Pipes due to Internal Flow Disturbances*. Journal of Sound and Vibration 94 (1984), 105146.
- [28] S.W. Rienstra, A. Hirschberg, *An Introduction to Acoustics*. Eindhoven University of Technology, 2015.
- [29] A.S. Sarigül, *Sound Attenuation Characteristics of Right Angle Pipe Bends*. Journal of sound and Vibration 228 (1999), 837844.
- [30] R.M.A. Marretta, G. Tassone, *A vorticity based aeroacoustic prediction for the noise emission of a low-speed turbulent internal flow*. Computers and Fluids 32 (2003), 457478.
- [31] M. Kaltenbacher, M. Escobar, S. Becker, I. Ali, *Numerical simulation of flow-induced noise using LES/SAS and Lighthill's acoustic analogy*. International Journal for Numerical Methods in Fluids 63 (2009), 11031122.
- [32] M. Kaltenbacher, *Numerical Simulation of Mechatronic Sensors and Actuators Finite Elements for Computational Multiphysics*. Springer, 3rd ed., 2015.
- [33] Y.H. Heo, J.G. Ih, H. Bodén, *In-duct identification of fluid-borne source with high spatial resolution*. Journal of Sound and Vibration 333 (2014), 60746089.
- [34] M.J. Lighthill, *On Sound Generated Aerodynamically. I. General Theory*. Proceedings of the Royal Society of London, 1952.
- [35] M.J. Lighthill, *On sound generated aerodynamically. II. Turbulence as a source of sound*. Proceedings of the Royal Society of London (Vol.222), 1954.
- [36] J.E. Ffowcs Williams, *The Acoustic Analogy thirty years on*. IMA Journal of applied Mathematics (1984) 32, 113124.



- 
- [37] M. Kaltenbacher, M. Escobar, I. Ali, S. Becker, *Finite Element Formulation of Lighthills Analogy*. University of Erlangen Nuremberg, 2005.
- [38] X. Gloerfelt, F. Perot, C. Bailly, D. Juvé, *Flow induced cylinder noise formulated as a diffraction problem for low Mach numbers*. Journal of Sound and Vibration 287 (2005), 129151.
- [39] B. Kaltenbacher, M. Kaltenbacher, *A modified and stable version of a perfectly matched layer technique for the 3 d second order wave equation in time domain with an application to aeroacoustics*. Journal of Computational Physics, 2013.
- [40] N.A. Pierce, J.J. Alonso, *Efficient Computation of Unsteady Viscous Flows by an Implicit Preconditioned Multigrid Method*. AIAA Journal Vol.36, March 1998.
- [41] F.J. Kelecy, *Efficient Computation of Unsteady Viscous Flows by an Implicit Preconditioned Multigrid Method*. ANSYS Advantage Vol. 2, Issue 2, 2008.
- [42] M. Escobar, S. Triebenbacher, M. Kaltenbacher, I. Ali, S. Becker, R. Lerch, *Hybrid Computation of Flow Induced Noise using the FE Method*. DAGA Conference, 2007.
- [43] A. Hüppe, A. Reppenhagen, M. Kaltenbacher, G. Dutzler, M. Hartmann, N. Peller, *Aeroacoustic investigation of HVAC systems using perturbation equations*. Internoise Conference, 2013.
- [44] N.E.L. Haugen, *Energy Spectra and scaling relations in numerical turbulence with laboratory and astrophysical applications*. Ph.D. Thesis, Norwegian University of Science and Technology, 2004.
- [45] M. Wilczek, Y. Narita, *Wave number frequency spectrum for turbulence from a random sweeping hypothesis with mean flow*. American Physical Society, Physical Review E86, 066308, 2012.

- [46] B. Rydeni, *Basic Turbulence*. Lecture Notes 825, Ohio State University, 2011.
- [47] G. Ahmadi, *Turbulence*. Lecture Notes ME637, Clarkson University, 2015.
- [48] S.P. Harsha, *Noise and vibration of flow in pipes*. Lecture Notes Noise and Vibration control, Indian Institute of Technology Roorkee, 2013.
- [49] N. Sellen, M. Cuesta, M. A. Galland, *Noise reduction in a flow duct: implementation of a hybrid passive/active solution*. Journal of Sound and Vibration 297 (2006), 492 511.
- [50] X. Yu, L. Cheng, *Duct noise attenuation using reactive silencer with various internal configurations*. Journal of Sound and Vibration 335 (2015), 229 244.
- [51] R. Corà, C.A. Martins, P.T. Lacava, *Acoustic instabilities control using Helmholtz resonators*. Applied Acoustics 77 (2014), 1 10.
- [52] S. Griffin, S.A. Lane, S. Huybrechts, *Coupled Helmholtz Resonators for Acoustic Attenuation*. Journal of Vibrational Acoustics 123 (2000), 11 17.
- [53] H. Erol, C. Meric, *Application of resonators and a side branch duct with an expansion chamber for broadband noise control*. Noise Control Engineering 57, 2009.
- [54] J.H. Granneman, R.P.M Jansen, *Sound power determination of large open plants; comparison of alternative methods*. Internoise 93, 1993.
- [55] W. Rostafinski, *Monograph on propagation of sound waves in curved ducts*. NASA Reference Publication 1248, 1991.
- [56] M. Möser, *Technische Akustik*. Springer, 2007.
- [57] F.J. Fahy, *Foundations of Engineering Acoustics*. Elsevier Academic Press, San Diego, 2005.

- [58] *Engineering Acoustics, Filter Design and Implementation*. <https://en.wikibooks.org/wiki/EngineeringAcoustics>, hof Wiki books, 2015, Web. September 2016.
- [59] E.J. Heller, *Why you hear what you hear: An experiential approach to sound, music and psychoacoustics*. Princeton University Press, Princeton, 2013.
- [60] C.Sachs, *Handbuch der Musikinstrumente*. Breitkopf und Härtel, Leipzig, 1930.
- [61] B. Kolbrek, *Horn Theory: An Introduction, part 1*. [www.audioXpress.com](http://www.audioXpress.com), Web. September 2016.
- [62] Avantgarde Acoustic, *Book of Horns*. Avantgarde Acoustic, Lautertal, 2010.
- [63] R. Lerch, G. Sessler, D. Wolf, *Technische Akustik: Grundlagen und Anwendungen*. Springer, Berlin and Heidelberg, 2009.

# Curriculum Vitae

## Personal Data

Name: Natalie Helena Schlachter

Date of Birth: [REDACTED]

Place of Birth: [REDACTED]

## Education

- 01/2006 08/2007 Mechanical Engineering  
University of the Witwatersrand  
Johannesburg, South Africa
- 10/2007 03/2011 BSc. Mechanical Engineering  
Karlsruhe Institute for Technology  
Karlsruhe, Germany
- 04/2011 09/2011 Dipl. General Mechanical Engineering  
Karlsruhe Institute for Technology  
Karlsruhe, Germany
- 03/2014 03/2017 Doctor of Technical Science  
Vienna University of Technology  
Vienna, Austria

## Professional Experience

- 11/2010 03/2011 Bachelor thesis: Optimization of the temperature sensitivity of a ceramic pressure sensor  
Endress+Hauser GmbH+Co.KG, Maulburg Germany
- 04/2011 09/2011 Diplom thesis: Optimization and design of a Coriolis mass flow meter for small pipe diameters  
Endress+Hauser Flowtec AG, Reinach Switzerland
- 10/2011 07/2013 Development Engineer Vortex flow meters  
Endress+Hauser Flowtec AG, Reinach Switzerland
- 09/2013 present Development Engineer Coriolis flow meters  
Endress+Hauser Flowtec AG, Reinach Switzerland